

# Quantum Mechanical Approach for Understanding Reaction Mechanisms of Complicated Systems

Takehiro Yoshikawa

Graduated School of Science and Engineering, University of Saitama



This dissertation is submitted for the degree of Doctor of Philosophy

## Abstract

Although it has been generally accepted that nuclear quantum effects, including tunneling and vibrational quantization, are playing very important roles in light particle transfer reactions, their role has not yet been fully understood in complicated chemical systems. This is simply because it is very difficult to solve quantum mechanical equations of motions except for simple chemical systems. In this work, in order to understand nuclear quantum effects from the theoretical side, we apply path-integral based computational methods, which can be applied to complicated systems. In particular, we would like to demonstrate that various isotope effects seen in many chemical dynamical systems cannot be understood without consideration of nuclear quantum effects.

### **Double proton transfer for porphycene and isotopic variants**

Full-dimensional Path-integral molecular dynamics (PIMD) simulations have been performed for understanding the double proton transfer tautomerization mechanism of the inner two protons in porphycene and its isotopic-substituted molecules. In order to reduce computational costs, the semi-empirical PM6 level combined with specific reaction parameterization have been employed. The obtained results show that double proton transfer of the unsubstituted porphycene at  $T = 300$  K mainly occurs via a so-called concerted mechanism through the  $D_{2h}$  second-order saddle point. In addition, we found that both isotopic substitution and temperature significantly affect the double proton transfer mechanism. For example, the contribution of the stepwise mechanism increases with a temperature increase. We have also carried out hypothetical simulations with the porphycene configurations being completely planar. It has been found that out-of-plane vibrational motions significantly decrease the contribution of the stepwise proton transfer mechanism.

### **Diffusion of hydrogen/tritium in Fe (bcc) lattice**

The diffusion coefficients of hydrogen (H) and tritium (T) in  $\alpha$ -Fe have been computed using two approximate quantum dynamical techniques, *i.e.* centroid molecular dynamics (CMD) and ring polymer molecular dynamics (RPMD), in the temperature range of  $T = 100$ – $1000$  K using the embedded-atom-method (EAM) potential. It has been found that the RPMD and CMD methods give very similar results. From a further analysis based on quantum transition state theory (centroid density QTST) combined with path integral molecular dynamics (PIMD), it has been clear that there is a

crossover between thermal and quantum mechanisms at about  $T = 500$  K and 300 K for H and T diffusions, respectively. The importance of nuclear quantum effects at low temperatures has been illustrated in terms of the effective free energy surface map.

### **Nonadiabatic relaxation dynamics of excited hydrated electron cluster**

We have applied a recently-developed hybrid quantum ring-polymer molecular dynamics (RPMD) method to nonadiabatic  $p \rightarrow s$  relaxation dynamics in water anion clusters in order to understand the isotope effects observed in previous experiments. The average relaxation times for  $(\text{H}_2\text{O})_{50}^-$  and  $(\text{D}_2\text{O})_{50}^-$  were calculated to be 120 and 207 fs, respectively, and are comparable to experimental results. Therefore, we conclude that nuclear quantum effects are playing an essential role in the structural rearrangement dynamics of water anion clusters. The detailed nonadiabatic relaxation mechanisms are also discussed.

## Publication list

- [1] T. Takayanagi, T. Yoshikawa, A. Kakizaki, M. Shiga, M. Tachikawa, "Molecular dynamics simulations of small glycine-(H<sub>2</sub>O)<sub>n</sub> (n = 2–7) clusters on semiempirical PM6 potential energy surfaces," *J. Mol. Struct. (THEOCHEM)* **869** (2008) 29-36.
- [2] A. Kakizaki, H. Motegi, T. Yoshikawa, T. Takayanagi, M. Shiga, M. Tachikawa, "Path-integral molecular dynamics simulations of small hydrated sulfuric acid clusters H<sub>2</sub>SO<sub>4</sub>\*(H<sub>2</sub>O)<sub>n</sub> (n = 1–6) on semiempirical PM6 potential surfaces," *J. Mol. Struct. (THEOCHEM)* **901** (2009) 1-8.
- [3] T. Yoshikawa, H. Motegi, A. Kakizaki, T. Takayanagi, M. Shiga, M. Tachikawa, "Path-integral molecular dynamics simulations of glycine-(H<sub>2</sub>O)<sub>n</sub> (n = 1–7) clusters on semiempirical PM6 potential energy surfaces," *Chem. Phys.* **365** (2009) 60-68.
- [4] T. Takayanagi, T. Yoshikawa, H. Motegi, M. Shiga, "Path-integral molecular dynamics simulations for water anion clusters (H<sub>2</sub>O)<sub>5</sub><sup>-</sup> and (D<sub>2</sub>O)<sub>5</sub><sup>-</sup>," *Chem. Phys. Lett.* **482** (2009) 195-200.
- [5] T. Yoshikawa, S. Sugawara, T. Takayanagi, M. Shiga, M. Tachikawa, "Theoretical study on the mechanism of double proton transfer in porphycene by path-integral molecular dynamics simulations," *Chem. Phys. Lett.* **496** (2010) 14-19.
- [6] T. Yoshikawa, T. Takayanagi, M. Tachikawa, S. Sugawara, "Theoretical study on mechanisms of structural rearrangement and ionic dissociation in the HCl(H<sub>2</sub>O)<sub>4</sub> cluster with path-integral molecular dynamics simulations," *Chem. Phys. Lett.* **501** (2011) 238-244.
- [7] S. Sugawara, T. Yoshikawa, T. Takayanagi, M. Shiga, M. Tachikawa, "Quantum proton transfer in hydrated sulfuric acid clusters: A perspective from semiempirical path integral simulations," *J. Phys. Chem. A* **115** (2011) 11486-11494.
- [8] T. Yoshikawa, S. Sugawara, T. Takayanagi, M. Shiga, M. Tachikawa, "Quantum tautomerization in porphycene and its isotopomers: Path integral molecular dynamics simulations," *Chem. Phys.* **394** (2012) 46-51.
- [9] T. Yoshikawa, T. Takayanagi, H. Kimizuka, M. Shiga, "Quantum-Thermal Crossover of Hydrogen and Tritium Diffusion in  $\alpha$ -Iron," *J. Phys. Chem. C* **116** (2012) 23113-23119.

- [10] T. Yoshikawa, T. Takayanagi, "Application of ring-polymer molecular dynamics to electronically nonadiabatic excess electron dynamics in water clusters: importance of nuclear quantum effects," *Chem. Phys. Lett.* **564** (2013) 1-5.
- [11] Y. Sugioka, T. Yoshikawa, T. Takayanagi, "Theoretical Study of Excess Electron Attachment Dynamics to the Guanine-cytosine Base Pair: Electronic Structure Calculations and Ring-polymer Molecular Dynamics Simulations," *J. Phys. Chem.* **117** (2013) 11403-11410.
- [12] T. Yoshikawa, T. Takayanagi, "Non-adiabatic relaxation dynamics of water anion cluster and its isotope effects by ring-polymer molecular dynamics simulation," *Int. J. Quant. Chem.* *as soon as published*.

# Acknowledgement

*First and foremost, I would like to express my thanks to my supervisor,*

*Prof. Toshiyuki Takayangi, for his suggestions, comments, patience and understanding.*

*I am glad that your door is always open, as I greatly value your opinion and input, and have always enjoyed our (scientific) discussions.*

*I am deeply grateful to my thesis committee members,*

*Dr. Yousoo Kim, Prof. Masayuki Hutamata, and Prof. Shunji Honma.*

*I wish to express my sincere thanks to Dr. Motoyuki Shiga, Prof. Masanori Tachikawa, Prof. Hajime Kimizuka, Prof. Takuji Oda, and Dr. Takanori Kobayashi.*

*I never forget the scientific discussions, helpful suggestions and encouragements with them.*

*Very special thanks to present and past laboratory members.*

*The work presented in this thesis would not have been possible without them.*

*I take this opportunity to extend my sincere gratitude and appreciation to all those who made this Ph.D thesis possible.*

# Contents

1	Introduction	1
1.1	Importance of nuclear quantum effects in light particle transfer reactions	1
1.2	Quantum simulation methods	4
1.3	References	5
2	Quantum simulation methods for understanding the hydrogen and proton Dynamics	7
2.1	Path-integral molecular dynamics (PIMD)	7
2.2	Harmonic oscillator	9
2.3	Centroid molecular dynamics (CMD)	10
2.4	Ring-polymer molecular dynamics (RPMD)	11
2.5	Efficiency and applicability	12
2.6	References	16
3	Double Proton Transfer Mechanism in Porphycene	19
3.1	Multiple proton transfer	19
3.2	Intramolecular double proton transfer in porphycene	20
3.3	Methods	22
3.3.1	Semiempirical PM6 method	22
3.3.2	Application of specific reaction parameter method to the PM6	23
3.3.3	Simulation conditions	26
3.4	Potential energy surface of double proton transfer for porphycene	26
3.5	Proton density distribution for HH-porphycene	28
3.6	PIMD vs classical MD for two-dimensional proton density distribution in HH-porphycene	28
3.7	Proton density distribution for isotopic-substituted porphycenes	31
3.8	Two-dimensional proton density distributions for isotopic substituted porphycenes	33
3.9	Free energy surface for the double proton transfer	33

3.10	Correlation of the inner nitrogen motion with the proton transfer and its isotope effects	37
3.11	References	39
4	Diffusion of Hydrogen/Tritium in Fe (bcc) lattice	43
4.1	Hydrogen/Tritium in Metal	43
4.2	Diffusion of hydrogen and tritium atom in pure Fe metal	44
4.3	Methods	45
4.3.1	Embedded atom model potential function for Fe lattice.	45
4.3.2	Potential energy surface on Fe (100) plane	47
4.3.3	Estimation of diffusion constant	49
4.3.4	Simulation conditions	49
4.4	Diffusion constants obtained from RPMD, CMD and classical MD simulations	50
4.5	Arrhenius plots of diffusion constants	53
4.6	Three dimensional perspective plots	54
4.7	Free energy surfaces on Fe (100) plane	55
4.8	Quantum transition state theory	58
4.9	References	61
5	Non-Adiabatic Relaxation Dynamics of Hydrated Electron Cluster	66
5.1	Hydrated electron	66
5.2	Non-adiabatic relaxation dynamics of excited-state hydrated electron and its isotope effects	67
5.3	Development of RPMD method for describing the non-adiabatic relaxation dynamics	69
5.3.1	One electron wave packet propagation method	70
5.3.2	Hybrid of RPMD with wave packet propagation method	70
5.4	Methods	72
5.4.1	TB pseudo-potential function for the interaction between an excess electron and water molecules	72
5.4.2	RWK2-M model potential for the interaction between water molecules	74
5.4.3	Simulation condition	75
5.5	Snapshots of the relaxation dynamics along the representative RPMD trajectory	76

5.6	Temporal changes of physical quantities along the representative RPMD trajectory	77
5.7	Statistical aspects of the survival probability and VDE for all trajectories of both $(\text{H}_2\text{O})_{50}^-$ and $(\text{D}_2\text{O})_{50}^-$	79
5.8	RPMD lifetimes obtained from a different scheme	83
5.9	Detailed nonadiabatic relaxation mechanisms	83
5.10	References	86
6	General Conclusions	90
6.1	Conclusion for chapter 3	90
6.2	Conclusion for chapter 4	91
6.3	Conclusion for chapter 5	91
	Appendices	93
A	Velocity Verlet algorithm	93
B	Discrete Variable Representation (DVR)	94



# Chapter 1

## Introduction

Although it has been generally accepted that nuclear quantum effects, including tunneling and vibrational quantization, are playing very important roles in light particle transfer reactions, their role has not yet been fully understood in complicated chemical reaction systems. This is simply because it is very difficult to solve quantum mechanical equations of motions for complicated systems due to huge number of degrees of freedom. In this work, in order to understand nuclear quantum effects in general chemical reactions containing many atoms from the theoretical side, we apply path-integral based computational methods, which can be applied to complicated systems. In particular, we would like to demonstrate that various isotope effects seen in many chemical dynamical systems cannot be understood without considerations of nuclear quantum effects.

Notice that we have used the following constants without notice in this paper;

$\hbar$  Dirac constant

$k_B$  Boltzmann constant

### 1.1 Importance of nuclear quantum effects in light particle transfer reactions

The importance of nuclear quantum effects in light particle transfer reactions can be understood from the schematic potential energy curve presented in Fig. 1-1. In this figure, the reactant to transition state region of a typical hydrogen (deuterium) transfer reaction  $\text{H-A (D-A)} + \text{B} \rightarrow \text{A} + \text{H-B (D-B)}$  is shown. Also shown are quantized

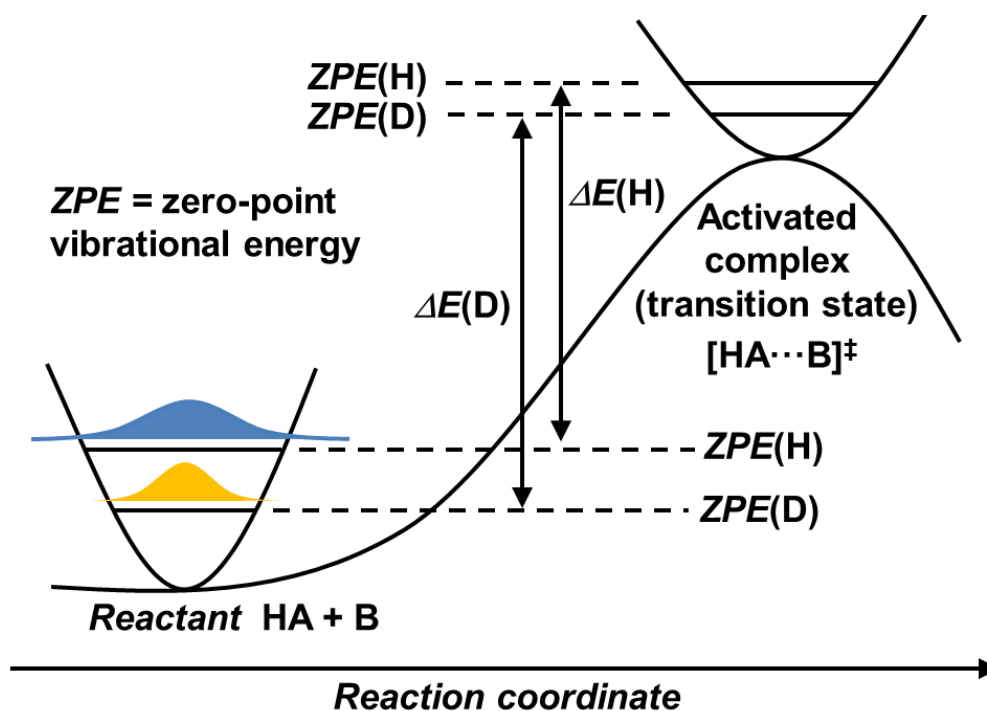


Fig. 1-1 The reaction region of the hydrogen (deuterium) transfer reaction A-H (A-D) + B  $\rightarrow$  A + H-B (D-B) with quantized-vibrational energy levels. The  $\Delta E$  is relative energy between the reactant and activated complex with ZPE. The zero-point vibrational amplitudes of hydrogen and deuterium in the reactant are described as blue and yellow, respectively.

zero-point energy levels for the reactant H-A (D-A) and for transition state. Since the magnitude of zero-point energy (ZPE) is dependent of atomic mass, the activation energy  $\Delta E$ , which is the difference between the reactant and transition state vibrational energy levels between zero-point vibrational energies, is also dependent of atomic mass.

Fig. 1-2 displays Arrhenius plot of rate constants of a certain chemical reaction. In addition to the above-mentioned isotopic ZPE difference, quantum tunneling significantly affects thermal physical quantities including rate constants as well diffusion coefficients. It is frequently seen that such physical quantities show a linear behavior in Arrhenius plot; however, accurate quantum mechanical theory predicts strongly curved behaviors in Arrhenius plot at lower temperatures due to quantum tunneling. The importance of quantum tunneling at lower temperatures can be

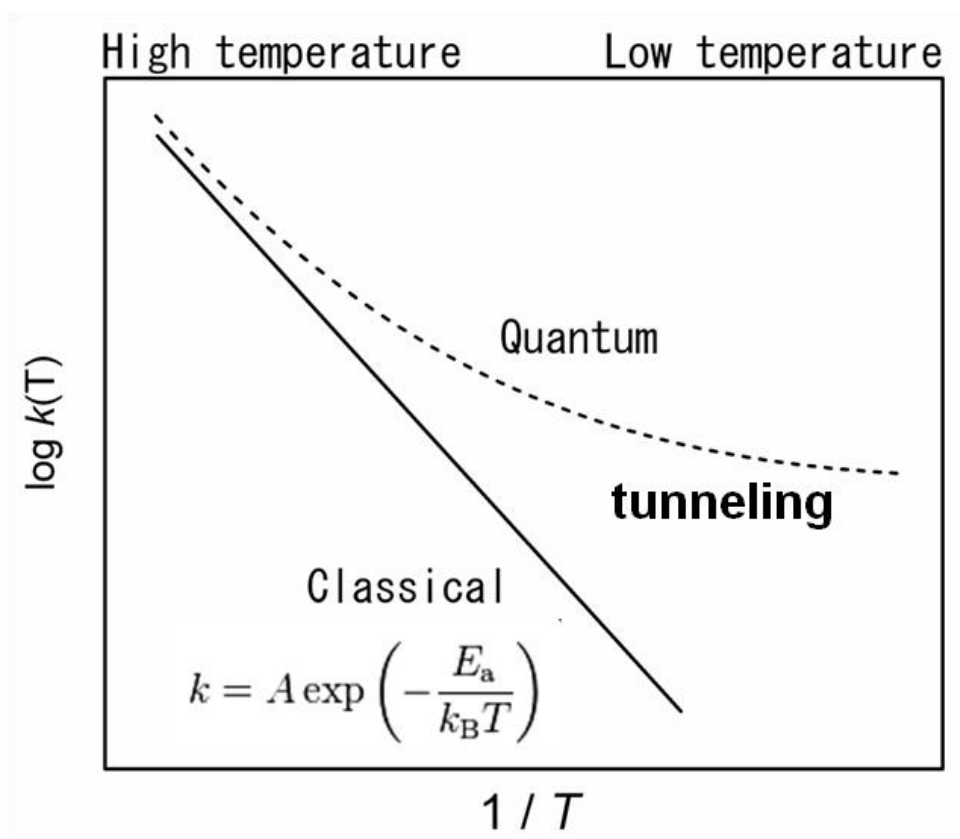


Fig. 1-2 The Arrhenius plot of rate constant as a function of inversed temperature  $1/T$ . Solid line and broken line are denoted as classical and quantum mechanical results, respectively. Arrhenius equation is also shown in this figure.

understood in terms of thermal de Broglie wavelength,  $\Lambda$ , defined as

$$\Lambda = (2\pi\hbar^2/mk_B T)^{1/2} \quad (1-1)$$

where  $m$  and  $T$  are denoted as particle mass and temperature, respectively. As temperature is lowered, thermal de Broglie wavelength becomes much longer. Thus, light particles, such as hydrogen atoms can easily penetrate a classically forbidden region of a potential energy interaction. As a result, for example, Arrhenius plots of rate constants obtained from classical mechanics and quantum mechanics frequently show completely different behaviors especially at low temperatures.

Fig. 1-3 shows the two-dimensional proton density distributions in the  $N_2H_7^+$  and  $N_2D_7^+$  ionic molecules obtained from quantum mechanical simulations [13]. This figure shows thermal distributions at  $T = 300$  K. It is clearly seen that the proton

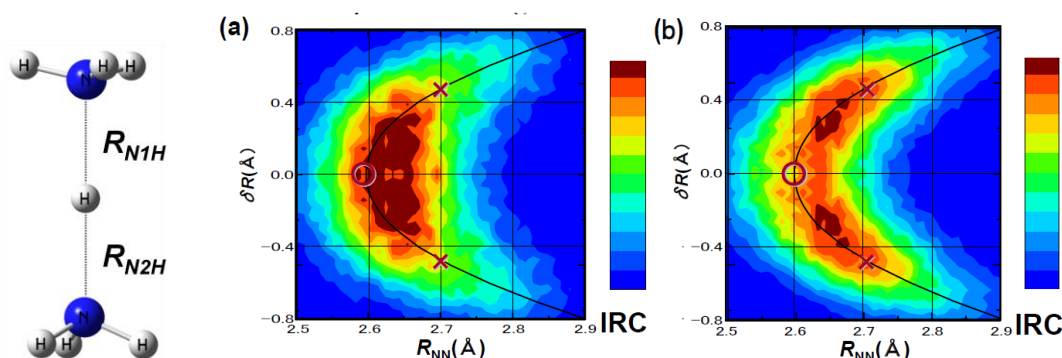


Fig. 1-3. Two-dimensional proton density distributions as a function of  $R_{NN}$  vs  $\delta R_{NH/ND}$  for (a)  $\text{N}_2\text{H}_7^+$  and (b)  $\text{N}_2\text{D}_7^+$  at 300 K. Notice that  $\delta R_{NH}$  is defined as  $R_{N2H} - R_{N1H}$ . Crosses and circle indicate a point of equilibrium structure and TS, respectively @Copyright 2006 Society of Computer Chemistry, Japan.

distribution in  $\text{N}_2\text{H}_7^+$  is quite different from that in  $\text{N}_2\text{D}_7^+$  because of a large amplitude motion of proton. This result indicates that isotopic substitution can sometimes affect molecular geometry and thus molecular property. The former phenomenon is called an “geometric isotope effect.”

In summary, it should be emphasized that nuclear quantum effects should be taken into account for understanding various isotope effects seen in extensive chemical dynamics phenomena.

## 1.2 Quantum Simulation methods

An accurate quantum mechanical picture can be obtained by exactly solving the Schrödinger equations for a certain system. However, it is very difficult to solve the equations except for simple chemical systems containing only a few atoms. In order to understand the quantum mechanical nature of complicated chemical reaction systems, one has to employ approximate quantum mechanical methods. In this work, we employ approximate methods based on path-integral formalism. In the next section, we will briefly explain the theoretical methods used in this work, including path integral molecular dynamics (PIMD), ring-polymer molecular dynamics (RPMD) and centroid molecular dynamics methods (CMD).

### 1.3 References

- [1] S. N. Smirnov, N. S. Golubev, G. S. Denisov, H. Benedict, P. Schah-Mohammedi, H. -H. Limbach, "Hydrogen/Deuterium Isotope Effects on the NMR Chemical Shifts and Geometries of Intermolecular Low-Barrier Hydrogen-Bonded Complexes" *J. Am. Chem. Soc.* **118** (1996) 4094-4101.
- [2] A. Douhal, F. Lahmani, A. H. Zewail, "Proton-transfer reaction dynamics" *Chem. Phys.* **207** (1996) 477-498.
- [3] J. T. Hynes, J. P. Klinman, H. -H. Limbach, R. L. Schowen, "Single and Multiple Hydrogen/Deuterium Transfer Reactions in Liquids and Solids" *Hydrogen-Transfer Reactions*, Wiley-VCH, Weinheim, Germany, 2007.
- [4] A. Vdovin, J. Waluk, B. Dick, A. Slenczka, "Mode-Selective Promotion and Isotope Effects of Concerted Double-Hydrogen Tunneling in Porphycene Embedded in Superfluid Helium Nanodroplets" *ChemPhysChem* **10** (2009) 761-765.
- [5] R. M. Balabin, "The First Step in Glycine Solvation: The Glycine-Water Complex" *J. Phys. Chem. B* **114** (2010) 15075-15078.
- [6] S. Gawinkowski, Ł. Walewski, A. Vdovin, A. Slenczka, S. Rols, M. R. Johnson, B. Lesyng, J. Waluk, "Vibrations and hydrogen bonding in porphycene" *Phys. Chem. Chem. Phys.* **14** (2012) 5489-5503.
- [7] M. J. Gillan, "Quantum simulation of hydrogen in metals" *Phys. Rev. Lett.* **58** (1987) 563.
- [8] N. Agmon, "The Grotthuss mechanism" *Chem. Phys. Lett.* **244** (1995) 456-462.
- [9] S. H.-Schiffer, "Theoretical Perspectives on Proton-Coupled Electron Transfer Reactions" *Acc. Chem. Res.* **34** (2001) 273-281.
- [10] Q. Cui, M. Karplus, "Is a 'Proton Wire' Concerted or Stepwise? A Model Study of Proton Transfer in Carbonic Anhydrase" *J. Phys. Chem. B* **107**, (2003), 1071-1078.
- [11] G. A. Voth, "Computer Simulation of Proton Solvation and Transport in Aqueous and Biomolecular Systems" *Acc. Chem. Res.* **39** (2006) 143-150.
- [12] T. E. Markland, S. Habershon, D. E. Manolopoulos, "Quantum diffusion of hydrogen and muonium atoms in liquid water and hexagonal ice" *J. Chem. Phys.* **128** (2008) 194506.

- [13] H. Ishibashi, A. Hayashi, M. Shiga, M. Tachikawa, “Geometric Isotope Effect on the  $\text{N}_2\text{H}_7^+$  Cation and  $\text{N}_2\text{H}_5^-$  Anion by *Ab Initio* Path Integral Molecular Dynamics Simulation” *ChemPhysChem* **9** (2008) 383-387.
- [14] T. Takayanagi, T. Yoshikawa, H. Motegi, M. Shiga, “Path-integral molecular dynamics simulations for water anion clusters  $(\text{H}_2\text{O})_5^-$  and  $(\text{D}_2\text{O})_5^-$ ” *Chem. Phys. Lett.* **482** (2009) 195-200.

# Chapter 2

## Simulation methods for quantum dynamics

In this chapter, we present three quantum mechanical methods, path-integral molecular dynamics (PIMD) [1-6], centroid molecular dynamics (CMD) methods [5,6-10] and ring-polymer molecular dynamics (RPMD) [5,6,11-14]. All these methods are based on Feynman path-integral formalism and quantum nature of a particle is treated with ring-polymer beads [1,2]. With the PIMD method, one can obtain thermal-equilibrium configuration including nuclear quantum effects but we cannot obtain information of time-dependent physical quantities. On the other hand, both the CMD and RPMD can give time-dependent physical quantities such as rate constants and diffusion coefficients. In the CMD method, time-evolution of the centroid position of the ring-polymer is calculated while, in RPMD, time evolution for all polymer beads is calculated. We also describe the efficiency and applicability of these three methods. We will apply these three simulation methods for the chemical systems presented in Chapters 3-5.

### 2.1 Path-integral molecular dynamics (PIMD)

The quantum partition function  $Z$  in the canonical (NVT) ensemble for a molecular system with inverse thermal energy  $\beta = 1/k_B T$  is defined as the trace of Boltzmann operator [1-6] as

$$Z(\beta) = \iint dx dp \exp(-\beta \hat{H}) = \text{Tr}[\exp(-\beta \hat{H})], \quad (2-1)$$

where Hamiltonian operator  $\hat{H}$  is defined as  $\hat{H} = \frac{\hat{p}^2}{2m'} + \hat{V}(x)$ .  $\hat{p}$  and  $\hat{x}$  are the momentum and position operators, respectively with  $\hat{p} = -i\hbar \frac{\partial}{\partial x}$ . However, it is

generally difficult to accurately calculate the value of  $Z$  for large systems due to a huge computational cost. We focus on the path-integral theory (PI) and present the PI expression of quantum partition function for single particle. The position representation of Eq. (2-1) is described as

$$Z(\beta) = \int dx \langle x | \mathbf{exp}(-\beta\hat{H}) | x \rangle . \quad (2-2)$$

In order to obtain the quantum partition function, with split-operator method the total Hamiltonian of Eq. (2-2) is described as

$$\langle x' | \mathbf{exp}(-\beta\hat{H}) | x \rangle \approx \langle x' | \mathbf{exp}(-\beta\hat{V}/2) \mathbf{exp}(-\beta\hat{T}) \mathbf{exp}(-\beta\hat{V}/2) | x \rangle \quad (2-3a)$$

$$= \langle x' | \mathbf{exp}(-\beta\hat{V}/2) | x' \rangle \langle x' | \mathbf{exp}(-\beta\hat{T}) | x \rangle \langle x | \mathbf{exp}(-\beta\hat{V}/2) | x \rangle \quad (2-3b)$$

$$= \mathbf{exp}(-\beta\hat{V}(x')/2) \langle x' | \mathbf{exp}(-\beta\hat{T}) | x \rangle \mathbf{exp}(-\beta\hat{V}(x)/2) \quad (2-3c)$$

$$= \int dp \mathbf{exp}(-\beta(\hat{V}(x') + \hat{V}(x))/2) \langle x' | \mathbf{exp}(-\beta\hat{T}) | p \rangle \langle p | x \rangle \quad (2-3d)$$

$$= \int dp \mathbf{exp}(-\beta(\hat{V}(x') + \hat{V}(x))/2) \langle x' | p \rangle \mathbf{exp}(-\beta p^2/2m) \langle p | x \rangle \quad (2-3e)$$

$$= \frac{1}{\sqrt{2\pi\hbar}} \int dp \mathbf{exp}(-\beta(\hat{V}(x') + \hat{V}(x))/2 + p^2/2m) \mathbf{exp}(ip(x-x')/\hbar) \quad (2-3f)$$

$$= \sqrt{\frac{m}{2\pi\beta\hbar^2}} \mathbf{exp}\left(-\frac{m}{2\beta\hbar^2}(x'-x)^2 - \beta \frac{(\hat{V}(x') + \hat{V}(x))}{2}\right) . \quad (2-3g)$$

Here, in order to derive Eq. (2-3g), we have used the following five relations as:

$$\int dx_i |x_i\rangle \langle x_i| = 1 \quad (2-4)$$

$$\int dp_i |p_i\rangle \langle p_i| = 1 \quad (2-5)$$

$$\langle x | p \rangle = \frac{1}{\sqrt{2\pi\hbar}} \mathbf{exp}(ipx/\hbar) \quad (2-6)$$

$$\mathbf{exp}(-\beta\hat{V} | x \rangle = \mathbf{exp}(-\beta V(x)) | x \rangle \quad (2-7)$$

$$\mathbf{exp}(-\beta\hat{p}^2/2m) | p \rangle = \mathbf{exp}(-\beta p^2/2m) | p \rangle \quad (2-8)$$

In addition, using Suzuki-Trotter decomposition [1-6], the PI representation of quantum partition function  $Z_p$  in Eq. (2-2) can be rewritten as

$$Z_p(\beta) = \int dx \langle x | \mathbf{exp}(-\beta\hat{H}) | x \rangle \quad (2-9)$$

$$= \int dx \langle x | \mathbf{exp}(-\beta\hat{H}/2) | x' \rangle \langle x' | \mathbf{exp}(-\beta\hat{H}/2) | x \rangle \quad (2-10)$$

$$= \int dx_1 \cdots x_p \langle x_1 | \mathbf{exp}(-\beta_p \hat{H}/2) | x_2 \rangle \cdots \langle x_p | \mathbf{exp}(-\beta_p \hat{H}/2) | x_1 \rangle \quad (2-11)$$

where  $P$  and  $\beta_p$  are the number of beads and  $\beta/P$ , respectively. From Eqs. (2-3g) and (2-11), we can derive Eq. (2-12) as:

$$Z_P(\beta) = \left( \frac{mP}{2\pi\beta\hbar^2} \right)^{P/2} \int dx_1, \dots, dx_P \exp \left\{ -\beta_P \sum_{k=1}^P \left[ \frac{1}{2} m\omega_P^2 (x_k - x_{k+1})^2 + \frac{1}{P} V(x_k) \right] \right\} \quad (2-12)$$

where  $\omega_P = \frac{\sqrt{P}}{\beta\hbar}$  and  $\mathbf{x}_{k+1} = \mathbf{x}_1$ . A conceptual image of Eq. (2-12) is shown in Fig. 2-1.

Without changing any of the thermal-equilibrium properties of the molecular system, we can introduce a set of  $P$  uncoupled Gaussian integrals as follows:

$$Z_P(\beta) = \int d\mathbf{p}_{1,1}, \dots, d\mathbf{p}_{N,P} \int d\mathbf{x}_{1,1}, \dots, d\mathbf{x}_{N,P} \exp(-\beta H_P(\mathbf{x}_{1,1}, \dots, \mathbf{x}_{N,P}, \mathbf{p}_{1,1}, \dots, \mathbf{p}_{N,P})) \quad (2-13)$$

$$= \int d\mathbf{p}_{1,1}, \dots, d\mathbf{p}_{N,P} \int d\mathbf{x}_{1,1}, \dots, d\mathbf{x}_{N,P} \times \exp \left\{ -\beta_P \sum_{k=1}^P \left[ \frac{\mathbf{p}_k^2}{2m'_k} + \frac{1}{P} V(\mathbf{x}_k) + \frac{1}{2} m\omega_P^2 (\mathbf{x}_k - \mathbf{x}_{k+1})^2 \right] \right\} \quad (2-14)$$

From Eq. (2-13), the effective PI Hamiltonian can be described as:

$$H_{eff} = \sum_{k=1}^P \left[ \frac{\mathbf{p}_k^2}{2m'_k} + \frac{1}{P} V(\mathbf{x}_k) + \frac{1}{2} m\omega_P^2 (\mathbf{x}_k - \mathbf{x}_{k+1})^2 \right] \quad (2-15)$$

The quantum partition function in the PI representation can be obtained by using an effective Hamiltonian in Eq. (2-15). Although PIMD cannot give time-dependent dynamical quantities such as rate constants and diffusion constants, it can give thermal-equilibrium configurations.

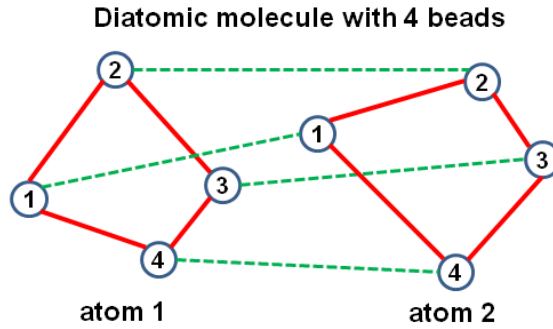


Fig. 2-1. Conceptual image of a diatomic molecular system with 4 beads. Red straight and green break lines are denoted as harmonic oscillators and interactions of atoms, respectively.

## 2.2 Harmonic oscillator

Eq. (2-15) can be rewritten as

$$H_{\text{eff}} = \sum_{k=1}^P \left[ \frac{\mathbf{p}_k^2}{2m'_k} + \frac{1}{P} V(x_k(\{\mathbf{Q}\})) + \frac{1}{2} m_k \omega_P^2 \mathbf{q}_k^2 \right] \quad (2-16a)$$

$$\mathbf{q}_1 = \mathbf{x}_1 \quad (2-16b)$$

$$\mathbf{q}_k = \mathbf{x}_k - \frac{(k-1)\mathbf{x}_{k+1} + \mathbf{x}_1}{k}, \quad k = 2, \dots, P \quad (2-16c)$$

$$m_1 = 0 \quad (2-16d)$$

$$m_k = \frac{k}{k-1} m \quad (2-16e)$$

where  $x_k(\{\mathbf{Q}\})$  is the inverse transformation. The third term in Eq. (2-16a) means the quantum harmonic oscillator and is expressed as

$$q_k = \frac{1}{\sqrt{P}} \sum_{i=1}^P U_{ki} x_i \quad (2-17)$$

where  $U_{ki}$  is a unitary matrix which can diagonalize  $A_{ij} = (2\delta_{i,j} - \delta_{i,j+1} - \delta_{i,j-1})$  with  $A_{ij+1} = A_{i1}$ ,  $A_{i0} = A_{iP}$  and its eigenvalue is  $\lambda_k$ . Eqs. (2-16b)-(2-16e) are rewritten as

$$m_k = m\lambda_k \quad (2-18)$$

$$\lambda_{2k-1} = \lambda_{2k-2} = 2P \left[ 1 - \cos\left(\frac{2\pi(k-1)}{P}\right) \right] \quad (2-19)$$

$$q_1 = x_0 = \frac{1}{P} \sum_{i=1}^P x_i. \quad (2-20)$$

Here,  $\lambda_1 = 0$  and  $\lambda_P = 4P$ . The fictitious masses  $m'_k$  in Eq. (2-15) are chosen according to  $m'_k = m_k$  and  $m'_1 = m$ . By transforming the harmonic oscillator formula, PIMD can efficiently yield the quantum partition function of many-body systems.

### 2.3 Centroid molecular dynamics (CMD)

Cao and Voth have developed CMD as a quasi-classical approximation method to calculate real-time quantum correlation functions [5,6,11,12]. CMD is based on the concept of centroid variables which are the center-of-mass positions of the ring polymers (see also Eq. (2-20)). The time-evolution of CMD is described by using the equation-of-motion of the centroid as follows:

$$\dot{x}_c = \frac{p_c}{m} \quad (2-21)$$

$$F_o(x_c) \equiv \dot{p}_c = -\frac{dV_o(x_c)}{dx_c} \quad (2-22)$$

$$p_c = p_o = \frac{1}{P} \sum_{i=1}^P p_i, \quad (2-23)$$

where  $m$  is physical mass.  $V_o(x_c)$  is the mean-field potential acting on the centroid, and defined as

$$V_o(x_c) = -\frac{1}{\beta} \ln \left\{ \left( \frac{2\pi\beta\hbar^2}{m} \right)^{1/2} \oint \mathcal{D}x(\tau) \delta(x_o[x(\tau)] - x_c) e^{-S[x(\tau)]/\hbar} \right\} \quad (2-24)$$

$$x_o[x(\tau)] = \frac{1}{\beta\hbar} \int_0^{\beta\hbar} x(\tau) d\tau \approx \frac{1}{P} \sum_{i=1}^P x(\tau_i) \quad (2-25)$$

Eq. (2-22) is also rewritten as

$$F_o(x_c) = -\frac{\oint \mathcal{D}x(\tau) \delta(x_o[x(\tau)] - x_c) \left[ \frac{1}{\beta\hbar} \int_0^{\beta\hbar} \frac{dV}{dx(\tau')} d\tau' \right] e^{-S[x(\tau)]/\hbar}}{\oint \mathcal{D}x(\tau) \delta(x_o[x(\tau)] - x_c) e^{-S[x(\tau)]/\hbar}} \quad (2-26)$$

In addition, the partition function in the CMD method is described as

$$Z(\beta) = \int x_c \int p_c \frac{dx_c dp_c}{2\pi\hbar} \rho_c(x_c) \mathbf{exp}\left(-\frac{\beta p_c^2}{2m}\right) \quad (2-27)$$

$$\rho_c(x_c) = \mathbf{exp}\left(-\beta\left(\frac{1}{P} V(x_k(\{Q\})) + \frac{1}{2} m_k \omega_P^2 q_k^2\right)\right) \quad (2-28)$$

The quantum expressions of CMD are exact but Eqs. (2-24)-(2-26) are of limited use. Their evaluation is not feasible for complex systems due to necessary of a full PI calculation at each centroid configuration.

## 2.4 Ring-polymer molecular dynamics (RPMD)

RPMD is an approximate real-time quantum dynamics simulation method and has been developed recently by Craig and Manolopoulos [5,6,13-16]. There have been three differences between CMD and RPMD. First, physical mass is used in RPMD while PIMD and CMD employ the fictitious mass (see also Eq. (2-18)). Second, expectation

values in RPMD are estimated by using the average of ring-polymer beads.

$$O_p(t) = \frac{1}{P} \sum_{i=1}^P O(x_i(t)) \quad (2-29)$$

RPMD can approximately describe the Kubo-transformed velocity autocorrelation function as

$$K_{vv}(t) \approx \frac{1}{(2\pi\hbar)^P Z_p(\beta)} \int dx \int dp v_p(0) v_p(t) e^{-\beta p H_p(x,p)} \quad (2-30)$$

$$H_p(\mathbf{x}, \mathbf{p}) = \sum_{j=1}^P \frac{p_j^2}{2m} + \frac{m}{2\beta_p^2 \hbar^2} \sum_{j=1}^P (x_j - x_{j-1})^2 + \sum_{j=1}^P V(x_j). \quad (2-31)$$

This means that RPMD can yield simulation results in quantum dynamics manner.

Third, the equation-of-motion of all polymer beads in RPMD obeys Newton's law.

$$\dot{p}_j = -\frac{m}{\beta_p^2 \hbar} [2x_j - x_{j-1} - x_{j+1}] - \frac{\partial V}{\partial x_j} \quad (2-32)$$

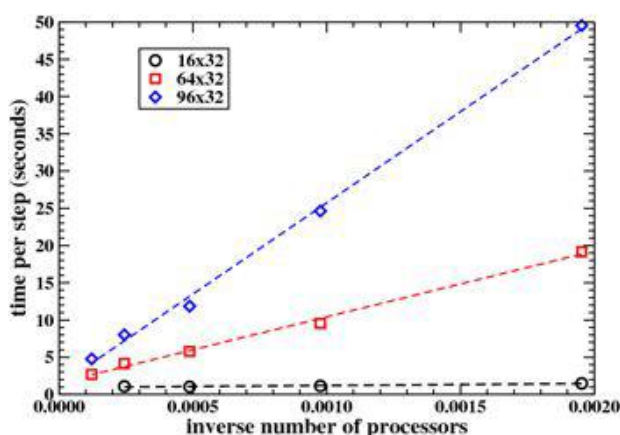
$$\dot{x}_j = \frac{p_j}{m} \quad (2-33)$$

## 2.5 Efficiency and applicability

The MD methods based on the PI theory are very useful because these methods can yield quantum-mechanical results from classical-like MD simulations although a large number of beads is generally required to obtain converged results. Fortunately, parallel efficiency of PIMD, CMD and RPMD simulations is very high. Fig. 2-2 shows the parallel efficiency with 16-96 beads [17]. The computational time of these simulations can be reduced as the number of processor increases. Fig. 2-3 displays the plots of the energy of an isolated water monomer as a function of the number of beads [18]. The energy convergence can clearly be seen as the number of beads increases. Therefore, PIMD, CMD and RPMD are powerful tools for understanding quantum nature of hydrogen and proton dynamics as well as of other isotopes.

Fig. 2-4 shows radial distribution functions of  $r_{OO}$ ,  $r_{OH}$  and  $r_{HH}$  [18]. We can see that radial distribution functions of PIMD are consistent with the experimental results,

and are much broader than classical MD results. In order to compare RPMD with CMD, self-diffusion coefficients for low pressure liquid *para*-hydrogen at  $T = 25$  and 14 K are shown in Table. 2-1 [19]. Diffusion coefficients of RPMD and CMD are consistent with available experiments and the RPMD results are very similar to those from CMD. Therefore, hydrogen and proton dynamics can be described by using these simulation methods. We will apply these simulation tools to three systems; (1) porphycene (Chapter 3), (2) hydrogen and tritium diffusion in Fe (Chapter 4) and (3) hydrated electron cluster (Chapter 5).



No. Proc.	16 × 32 molecules (1536 atoms)	64 × 32 molecules (6144 atoms)	96 × 32 molecules (9216 atoms)
512	1.49 sec	19.16 sec	49.54 sec
1024	1.14 sec	9.54 sec	24.63 sec
2048	1.03 sec	5.79 sec	11.86 sec
4096	1.09 sec	4.16 sec	8.02 sec
8192	—	2.70 sec	4.77 sec

Fig. 2-2. The parallel efficiency for the number of beads with calculation times. These results are obtained from calculations of 32 SPC/F2 water molecules with 16 beads (Left column), 64 beads (middle column) and 96 beads (right column). Notice that calculation time is 2.22 sec on 1 processor. @ Copyright Columbia University.

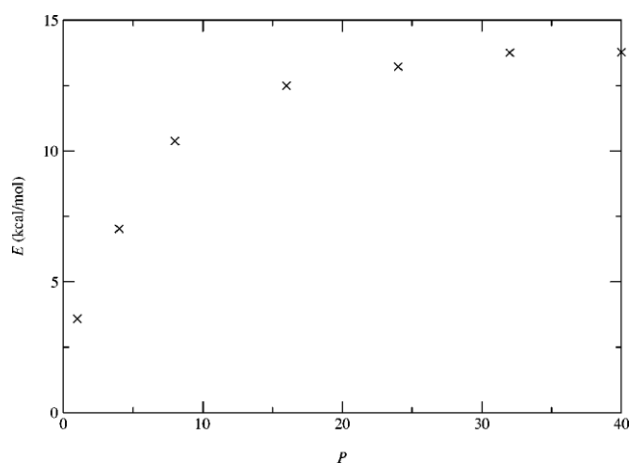


Fig. 2-3. Energy of an isolated water monomer,  $E$ , as a function of the number of beads  $P$  used in a PIMD simulation in the canonical ensemble at 298.15 K. The number of water molecules is 125. @ Copyright 2001 American Institute of Physics.

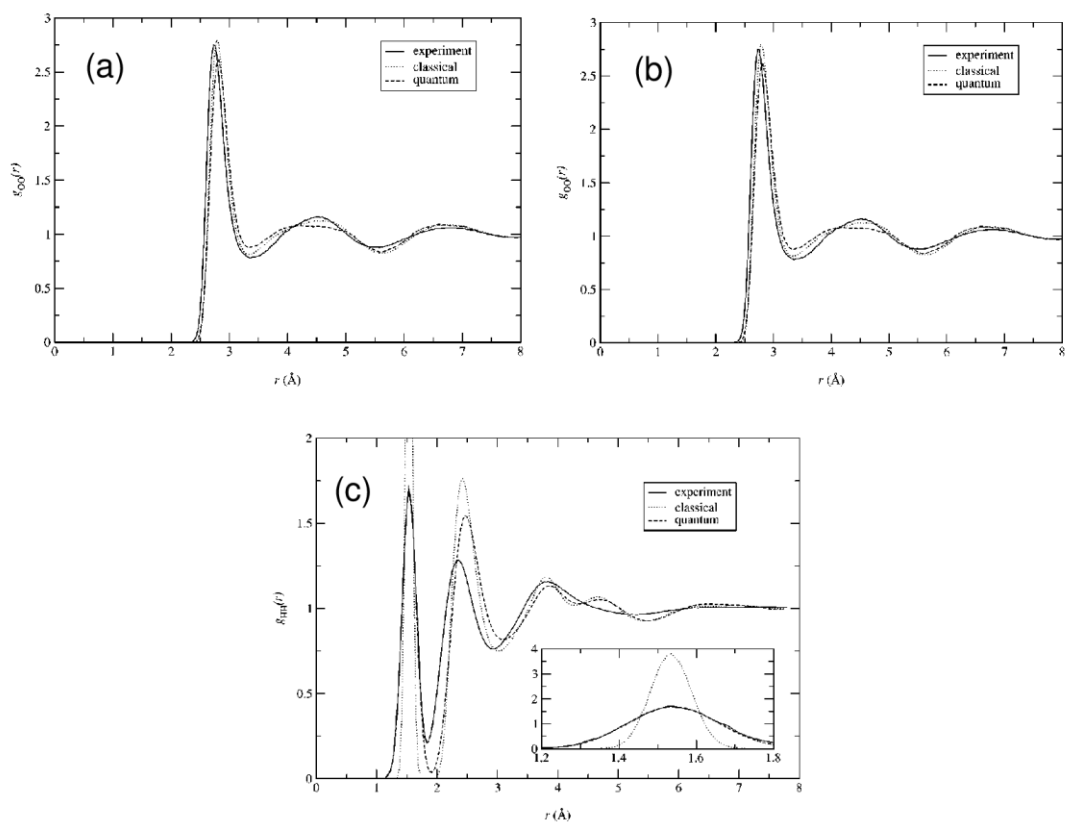


Fig. 2-4. The radial distribution functions of (a)  $r_{OO}$ , (b)  $r_{OH}$ , (c)  $r_{HH}$  as the same molecular system in Fig. 2-3 @ Copyright 2001 American Institute of Physics.

TABLE 2-1. Calculated and experimental self-diffusion coefficients for low pressure liquid *para*-hydrogen at 25 and 14 K. (The numbers in parentheses are the estimated errors in the last digit in cases where these are available.) @ Copyright 2005 American Institute of Physics.

Method	$N$	25 K	14 K
MEAC <sup>a</sup>	108	1.47	0.28
QMCT <sup>b</sup>	108	1.69	0.30
FBSD <sup>c</sup>	108	1.68(5)	0.75(7)
CWM <sup>d</sup>	125	1.73	–
CMD <sup>e</sup>	180	1.52(8)	0.35(5)
RPMD <sup>f</sup>	$\infty$	1.59(1)	0.33(1)
Expt. <sup>g</sup>	–	–	0.4

<sup>a</sup> Maximum entropy analytic continuation (Ref. 20).

<sup>b</sup> Quantum mode-coupling theory (Ref. 21).

<sup>c</sup> Forward-backward semiclassical dynamics (Ref. 22).

<sup>d</sup> Classical Wigner model (Ref. 23).

<sup>e</sup> Centroid molecular dynamics (Ref. 24).

<sup>f</sup> Ring-polymer molecular dynamics (Ref. 19).

<sup>g</sup> Experimental results from (Ref. 25).

## 2.6 References

- [1] R. P. Feynman, A. R. Hibbs, *Quantum Mechanics and Path Integrals*, McGraw-Hill: New York, 1965, Sections 12.8 and 12.9
- [2] R. P. Feynman, *Statistical Mechanics*, Benjamin, New York, (1972). Another classic text by Feynman which covers the basic concepts.
- [3] D. Chandler, P. G. Wolynes, "Exploiting the isomorphism between quantum theory and classical statistical mechanics of polyatomic fluids" *J. Chem. Phys.* **74** (1981) 4078-4095.
- [4] J. Cao, G. A. Voth, "A new perspective on quantum time correlation functions" *J. Chem. Phys.* **99** (1993) 10070-10073.
- [5] T. D. Hone, P. J. Rossky, G. A. Voth, "A comparative study of imaginary time path integral based methods for quantum dynamics" *J. Chem. Phys.* **124** (2006) 154103.
- [6] A. Pérez, M. E. Tuckerman, M. H. Müser, "A comparative study of the centroid and ring-polymer molecular dynamics methods for approximating quantum time correlation functions from path integrals" *J. Chem. Phys.* **130** (2009) 184105.
- [7] J. Cao, G. A. Voth, "The formulation of quantum statistical mechanics based on the Feynman path centroid density. II. Dynamical properties" *J. Chem. Phys.* **100** (1994) 5106-5117.
- [8] J. Cao, G. A. Voth, "The formulation of quantum statistical mechanics based on the Feynman path centroid density. III. Phase space formalism and analysis of centroid molecular dynamics" *J. Chem. Phys.* **101** (1994) 6157-6167.
- [9] J. Cao, G. A. Voth, "The formulation of quantum statistical mechanics based on the Feynman path centroid density. IV. Algorithms for centroid molecular dynamics" *J. Chem. Phys.* **101** (1994) 6168-6183.
- [10] J. Cao, G. A. Voth, "The formulation of quantum statistical mechanics based on the Feynman path centroid density. V. Quantum instantaneous normal mode theory for liquids" *J. Chem. Phys.* **101** (1994) 6184-6192.
- [11] S. Jang, G. A. Voth, "Path integral centroid variables and the formulation of their exact real time dynamics" *J. Chem. Phys.* **111** (1999) 2357-2370.

- [12] S. Jang, G. A. Voth, “A derivation of centroid molecular dynamics and other approximate time evolution methods for path integral centroid variables” *J. Chem. Phys.* **111** (1999) 2371-2384.
- [13] I. R. Craig, D. E. Manolopoulos, “Quantum statistics and classical mechanics: Real time correlation functions from ring polymer molecular dynamics” *J. Chem. Phys.* **121** (2004) 3368-3373.
- [14] I. R. Craig, D. E. Manolopoulos, “Chemical reaction rates from ring polymer molecular dynamics” *J. Chem. Phys.* **122** (2005) 084106.
- [15] I. R. Craig, D. E. Manolopoulos, “A refined ring polymer molecular dynamics theory of chemical reaction rates” *J. Chem. Phys.* **123** (2005) 034102.
- [16] B. J. Braams, D. E. Manolopoulos, “On the short-time limit of ring polymer molecular dynamics” *J. Chem. Phys.* **125** (2006) 124105.
- [17] J. A. Morrone, “The proton momentum distribution in hydrogen bonded systems: A path integral molecular dynamics study” [http://webusers.fis.uniroma3.it/sns\\_fpr/lecture/Lecture\\_10/morrone\\_9-10.pdf](http://webusers.fis.uniroma3.it/sns_fpr/lecture/Lecture_10/morrone_9-10.pdf).
- [18] Harry A. Stern, B. J. Berne, “Quantum effects in liquid water: Path-integral simulations of a flexible and polarizable ab initio model” *J. Chem. Phys.* **115** (2001) 7622-7626.
- [19] T. F. Miller III, D. E. Manolopoulos, “Quantum diffusion in liquid para-hydrogen from ring-polymer molecular dynamics” *J. Chem. Phys.* **122** (2005) 184503.
- [20] E. Rabani, D. R. Reichman, G. Krilov, B. J. Berne, “The calculation of transport properties in quantum liquids using the maximum entropy numerical analytic continuation method: Application to liquid *para*-hydrogen” *PNAS.* **99** (2002) 1129-1133.
- [21] D. R. Reichman, E. Rabani, “A self-consistent mode-coupling theory for dynamical correlations in quantum liquids: Application to liquid *para*-hydrogen” *J. Chem. Phys.* **116** (2002) 6279-6285.
- [22] A. Nakayama, N. Makri, “Forward-backward semiclassical dynamics for quantum fluids using pair propagators: Application to liquid *para*-hydrogen” *J. Chem. Phys.* **119** (2003) 8592-8605.

- [23] J. A. Poulsen, G. Nyman, P. J. Rossky, “Quantum Diffusion in Liquid Para–hydrogen: An Application of the Feynman–Kleinert Linearized Path Integral Approximation” *J. Phys. Chem. B* **108** (2004) 19799-19808.
- [24] T. D. Hone, G. A. Voth, “A centroid molecular dynamics study of liquid para–hydrogen and ortho–deuterium” *J. Chem. Phys.* **121** (2004) 6412-6422.
- [25] B. N. Esel’son, Y. P. Blagoi, V. V. Grigor’ev, V. G. Manzhelii, S. A. Mikhailenko, and N. P. Neklyudov, “Properties of Liquid and Solid Hydrogen” *Israel Program for Scientific Translations*, Jerusalem, 1971.

## Chapter 3

# Double Proton Transfer Mechanism in Porphycene

In this chapter, full-dimensional path-integral molecular dynamics (PIMD) simulations have been performed for understanding the double proton transfer tautomerization mechanism of the inner two protons in porphycene and its isotopic-substituted molecules. In order to reduce computational costs, the semi-empirical PM6 level combined with specific reaction parameterization have been employed. The obtained results show that double proton transfer of the unsubstituted porphycene at  $T = 300$  K mainly occurs via a so-called concerted mechanism through the  $D_{2h}$  second-order saddle point. In addition, we found that both isotopic substitution and temperature significantly affect the double proton transfer mechanism. For example, the contribution of the stepwise mechanism increases with a temperature increase. We have also carried out hypothetical simulations with the porphycene configurations being completely planar. It has been found that out-of-plane vibrational motions significantly decrease the contribution of the stepwise proton transfer mechanism.

### 3.1 Multiple proton transfer

Multiple proton transfer is one of the fundamental chemical reactions and plays a very important role in many physical, chemical and biological processes [1,2]. For cases composing more than one proton, a basic question to be solved is whether the transfer occurs in a concerted or stepwise manner. In the concerted mechanism, multiple protons (or hydrogen atoms) simultaneously move. On the other hand, in the stepwise mechanism single proton transfers consecutively occur with each transfer process being an independent event. There have been many discussions of the mechanism of double

proton transfer processes, which is the simplest of the multiple proton transfer. For example, the question has been frequently addressed by using static electronic structure calculations of the potential energy surface of the system. However, the preferred mechanism cannot be determined from the barrier height which the dynamics of nuclei are not considered. Moreover, it should be mentioned that the potential energy surface of the double proton transfer reaction often contains second-order saddle points. In this case, it is sometimes difficult to locate such stationary points using standard quantum chemistry calculations.

### **3.2 Intramolecular double proton transfer in porphycene.**

Porphycene, which is a constitutional isomer of porphyrin, is a suitable molecule for studying the detailed mechanism of intra-molecular double proton transfer processes. This molecule has four pyrrole rings that form four proton-bound sites inside an inner cavity. The tautomerization of porphycene is summarized in Fig. 3-1, which is showing the proton transfer pathways among the lowest four stationary points on the ground-state potential energy surface. The  $C_{2h}$  *trans* structure is the most stable tautomer and that the energy of the  $C_{2v}$  *cis* structure is slightly higher than that of the *trans* structure. Thus, the  $C_{2v}$  *cis* configuration is the intermediate on the potential energy surface. The  $D_{2h}$  SS structure is a second-order saddle point (or hilltop) and is the most probable transition state along the concerted double proton transfer pathway between the two *trans* structures. The  $C_s$  TS structure is the transition state (first-order saddle point) of the stepwise single proton transfer process between the *trans* and *cis* configurations.

The experimental studies have already been reported for proton transfer in porphycene after the first synthesis of porphycene by Vogel and co-workers [3-11]. For example, Limbach and co-workers have studied the tautomerization for porphycene and its isotope-substituted molecules using a combination of NMR spectroscopy and relaxometry in that temperature range of 50 ~ 403 K in solid state [4,5]. The motion of the inner two protons is too rapid to be frozen in the NMR time scale. Electronic absorption and fluorescence spectra have been measured by Sepioł and co-workers for

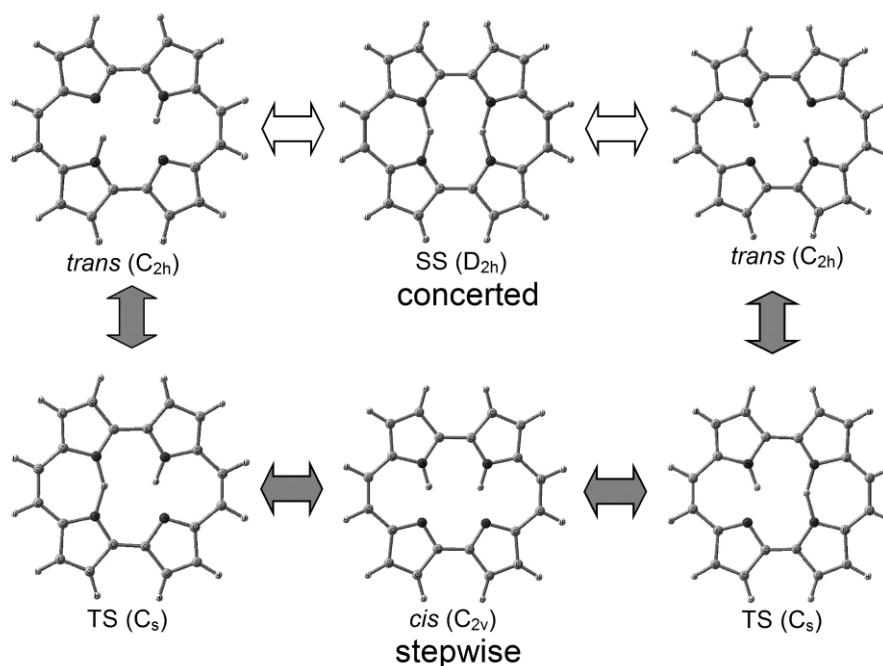


Fig. 3-1. Concerted ( $C_{2h}$  *trans*  $\leftrightarrow$   $D_{2h}$  SS  $\leftrightarrow$   $C_{2h}$  *trans*) and stepwise ( $C_{2h}$  *trans*  $\leftrightarrow$   $C_s$  TS  $\leftrightarrow$   $C_{2v}$  *cis*) double proton transfer pathways for the tautomerization in porphycene.

porphycene isolated in low-temperature supersonic molecular beams [6,7]. Vdovin and co-workers have performed the spectroscopic experiments in superfluid helium nanodroplets [8]. They revealed quantum delocalization of inner two protons by observing the tunneling splitting  $4.4\text{ cm}^{-1}$  in molecular vibrational spectra. They also found that there are vibrational modes that enhance and suppress the concerted proton transfer tunneling probability.

On the other hand, there have been also theoretical works for the tautomerization in porphycene [12–22]. Kozłowski and co-workers have carried out systematic calculations for the inner-proton transfer of porphycene at the B3LYP and MP2 levels of theory [15]. They have theoretically shown that the  $C_{2v}$  *cis* intermediate structure is 2.4 kcal/mol higher in energy than the most stable  $C_{2h}$  *trans* structure at the B3LYP/TZ2P level without zero-point harmonic vibrational energy correction. Also, the barrier heights for the concerted and stepwise pathways were reported to be 7.6 and 4.9 kcal/mol at the B3LYP/TZ2P, respectively. This indicates that the stepwise mechanism is energetically favorable. However, it should be emphasized that zero-point

vibrational energy correction significantly changes this energetic behavior.

Kozłowski *et al.* have already pointed out that the barrier heights for the two pathways become comparable (~1.6 kcal/mol) after zero-point vibrational energy correction based on harmonic frequency analyses [15]. This result comes from the fact that the  $D_{2h}$  second-order saddle point has one more imaginary frequency than the  $C_s$  first-order transition state structure. This implies that nuclear quantum effects could play an important role in the selection of dominant pathway of the proton transfer process as well as the reaction rate. In order to understand the nuclear quantum effects for the double proton transfer, full-dimensional PIMD simulations have been performed employing semiempirical PM6 potential function improved by specific reaction parameters method (SRP) for porphycene and its isotope-substituted molecules.

### 3.3 Methods

The most robust approach would be "on-the-fly" *ab initio* PIMD [23-26], where *ab initio* electronic structure theory calculations are directly employed to obtain potential energy values and their derivatives during the course of the PIMD propagation. However, it is still very expensive to use *ab initio* (or DFT) PIMD methods for the present porphycene system.

Computational costs of many integral calculations, especially two electron integrals, in *ab initio* molecular orbital method are high. In order to reduce the costs, the integrals in the semiempirical molecular orbital methods are approximated by functions with empirical parameters while Hartree-Fock equation is solved as well as *ab initio* calculation. These parameters can be adjusted to improve the agreement with experiment.

#### 3.3.1 Semiempirical PM6 method

The PM6 is a recently-developed semiempirical method by Stewart [27,28]. That can predict geometries and heat of formation consistent with DFT results and experimental observations. However, accurate evaluation of the dispersion energy and hydrogen bonding by this method is still difficult.

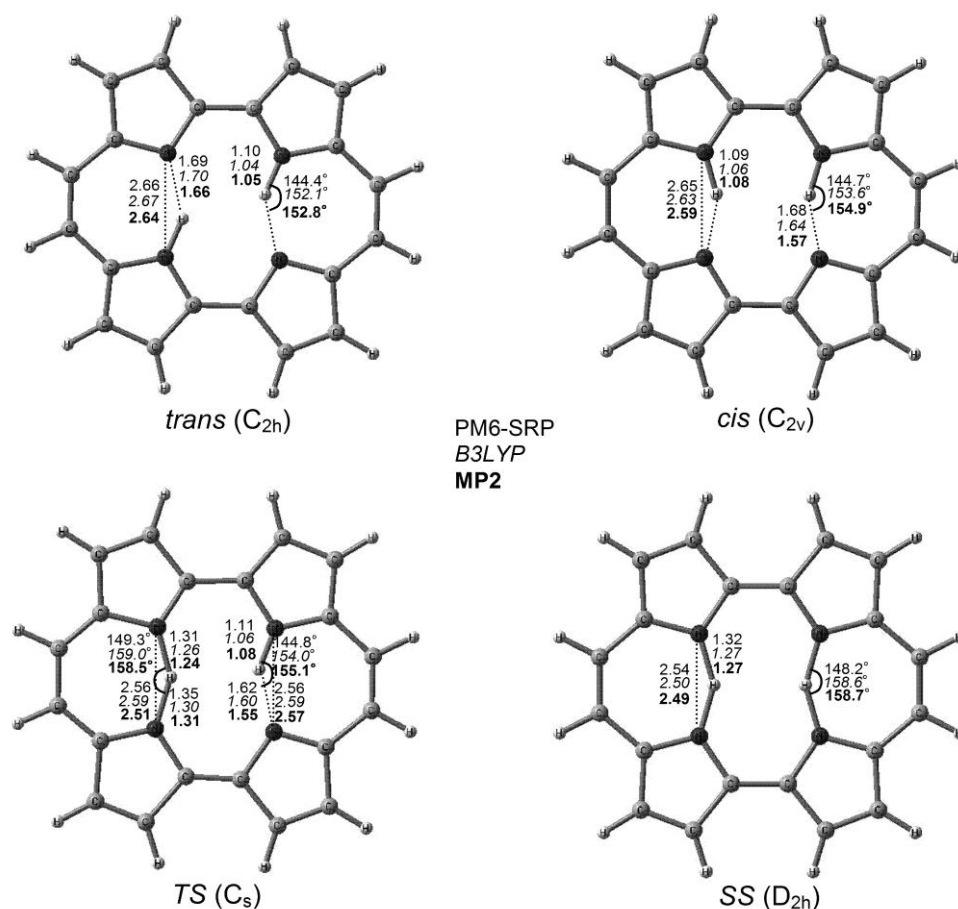


Fig. 3-2. Comparison of the optimized PM6-SRP stationary point geometries on the potential energy surface for porphycene to the B3LYP/TZ2P (*italic*) and MP2/6-31+G(d, p) (**bold**) results [15,20,21,29]. Selected bond lengths (in Å) and bond angles (in degrees) are shown.

### 3.3.2 Application of specific reaction parameter method to the PM6

The specific-reaction-parameter (SRP) method approach selected parameters of a semiempirical method are adjusted to fit *ab initio* (or DFT) results for a specific reaction (or a small range of reactions) [30-32]. First, trial semiempirical parameters have been randomly generated within appropriate ranges and then geometry optimization of the four stationary points performed. More specifically, in the case of the parameters used in molecular integrals, we generated a trial value in the range of  $(-1 + \alpha)$  eV and  $(1 + \alpha)$  eV, where  $\alpha$  is the original PM6 parameter. In the case of the three

parameters for the gaussian function used in the core-core repulsion energy [27], we have generated trial values within  $\pm 150$  %. A total of 200 sets of parameters were randomly generated and then obtained energies were compared to that obtained from various electronic structure calculations. Here, obtained SRP parameters are summarized in Table 3-1. Notice that parameters of nitrogen atom is not fitted. Fig. 3-2 compares some PM6-SRP geometric parameters to those obtained at the B3LYP/TZ2P and MP2/6-31G(d, p) levels. The PM6-SRP results are good agreement with The MP2 and B3LYP [15,19-21].

Atom	Parameter	PM6	PM6-SRP	$\Delta$
H	$U_{ss}$ (eV)	-11.247	-10.8118	0.4352
	$\beta_s$ (eV)	-8.353	-8.018	0.335
	$G_{ss}$ (eV)	14.4487	14.7724	0.3237
	$a_1$ (none)	0.0242	0.0357	0.0115
	$b_1$ ( $\text{\AA}^{-2}$ )	3.056	5.2628	2.2068
	$c_1$ ( $\text{\AA}$ )	1.786	1.9837	0.1977
C	$U_{ss}$ (eV)	-51.0897	-51.0995	-0.0098
	$U_{pp}$ (eV)	-39.9379	-39.9334	0.0045
	$\beta_s$ (eV)	-15.3852	-15.7835	-0.3983
	$\beta_p$ (eV)	-7.4719	-7.5395	-0.0676
	$G_{ss}$ (eV)	13.3355	13.5478	0.2123
	$G_{pp}$ (eV)	10.7783	10.0116	-0.7667
	$G_{sp}$ (eV)	11.5281	11.9605	0.4324
	$G_{p2}$ (eV)	9.4862	9.6319	0.1457
	$H_{sp}$ (eV)	0.7173	0.3891	-0.3282

TABLE 3-1. Original PM6 parameters and specific reaction parameters determined in this work for porphycene.

Level	<i>trans</i> (C <sub>2h</sub> )	<i>cis</i> (C <sub>2v</sub> )	TS (C <sub>s</sub> )	SS (D <sub>2h</sub> )
B3LYP/6-31G( <i>d</i> ) <sup>a</sup>	0.0 (0.0)	2.6 (2.1)	5.4 (2.1)	8.2 (2.2)
B3LYP/6-31G( <i>d, p</i> ) <sup>b,e</sup>	0.0 (0.0)	2.23 (1.59)	4.10 (1.01)	6.13 (0.55)
B3LYP/6-31+G( <i>d, p</i> ) <sup>c</sup>	0.0 (0.0)	2.30 (0.59)	4.68 (5.54)	6.45 (3.03)
B3LYP/TZ2P <sup>a</sup>	0.0 (0.0)	2.4 (1.9)	4.9 (1.6)	7.6 (1.6)
PZB/PW <sup>d</sup>	0.0	2.5	4.9	7.5
BLYP/PW <sup>d</sup>	0.0	2.1	3.9	5.9
PBE/PW <sup>d</sup>	0.0	1.5	2.4	3.5
BP/PW <sup>d</sup>	0.0	1.6	2.5	3.6
MP2/6-31G( <i>d</i> ) <sup>a</sup>	0.0 (0.0)	5.1 (4.6)	5.7 (2.4)	7.6 (1.6)
MP2/6-31+G( <i>d, p</i> ) <sup>c,e</sup>	0.0	2.65	3.75	5.23
MPW1K/6-31+G( <i>d, p</i> ) <sup>c</sup>	0.0	1.68	2.42	3.41
SCC-DFTB <sup>b</sup>	0.0	3.7	11.1	–
PM3 <sup>e</sup>	0.0 (0.0)	6.1 (6.1)	18.5 (14.4)	29.8 (22.1)
PM6 <sup>e</sup>	0.0 (0.0)	5.7 (5.8)	10.9 (8.0)	12.4 (7.5)
PM6-SRP <sup>e</sup>	0.0 (0.0)	1.1 (3.7)	4.4 (4.8)	5.5 (1.8)

<sup>a</sup>Ref. 15

<sup>b</sup>Ref. 19

<sup>c</sup>Ref. 20

<sup>d</sup>Ref. 21

<sup>e</sup>This work

TABLE 3-2. Comparison of relative energies (in kcal/mol) between stationary points on the porphycene potential energy surface obtained with various electronic structure levels of theory. Numbers in parentheses are relative energies including zero-point vibrational energy correction obtained from harmonic vibrational frequency analyses. The relative energy of *trans*-porphycene (C<sub>2h</sub>) is taken to be zero.

### 3.3.3 Simulation conditions

The PIMD simulations were carried out with  $P = 24$ -64 beads depending on the system temperature as well as isotopic substitution. The massive N ose-Hoover chain thermostat technique was implemented in the velocity Verlet algorithm (see also Appendix A) to the control system temperature [24-26,33]. The time increment was set to  $\Delta t = 5$ –10 atomic unit (0.12–0.24 fs). These numerical parameters were carefully chosen to obtain fully converged results. It was found that the double proton transfer processes in porphycene dominantly occur via the concerted mechanism at  $T = 300$  K. Based on the comparison between classical MD and PIMD calculations, it has also been concluded that the concerted pathway is emphasized by nuclear quantum effects. In this paper, we discuss the effect of isotopic substitution of the inner protons on the double proton transfer mechanism in porphycene. The semiempirical calculations were performed using the MOPAC2009 code, which has been interfaced to our PIMD simulation code [34].

### 3.4 Potential energy surface of double proton transfer for porphycene

First, we mention the features of the PM6-SRP potential energy surface of porphycene. Fig. 3-3 displays the two-dimensional contour map plotted as a function of  $r_1$ – $r_2$  and  $r_3$ – $r_4$  distance differences, where  $r_i$  represents the N-H distance defined in the same figure. Notice that the  $r_1$ – $r_2$  and  $r_3$ – $r_4$  distances are able to characterize both concerted and stepwise pathways of the proton transfer reaction. All other internal coordinates were optimized with respect to total energy. Four potential minima are seen in Fig. 3-3 corresponding to the  $C_{2h}$  *trans* and  $C_{2v}$  *cis* structures; the two minima at  $(-0.59, -0.59)$  and  $(0.59, 0.59)$  correspond to the most stable  $C_{2h}$  *trans* structures, while the two minima at  $(-0.59, 0.59)$  and  $(0.59, -0.59)$  to the intermediate  $C_{2v}$  *cis* structures. Note that the relative energy is measured from the energy level of the  $C_{2h}$  *trans* minimum. The PM6-SRP potential gives the relative energy between the  $C_{2h}$  *trans* and  $C_{2v}$  *cis* structures to be 1.1 kcal/mol (see also Table 3-2). This value is somewhat smaller than the previously reported values obtained at the DFT-B3LYP and *ab initio* MP2 levels

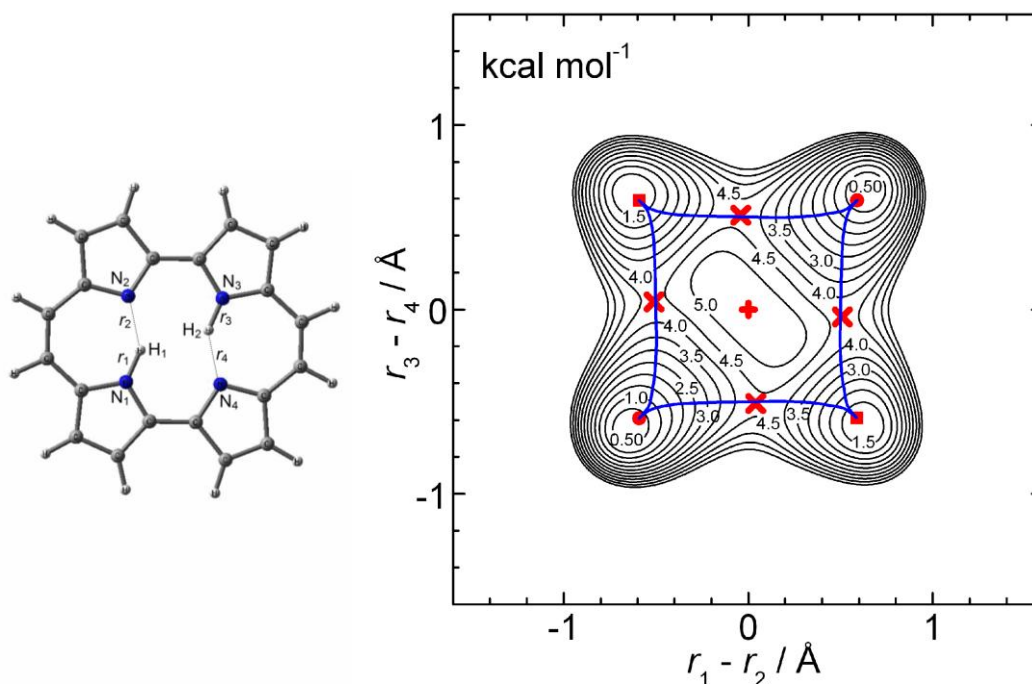


Fig. 3-3. Two-dimensional potential energy surface as a function of  $r_1-r_2$  and  $r_3-r_4$  coordinates obtained at the PM6-SRP semiempirical level, where  $r_i$  is the distance between the inner proton and nitrogen atom. Contour increments are 0.5 kcal/mol. Circles and squares indicate  $C_{2h}$  *trans* and  $C_{2v}$  *cis* minima, respectively. The saddle points for the stepwise process and the second-order saddle point for the concerted process are also shown as crosses. The intrinsic reaction coordinates for the stepwise process are also shown.

(2.2–2.7 kcal/mol) [15,19-21,29] but is close to the value obtained at the DFT-PBE level (1.5 kcal/mol) [21]. The barrier height for the first-order stepwise pathway (*trans*–*cis* inter-conversion) was obtained to be 4.4 kcal/mol at the PM6-SRP method, which is also in the range of previously reported results (2.4–5.7 kcal/mol) [15,19-21]. Notice that the corresponding transition states are seen at  $(-0.51, 0.04)$ ,  $(0.51, -0.04)$ ,  $(-0.04, 0.51)$  and  $(0.04, -0.51)$  in Fig. 2. The coordinate origin at  $r_1-r_2 = r_3-r_4 = 0$  corresponds to the  $D_{2h}$  second-order saddle point configuration of porphycene. The barrier height for the concerted pathway via the  $D_{2h}$  second-order saddle point is

obtained to be 5.5 kcal/mol, which is thus slightly larger than the stepwise barrier height. Again, the obtained value is in the range of the previously reported results (3.4–8.2 kcal/mol) at various electronic structure levels [15,19-21]. In summary, it is found that these PM6-SRP results are either within or close to the error bars of previous electronic structure calculations. Of course, for a more reliable assessment, one should wait for *ab initio* calculations with higher accuracy to truly determine the barrier heights, such as CCSD(T) or MRCI level of theory with large basis sets. Such a calculation is not currently available, unfortunately, within our computer facility.

### 3.5 Proton density distribution for HH-porphycene

Fig. 3-4 displays a representative three-dimensional perspective plot of the nuclear distribution function obtained from the PIMD simulation for the unsubstituted porphycene (HH-porphycene). In this plot, Cartesian coordinates are transformed so as that overall translational and rotational motions are removed. Large fluctuation motion can be seen for all hydrogen atoms due to the large zero-point vibrational amplitude of light atoms. However, qualitative trend in their motions is clearly different between the outer and inner hydrogen (H) atoms. We can see that out-of-plane motions are significant for the outer 12 hydrogen atoms, while the inner two hydrogen atoms are mainly vibrating within the molecular plane due to hydrogen-bonding although small out-of-plane amplitudes are also seen.

### 3.6 PIMD vs classical MD for two-dimensional proton density distribution in HH-porphycene

Fig. 3-5 shows the two-dimensional contour plots of the inner proton distributions as a function of the  $r_1 - r_2$  and  $r_3 - r_4$  coordinates obtained from the PIMD simulations at  $T = 300$  and  $500$  K. Notice that the coordinate origin ( $r_1 - r_2 = r_3 - r_4 = 0$ ) corresponds to the  $D_{2h}$  second-order saddle point structure of HH-porphycene (see Figs. 3-1 and 3-2). From the density distribution plots presented in Fig. 3-5a, it is seen that double proton transfer between *trans-trans* structures in HH-porphycene at  $T = 300$  K occurs mainly through the concerted mechanism due to the higher distribution around the coordinate

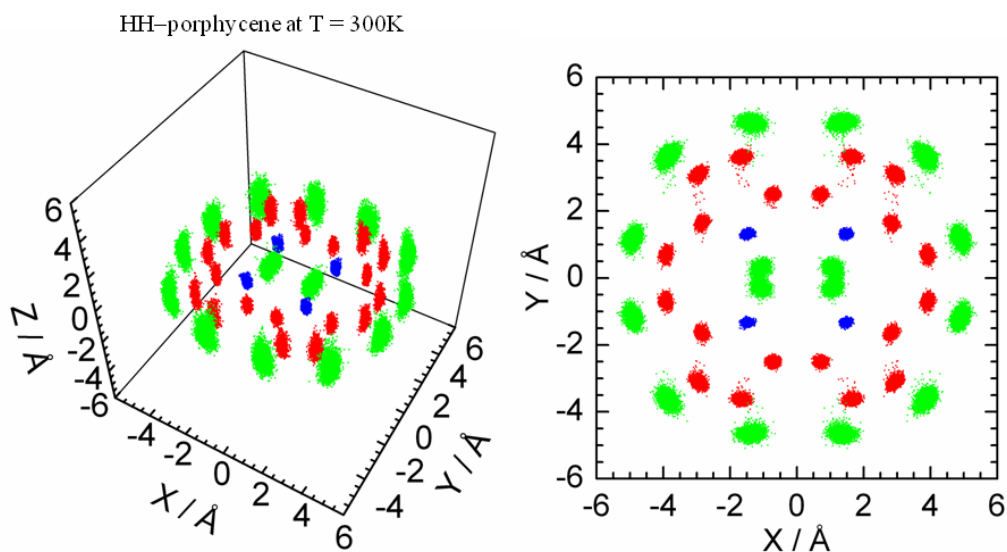


Fig. 3-4. Three-dimensional perspective plots of the PIMD nuclear distributions of the HH-porphycene at  $T = 300$  K. Right panels show the distributions projected on the X–Y plane.

origin,  $(r_1 - r_2, r_3 - r_4) = (0, 0)$ . At  $T = 300$  K the population of the *cis* form is seen to be very small. Thus, the contribution of the stepwise mechanism is less important. On the other hand, one can notice that the population of the *cis* form clearly increases at  $T = 500$  K. Therefore, we can see that the double proton transfer reaction also occurs via the stepwise mechanism from the density plot present in Fig. 3-5b although the dominant mechanism is the concerted one.

It should be emphasized that the trend seen in Fig. 3-5 can qualitatively be predicted from the zero-point corrected barrier heights; however, the present PIMD result definitely indicates the importance of the vibrational quantization for understanding the double proton transfer mechanism in HH-porphycene. In order to understand the importance of the nuclear quantum effect, we have also performed standard constant temperature classical molecular dynamics simulations on the same PM6-SRP potential energy surface. The classical result is presented in Fig. 3-5c. Notice that the classical distribution function is completely different from the quantum distributions. In the

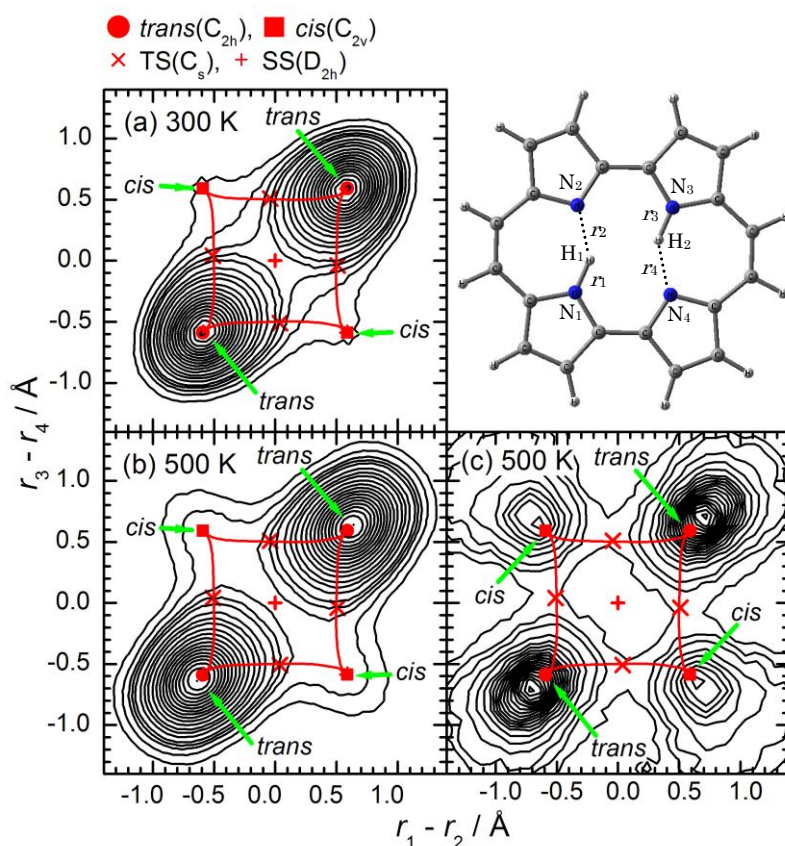


Fig. 3-5. Two-dimensional contour plots of the inner proton distributions in porphycene as a function of  $r_1 - r_2$  and  $r_3 - r_4$  obtained from the PIMD simulations at  $T = 300$  K (a) and  $T = 500$  K (b). The same plot but obtained from the classical MD simulation at  $T = 500$  K is shown in (c). Circles and squares indicate  $C_{2h}$  *trans* or  $C_{2v}$  *cis* minima on the PM6-SRP potential energy surface, respectively. The saddle points for the stepwise process and the second-order saddle point for the concerted process are also shown as crosses. The intrinsic reaction coordinates (IRCs) for the stepwise pathways are also shown.

classical case, we have found that the double proton transfer process always occurs via the  $C_s$  first order saddle point structure, *i.e.*, via the stepwise mechanism. Therefore, we conclude that the dominant concerted double proton transfer mechanism is a result of nuclear quantum effects

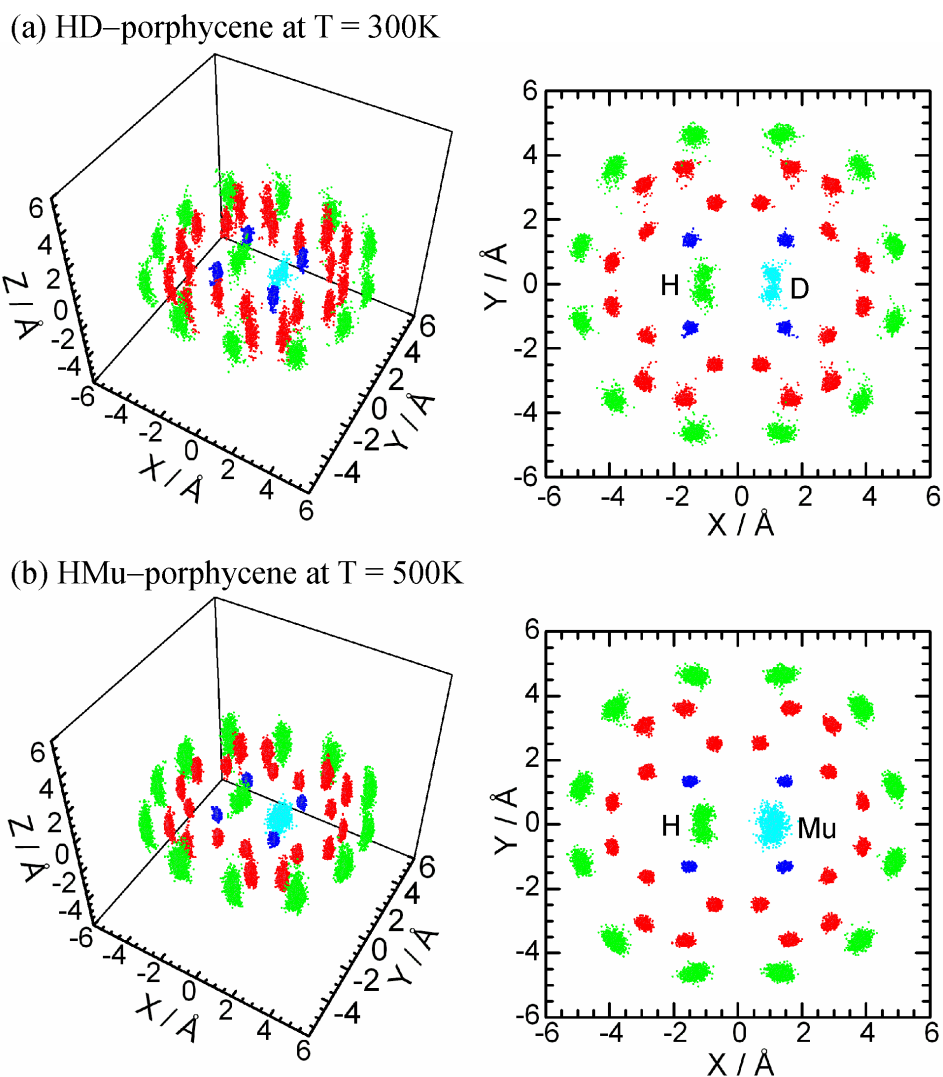


Fig. 3-6. Three-dimensional perspective plots of the PIMD nuclear distributions of the isotopic-substituted porphycene molecules: (a) HD-porphycene at  $T = 300\text{ K}$  and (b) HMu-porphycene at  $T = 500\text{ K}$ . In both cases, one of the two inner protons of porphycene is isotopic-substituted into deuteron or muon. Right panels show the distributions projected on the X–Y plane.

### 3.7 Proton density distribution for isotopic-substituted porphycenes

Figs. 3-6a and 3-6b display isotopic-substituted porphycene molecules, where one of the inner protons were replaced into deuteron (HD-porphycene) or muon (HMu-porphycene), whose mass is about 1/9 of the proton mass. Large fluctuation

motion can be seen for both the inner proton and deuteron in Fig. 3-6a, but the fluctuation for the inner proton is somewhat broader than that for the inner deuteron. The corresponding PIMD simulation was performed with 64 beads at  $T = 500$  K due to its very light mass of muon. Fig. 3-6b shows the nuclear distributions of the substituted porphycene, where one of the inner protons was replaced into muon. It is interesting to note that, although the muon distribution is significantly broader than the proton distribution, and its density maximum is located around the midpoint of the two nitrogen atoms. This is an expected result since the zero-point energy of the corresponding muon vibration is very large. In this case, even when the potential energy surface has a double-minimum character, the particle is mainly located around the saddle point region. In fact, as is shown in Table 3-3, the zero-point corrected energy level of the  $D_{2d}$  structure is lower than that of the  $C_{2h}$  *trans* structure for the HMu-porphycene molecule.

Relative energy / kcal mol <sup>-1</sup>	<i>trans</i> ( $C_{2h}$ )	<i>cis</i> ( $C_{2v}$ )	TS ( $C_s$ )	SS ( $D_{2h}$ )
PES <sup>a</sup>	0.0	1.1	4.4	5.5
HH <sup>b</sup>	0.0	3.7	4.8	1.8
DD <sup>b</sup>	0.0	3.7	5.6	3.1
HD <sup>b</sup>	0.0	3.8	5.0	2.7
HMu <sup>b</sup>	0.0	3.8	4.6	-2.5

<sup>a</sup> Relative energies without zero-point vibrational energy correction.

<sup>b</sup> Relative energies with zero-point vibrational energy correction for isotopic-substituted porphycenes.

TABLE 3-3. Relative energies of the stationary point configurations of porphycene with and without zero-point vibrational energy correction obtained on the PM6-SRP potential energy surface. The energies are measured from the energy of the most stable  $C_{2h}$  *trans* structure.

### 3.8 Two-dimensional proton density distributions for isotopic substituted porphycenes

In order to understand the effect of isotopic substitution as well as temperature on the double proton transfer mechanism in porphycene more clearly, we show two-dimensional contour plots of the inner proton/deuteron distributions as a function of the  $r_1-r_2$  and  $r_3-r_4$  coordinates in Fig. 3-7. At  $T = 300$  K, in the case that both the two protons are replaced by deuterons (DD-porphycene), the obtained distributions are similar to the unsubstituted HH-porphycene case although the density around the *cis* configuration is larger than that for the HH case. This suggests that the contribution of the stepwise mechanism becomes more important for the DD-porphycene molecule. Notice that the obtained distribution becomes asymmetric with respect to the  $r_1 - r_2 = r_3 - r_4$  line when one proton is replaced by a deuteron (HD-porphycene) or muon (HMu-porphycene). It is interesting note that, in the HD-porphycene case at  $T = 300$  K, the contribution of the concerted and stepwise mechanisms is seen to be comparable to the DD-porphycene case. Although the present PIMD simulations give only thermal statistical nuclear distributions, the asymmetric position of H and D must be relevant to the asynchronous motions of H and D transfer, and thus it should affect the trajectories of the reaction. Similar to the HH-porphycene case, it can be seen that the system temperature somewhat affects the density distributions, and hence the proton transfer mechanism.

### 3.9 Free energy surface for the double proton transfer

In order to characterize the rate of chemical reactions, it is sometimes useful to compute a free energy surface  $F(\mathbf{q})$  along an appropriate reaction coordinate  $\mathbf{q}$  [33,34]. The free energy  $F(\mathbf{q})$  is rigorously defined as  $F(\mathbf{q}) = -k_B T \ln \rho(\mathbf{q})$ , where  $\rho(\mathbf{q})$  is the probability to observe a given value of  $\mathbf{q}$  while sampling molecular configurations in the PIMD simulation.

Fig. 3-9 shows the free energy surfaces associated with  $r_1-r_2$  and  $r_3-r_4$  coordinates. First, it should be emphasized that the features of all the free energy surfaces obtained are very different from those of the bare potential energy surface (see Fig. 3-3). In the

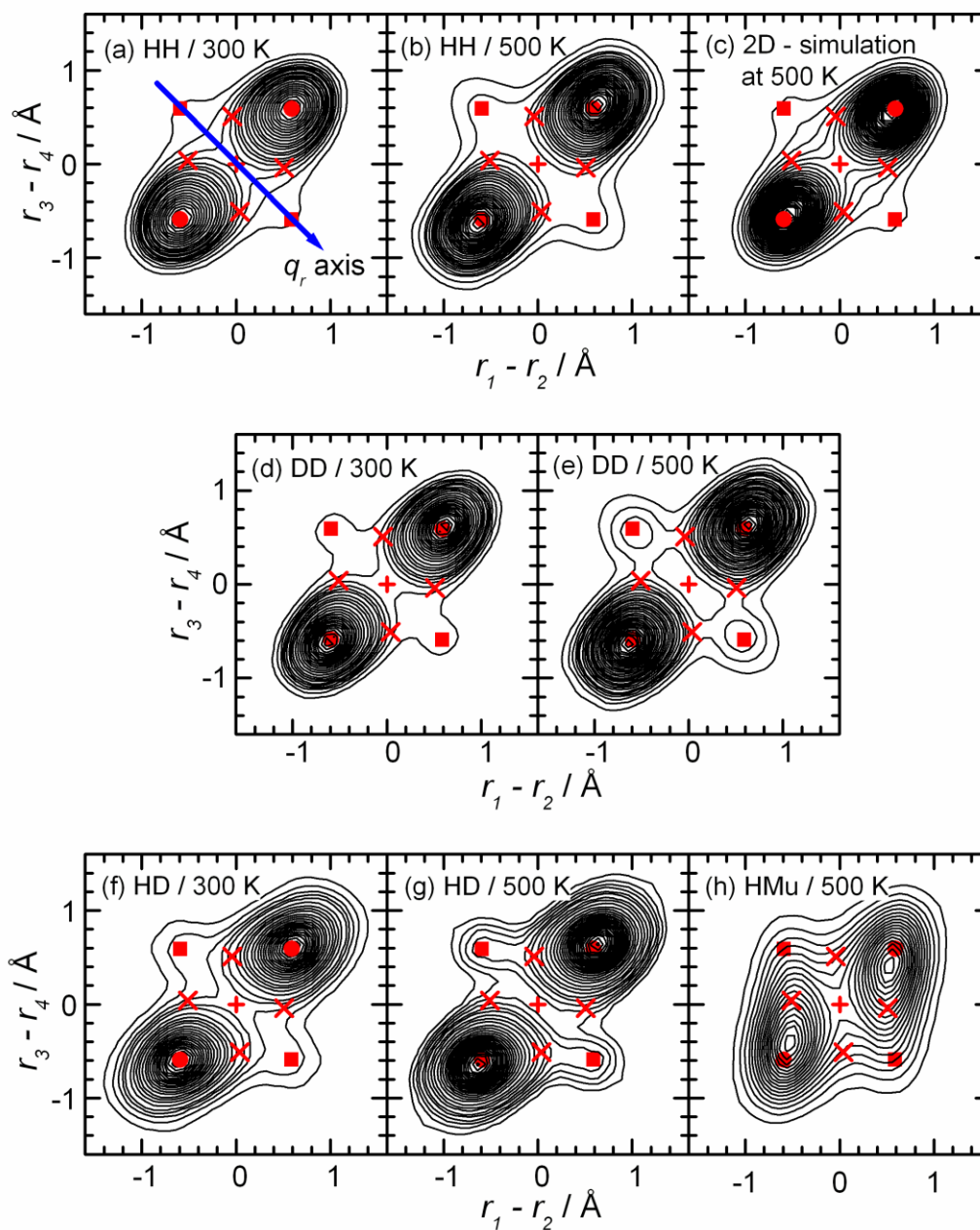


Fig. 3-7. Two-dimensional contour plots of the inner proton/deuteron distributions for prophyene and its isotopic variants as a function of  $r_1-r_2$  and  $r_3-r_4$  coordinates obtained from the PIMD simulations at  $T = 300$  and  $500$  K. Symbols (circles, squares, and crosses) indicate the stationary points on the PM6-SRP potential energy surface. The result obtained from the 2D-PIMD simulation for HH-prophyene at  $T = 500$  K with porphyene configurations being planar structures is also shown.

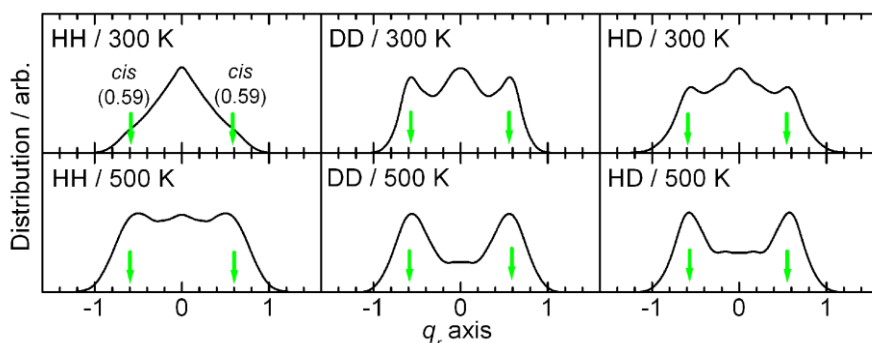


Fig. 3-8. Inner proton/deuteron distributions along the  $r_1-r_2 = r_4-r_3$  line (corresponding to the  $q_r$ -axis in Fig. 3-7) obtained from the PIMD simulations at  $T = 300$  and  $500$  K

case of HH-porphycene at  $T = 300$  K, one can see that the free energy barrier (1.5 kcal/mol at the  $D_{2h}$  second-order saddle point) for the concerted pathway is lower than that for the *cis* configuration (1.8 kcal/mol at the *cis* minima). The former value is comparable to the zero-point energy corrected barrier height (1.8 kcal/mol) for the concerted pathway (see Table 1). At  $T = 500$  K, the free energy barrier for the concerted pathway is estimated to be  $\sim 2.5$  kcal/mol for HH-porphycene. Thus, the free energy barrier is higher for the concerted pathway as the temperature is higher. One of the important origins for this temperature dependence in the barrier height may be large quantum fluctuation at lower temperatures, which is characterized by the radius of gyration of the ring polymer in the transition state [35]. However, further analysis must be done to study this issue in detail, which is beyond our scope here.

As an independent issue from the discussions above, another interesting one is on the role of broken planarity of the porphycene molecule at finite temperatures. In order to investigate this issue, we have also performed similar PIMD simulations with the porphycene configurations restricted to be always planar (hereafter, we call it "2D-PIMD"). Fig. 3-7c displays the nuclear distribution plotted as a function of the  $r_1-r_2$  and  $r_3-r_4$  coordinates obtained from the 2D-PIMD simulations at  $T = 500$  K. Compared with the "3D-simulations" at  $T = 500$  K presented in Fig. 3-7b, the concerted proton transfer mechanism is enhanced while the stepwise mechanism is somewhat suppressed in the 2D-simulation. This result qualitatively suggests that the out-of-plane

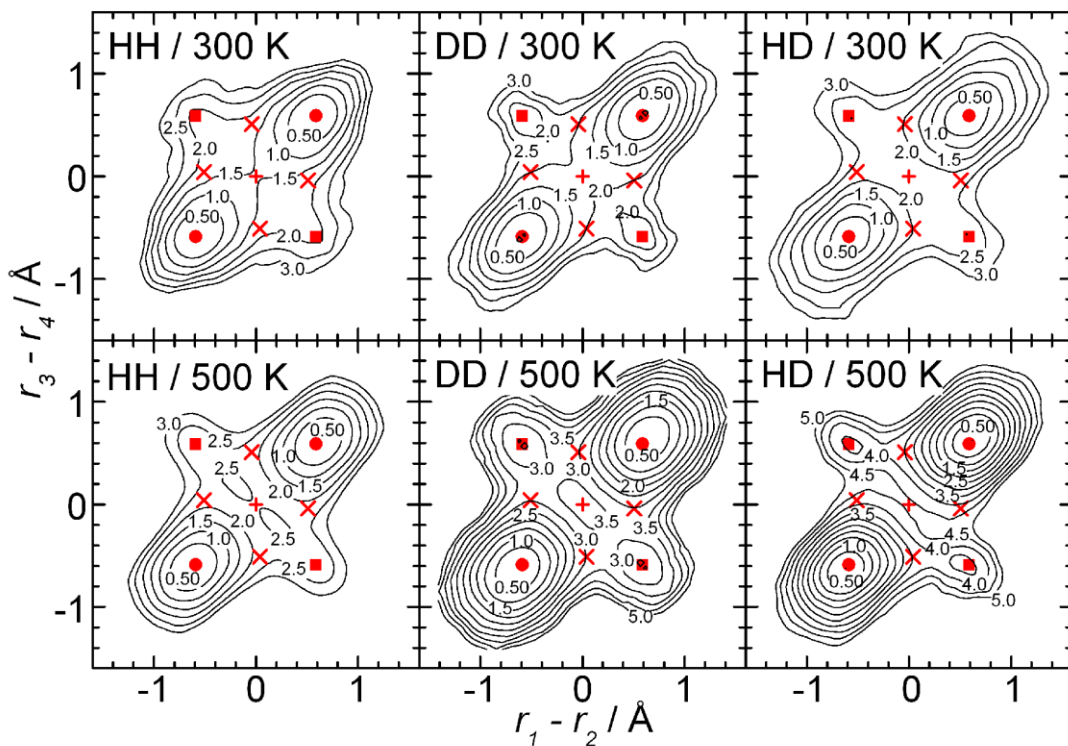


Fig. 3-9. Two-dimensional contour plots of free-energy surfaces as a function of  $r_1-r_2$  and  $r_3-r_4$  coordinates obtained from the PIMD simulations at  $T = 300$  and  $500$  K for HH-porphycene, DD-porphycene, and HD-porphycene

motions of porphycene have the influence of suppressing the concerted proton transfer mechanism. In this case, the out-of-plane motions could be considered as mainly entropic effects since the vibrational frequencies of the corresponding normal modes are in the range of  $50-200 \text{ cm}^{-1}$  which is smaller than thermal energy,  $kT$ . Recently, there has been an interesting experimental report by Vdovin *et al.* that for porphycene embedded in superfluid helium nanodroplets there are vibrational modes that enhance and suppress the concerted proton transfer tunneling probability [8]. However, as far as we are aware, there has been no such experimental information on the gas phase porphycene. We hope that the present computational study would stimulate future experiments along this line.

### 3.10 Correlation of the inner nitrogen motion with the proton transfer and its isotope effects

Fig. 3-10 displays the two-dimensional contour plots of the inner (a) proton and (b) deuterium distributions as a function of the  $N_1-N_2$  (or  $N_3-N_4$ ) distance and  $r_1-r_2$  (or  $r_3-r_4$ ). Since the  $r_1-r_2$  distance difference qualitatively corresponds to the reaction coordinate of proton transfer, these plots indicate that the proton transfer process strongly correlates with the  $N_1-N_2$  stretch motion. We can see that proton transfer effectively occurs when the  $N_1-N_2$  distance is small indicating that the N–N stretch vibration is a promoting mode of proton transfer, as expected. This behavior is frequently seen in the proton transfer process in water [33]. However, note that the N–N distance difference between the transition state and the equilibrium structures (0.12 Å) is not so large as the case of O–O distance of water. In addition, the proton distribution spreads in broader range of  $r(N_1-N_2)$  than the deuterium.

Fig. 3-11 shows the two-dimensional contour plots of the inner proton/deuteron distributions as a function of the  $r_1-r_2$  coordinate and angle  $\theta$  ( $\angle N-H(D)-N$ ) obtained from the PIMD simulations at  $T = 300$  K for the HH-porphycene and DD-porphycene molecules. It can be seen that the proton/deuteron transfer mainly occurs with bent configurations. From these plots, one can see that the proton transfer occurs with a somewhat a wider range of  $\theta$  than the deuteron transfer.

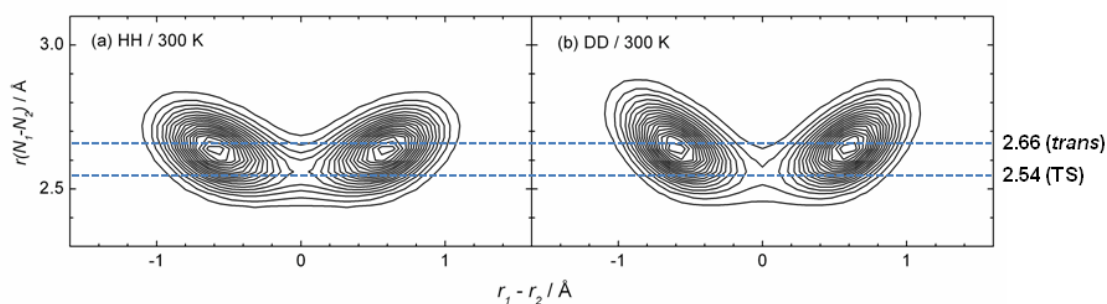


Fig. 3-10. Two-dimensional contour plots of the proton distribution as a function of the  $N_1-N_2$  distance and the difference between  $H_1-N_1$  and  $H_1-N_2$  (or  $H_2-N_3$  and  $H_2-N_4$ ) distances obtained from the PIMD simulations at  $T = 300$  K for (a) HH-porphycene and (b) DD-porphycene. Horizontal lines indicate the N–N distances at the trans equilibrium structure and the SS saddle point.

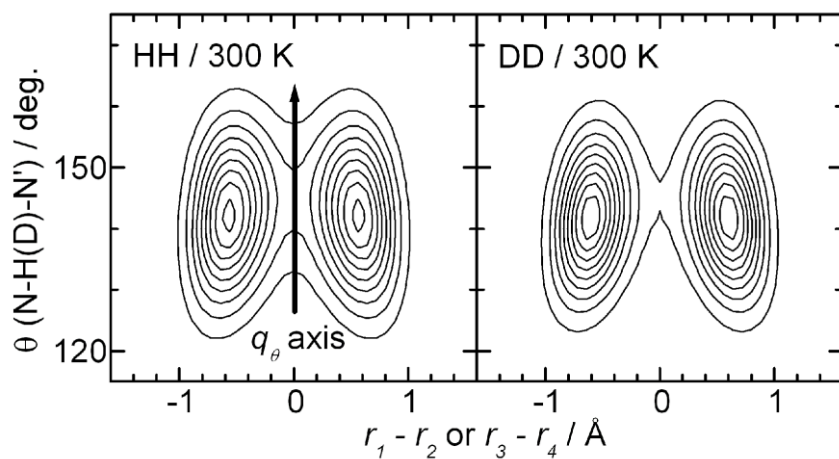


Fig. 3-11. Two-dimensional contour plots of proton/deuteron distributions for HH-porphycene and DD-porphycene as a function of  $r_1-r_2$  coordinate and angle  $\theta$  ( $\angle\text{N-H(D)-N}$ ) obtained from the PIMD simulations at  $T = 300$  K.

### 3.11 References

- [1] K. Giese, M. Petković, H. Naundorf, O. Kühn, “Multidimensional quantum dynamics and infrared spectroscopy of hydrogen bonds” *Phys. Rep.* **430** (2006) 211-276.
- [2] J. T. Hynes, J. P. Klinman, H. -H. Limbach, R. L. Schowen, “Single and Multiple Hydrogen/Deuterium Transfer Reactions in Liquids and Solids” *Hydrogen–Transfer Reactions*, Wiley-VCH, Weinheim, Germany, 2007.
- [3] E. Vogel, M. Kocher, H. Schmickler, J. Lex, *Angew. Chem. Int. Ed. Engl.* **25** (1986) 257-259.
- [4] B. Wehrle, H.-H. Limbach, M. Kocher, O. Ermer, E. Vogel, “<sup>15</sup>N-CPMAS-NMR Study of the Problem of NH Tautomerism in Crystalline Porphine and Porphycene” *Angew. Chem. Int. Ed. Engl.* **26** (1987) 934-936.
- [5] M. F. Shibl, M. Pietrzak, H. -H. Limbach, O. Kühn, “Geometric H/D Isotope Effects and Cooperativity of the Hydrogen Bonds in Porphycene” *Chem. Phys. Chem.* **8** (2007) 315-321.
- [6] J. Sepioł, Y. Stepanenko, A. Vdovin, A. Mordziński, E. Vogel, J. Waluk, “Proton tunnelling in porphycene seeded in a supersonic jet” *Chem. Phys. Lett.* **296** (1998) 549-556.
- [7] A. Vdovin, J. Sepioł, N. Urbańska, M. Pietraszkiewicz, A. Mordziński, J. Waluk, “Evidence for Two Forms, Double Hydrogen Tunneling, and Proximity of Excited States in Bridge-Substituted Porphycenes: Supersonic Jet Studies” *J. Am. Chem. Soc.* **128** (2006) 2577-2586.
- [8] A. Vdovin, J. Waluk, B. Dick, A. Slenczka, “Mode–Selective Promotion and Isotope Effects of Concerted Double-Hydrogen Tunneling in Porphycene Embedded in Superfluid Helium Nanodroplets” *Chem. Phys. Chem.* **10** (2009) 761-765.
- [9] J. Waluk, M. Muller, P. Swiderek, M. Kocher, E. Vogel, G. Hohlneicher, J. Michl, “Electronic states of porphycenes” *J. Am. Chem. Soc.* **113** (1991) 5511-5527.
- [10] J. Waluk, “Ground– and Excited–State Tautomerism in Porphycenes” *Acc. Chem. Res.* **39** (2006) 945-952.

- [11] M. Gil, J. Walük, “Vibrational Gating of Double Hydrogen Tunneling in Porphycene” *J. Am. Chem. Soc.* **129** (2007) 1335-1341.
- [12] Y. D. Wu, K. W. K. Chan, C. P. Yip, E. Vogel, D. A. Plattner, K. N. Houk, “Porphyrin Isomers: Geometry, Tautomerism, Geometrical Isomerism, and Stability” *J. Org. Chem.* **62** (1997) 9240-9250.
- [13] K. Malsch, G. Hohlneicher, “The Force Field of Porphycene: A Theoretical and Experimental Approach” *J. Phys. Chem. A* **102** (1997) 8409.
- [14] M. Boronat, E. Orti, P. M. Viruela, F. Tomas, “Theoretical study of the N–H tautomerism in free base porphyrin” *J. Mol. Struct. (THEOCHEM)* **390** (1997) 149-156
- [15] P. M. Kozłowski, M. Z. Zgierski, J. Baker, “The inner–hydrogen migration and ground–state structure of porphycene” *J. Chem. Phys.* **109** (1998) 5905-5913
- [16] M. F. Shibl, M. Tachikawa, O. Kühn, “The geometric (H/D) isotope effect in porphycene: grid–based Born–Oppenheimer vibrational wavefunctions vs. multi–component molecular orbital theory” *Phys. Chem. Chem. Phys.* **7** (2005) 1368-1373.
- [17] H. Cybulski, M. Pecul, T. Helgaker, M. Jaszuński, “Theoretical Studies of Nuclear Magnetic Resonance Parameters for the Proton–Exchange Pathways in Porphyrin and Porphycene” *J. Phys. Chem. A* **109** (2005) 4162-4171.
- [18] T. Udagawa, M. Tachikawa, “H/D isotope effect on porphine and porphycene molecules with multicomponent hybrid density functional theory” *J. Chem. Phys.* **125** (2006) 244105.
- [19] Ł. Walewski, D. Krachtus, S. Fischer, J. C. Smith, P. Bała, B. Lesyng, “CC–DFTB energy barriers for single and double proton transfer processes in the model molecular systems malonaldehyde and porphycene” *Int. J. Quant. Chem.* **106** (2006) 636-640.
- [20] Z. Smedarchina, M. F. Shibl, O. Kühn, A. Fernandez-Ramos, “The tautomerization dynamics of porphycene and its isotopomers – Concerted versus stepwise mechanisms” *Chem. Phys. Lett.* **436** (2007) 314-321.
- [21] Ł. Walewski, P. Bała, B. Lesyng, “Steered Classical and Quantum Path-Integral Molecular Dynamics Simulations of Strongly Coupled Protons Motions in Porphycene” *NIC Ser.* **36** (2007) 291-298.

- [22] Ł. Walewski, J. Waluk, B. Lesyng, "Car–Parrinello Molecular Dynamics Study of the Intramolecular Vibrational Mode–Sensitive Double Proton–Transfer Mechanisms in Porphycene" *J. Phys. Chem. A* **114** (2010) 2313-2318.
- [23] D. Marx, M. Parrinello, "Ab initio path-integral molecular dynamics" *Z. Phys. B* **95** (1994) 143-144.
- [24] M. Shiga, M. Tachikawa, S. Miura, "Ab initio molecular orbital calculation considering the quantum mechanical effect of nuclei by path integral molecular dynamics" *Chem. Phys. Lett.* **332** (2000) 396-402.
- [25] M. Shiga, M. Tachikawa, S. Miura, "A unified scheme for ab initio molecular orbital theory and path integral molecular dynamics" *J. Chem. Phys.* **115** (2001) 9149-9159.
- [26] M. Shiga, M. Tachikawa, "Ab initio path integral study of isotope effect of hydronium ion" *Chem. Phys. Lett.* **374** (2003) 229-234.
- [27] J. J. P. Stewart, "Optimization of parameters for semiempirical methods V: Modification of NDDO approximations and application to 70 elements" *J. Mol. Model.* **13** (2007) 1173-1213.
- [28] J. J. P. Stewart, MOPAC2007, Stewart Computational Chemistry, Colorado Springs, CO, USA, <http://www.OpenMOPAC.net> (2007).
- [29] M.J. Frisch *et al.*, GAUSSIAN-03, Revision D.02, Gaussian Inc., Wallingford, CT, 2004.
- [30] A. Gonzalez-Lafont, T. N. Truong, D. G. Truhlar, "Direct dynamics calculations with NDDO (neglect of diatomic differential overlap) molecular orbital theory with specific reaction parameters" *J. Phys. Chem.* **95** (1991) 4618-4627.
- [31] Y. P. Liu, D. H. Lu, A. Gonzalez-Lafont, D. G. Truhlar, B. C. Garrett, "Direct dynamics calculation of the kinetic isotope effect for an organic hydrogen–transfer reaction, including corner–cutting tunneling in 21 dimensions" *J. Am. Chem. Soc.* **115** (1993) 7806-7817.

- [32] I. Rossi, D. G. Truhlar, "Parameterization of NDDO wavefunctions using genetic algorithms. An evolutionary approach to parameterizing potential energy surfaces and direct dynamics calculations for organic reactions" *Chem. Phys. Lett.* **233** (1995) 231-236.
- [33] U. W. Schmitt, G. A. Voth, "The computer simulation of proton transport in water" *J. Chem. Phys.* **111** (1999) 9361-9381.
- [34] T. Yoshikawa, S. Sugawara, T. Takayanagi, M. Shiga, M. Tachikawa, "Theoretical study on the mechanism of double proton transfer in porphycene by path-integral molecular dynamics simulations" *Chem. Phys. Lett.* **496** (2010) 14-19.
- [35] M. J. Gillan, "Quantum simulation of hydrogen in metals" *Phys. Rev. Lett.* **58** (1987) 563-566.

## Chapter 4

### Diffusion of Hydrogen/Tritium in Fe (bcc) lattice

The diffusion coefficients of hydrogen (H) and tritium (T) in  $\alpha$ -Fe have been computed using two approximate quantum dynamical techniques, *i.e.* centroid molecular dynamics (CMD) and ring polymer molecular dynamics (RPMD), in the temperature range of  $T = 100$ – $1000$  K using the embedded-atom-method (EAM) potential. It has been found that the RPMD and CMD methods give very similar results. From a further analysis based on quantum transition state theory (centroid density QTST) combined with path integral molecular dynamics (PIMD), it has been clear that there is a crossover between thermal and quantum mechanisms at about  $T = 500$  K and  $300$  K for H and T diffusions, respectively. The importance of nuclear quantum effects at low temperatures has been illustrated in terms of the effective free energy surface map.

#### 4.1 Hydrogen/Tritium in Metal

Safe control of tritium is one of the technological challenges in the development of next-generation deuterium-tritium fusion reactors where tritium is used as nuclear fuel [1,2]. Tritium should be strictly confined to prevent from contamination by contacts to external environment *via* isotopic exchange with hydrogen in water or hydrocarbons. However, the fundamental database for the properties of tritium that supports such investigations is far from being complete. For instance, the migration rates of tritium in metallic materials which constitute the reactor, as well as the underlying physics of migration, have not been discussed thoroughly from a scientific viewpoint. This status is highly in contrast to the case of hydrogen/deuterium migration, which has been a long-standing research field associated to scientific interest and technological problems

such as hydrogen storage and hydrogen embrittlement [3-6]. The difference is presumably due to the experimental difficulty in dealing with strongly radioactive tritium. Thus, the computational approach would be an alternative that is free of such an experimental limitation. In particular, it is expected that molecular simulation is a useful way that has access to microscopic mechanisms on the atomistic level for a given form of inter-atomic forces, in principle.

## 4.2 Diffusion of hydrogen and tritium atom in pure Fe metal

In this chapter, we investigate the rate and the mechanism of hydrogen (H) and tritium (T) diffusion in the  $\alpha$  phase of iron ( $\alpha$ -Fe). In addition to the technological importance of Fe and Fe alloys as major structural materials for nuclear reactor plants, it is pointed out that the diffusion coefficients of H in  $\alpha$ -Fe are the highest among the values reported thus far for any metal [7], and thus H interstitials in Fe are extremely mobile even at low temperatures. Detailed information on the behavior of H isotopes in Fe is important for understanding the fundamental processes of fast solid-state diffusion and transport in metal-H isotope systems. Previous studies for H (and deuterium) in Fe and other body-centered cubic (bcc) metals suggest that the diffusion mechanisms depend on the quantum and temperature effects [8-20]. In particular, very recently, Kimizuka *et al.* have applied centroid molecular dynamics simulations including quantum mechanical nature of nuclei for the H-atom diffusion processes in Fe [18-20]. They found a curved non-Arrhenius behavior for the temperature dependence of the calculated diffusion coefficients below  $T \sim 500$  K and concluded that quantum nature of H atoms is playing an essential role in diffusion mechanisms. Therefore, it is necessary to use a simulation method where both thermal and quantum diffusion processes are taken into account.

For this purpose, we use two distinct methods based on the approximate quantum dynamics theories relevant to the imaginary-time path integral formulation [21-23], *i.e.* centroid molecular dynamics (CMD) [24-30], and ring polymer molecular dynamics (RPMD) [31-34]. It should be mentioned that the RPMD method has been recently applied to hydrogen atom diffusion on the Ni(100) surface [35]. We here compare the

CMD and RPMD results with those from quantum transition state theory (centroid-density QTST) where the free energy barrier along the diffusive reaction path is estimated numerically by path integral molecular dynamics (PIMD) [17,36-40]. Moreover, we have also carried out classical molecular dynamics (classical MD) where quantum effect is switched off, *i.e.* only the thermal effect is included. All these simulations have been done systematically within the temperature range of  $T = 100\text{--}1000$  K. We note that this is the first report on the quantum molecular dynamics simulation of T-diffusion in metals, according to the authors' knowledge. It generally requires more computational effort to obtain the trajectory of T-diffusion whose rate is much slower than H- or D-diffusion.

### 4.3 Methods

DFT calculations under periodic boundary conditions can obtain reasonable results with experimental data for solid state molecular systems. However, computational costs of the calculation are very high. In order to reduce the costs, the embedded-atom-method (EAM) developed by Kimizuka *et al.* has been employed [18,19]. The EAM potential function includes many-body effects while it is formed by simple formula. RPMD and CMD (see also chapter 2) with the EAM potential function have been applied to Fe<sub>128</sub>H supercell under periodic boundary conditions (lattice constant  $l_c = 2.8553 \text{ \AA}$  and  $4 \times 4 \times 4$  unit cells) in the temperature range of 100–1000 K. We have performed PIMD simulations in order to understand the diffusion mechanism.

#### 4.3.1 Embedded atom model potential function for Fe lattice.

For the Fe–H interaction, we have used the EAM potential to describe the interaction among hydrogen/tritium in the bcc-Fe-lattice [18,19]. The EAM is an empirical implementation of effective-medium theory for the binding energy of a metal [42,43], which includes many-body effects. The energy of a system is given by:

$$V = \frac{1}{2} \sum_{i=1, j \neq i}^N \varphi_{ij}(r_{ij}) + \sum_{i=1}^N F_i(\bar{\rho}_i) \quad (4-1)$$

where the former term corresponds to pair interactions  $\varphi$  as a function of the distance  $r_{ij}$

between the atoms  $i$  and  $j$ , and the latter term is an atomic embedding energy  $F$  as a function of the electron density  $\rho_i$  which is the electron density at atom  $i$  due to the remaining atoms in the system. Thus, the EAM potential for Fe–H is specified by seven functions:  $\varphi_{\text{FeFe}}$ ,  $\varphi_{\text{FeH}}$ ,  $\varphi_{\text{HH}}$ ,  $F_{\text{Fe}}$ ,  $F_{\text{H}}$ ,  $\rho_{\text{Fe}}$  and  $\rho_{\text{H}}$ . According to the EAM model in refs 18 and 19, we used the functions of  $\varphi_{\text{FeFe}}$ ,  $F_{\text{Fe}}$  and  $\rho_{\text{Fe}}$  that were developed by Mendeleev *et al.* [44] and the functions of  $\varphi_{\text{HH}}$ ,  $F_{\text{H}}$  and  $\rho_{\text{H}}$  that were developed by Angelo *et al.* [45]. For the function of  $\varphi_{\text{FeH}}$ , we used the model recently-developed by Kimizuka *et al.* with reference to work of Jiang and Carter [18,19,46]. The pair interactions are defined as

$$\varphi_{\text{FeH}}(r) = \alpha_1 [\exp(-2\alpha_2(r - \alpha_3)) - 2\exp(-\alpha_2(r - \alpha_3))] \quad (4-2)$$

where,  $\alpha_1$ ,  $\alpha_2$ , and  $\alpha_3$  are fitting parameters for DFT calculation [46]. The pair potential  $\varphi(r)$  is described as potential energy function added cutoff energy to  $\varphi_{\text{FeH}}$  and is given by.

$$\varphi(r) = \varphi_{\text{FeH}}(r) + a(r - r_{\text{cut}}) + b \quad (4-3)$$

where  $r_{\text{cut}}$  is the cutoff distance and  $a = -\frac{d\varphi(r_{\text{cut}})}{dr}$  and  $b = -\varphi_{\text{FeH}}(r_{\text{cut}})$ .

On the other hand, the density  $\bar{\rho}_i(r)$  in Eq. (4-1) are defined as

$$\bar{\rho}_i(r) = \sum_{j \neq i}^N \rho_j \quad (4-4)$$

$$\rho_H = S_H \rho_H \quad (4-5)$$

$$F_H(\bar{\rho}) = F_H(\bar{\rho}/S_H) \quad (4-6)$$

where,  $\rho_i$  is denoted as the local electron density of atom  $i$  and  $S_H$  is the relative scaling factor for  $\rho_H$ . EAM parameters using by our simulation are shown in Tables 4-1.

Parameter	$\varphi_{\text{FeH}}$
$S_H$	32.0
$\alpha_1$ (eV)	0.0968
$\alpha_2$ ( $\text{\AA}^{-1}$ )	4.33
$\alpha_3$ ( $\text{\AA}$ )	1.65
$a$ ( $10^{-5}$ eV/ $\text{\AA}$ )	-1.34315
$b$ ( $10^{-5}$ eV)	3.10198
$r_{\text{cut}}$ ( $\text{\AA}$ )	4.2

TABLE 4-1. Parameters for the mixed two-body potential  $\varphi_{\text{FeH}}$  [18,19].

### 4.3.2 Potential energy surface on Fe (100) plane

The geometry and potential energy profile of the Fe–H system obtained from this potential is presented in Figs. 4-1a and 4-1b. The contour plot of the potential energy in Figure 4-1b is shown as a function of the H position on the (100) plane of the bcc-Fe lattice. Notice that the four corners correspond to the Fe positions in the lattice. The most stable trapping site of H is located at the tetrahedral site (T–site, closed circle) and is at  $(L \pm L/2, L)$  and  $(L, L \pm L/2)$  of the (100) plane where  $L = l_c/2$ . The H diffusion microscopically consists of the migration of the H atom from one T–site to another neighboring T–site (dotted line). The saddle-point site (S–site, closed triangle) is a transition state for the H migration, which is located around the midpoint between the two neighboring T–sites. The energy of an H atom at the S–site is 0.088 eV higher than that at the T–site. The H atom diffusion may also occur through the octahedral site (O–site, cross), corresponding to the second-order saddle point on the potential energy surface. The O–site is at the center of (100) plane. The energy state of the H atom at the O–site is lying at 0.144 eV above that at the T–site. These values are comparable with potential energy barriers obtained from density function theory [46]. This suggests that the most energetically favorable diffusion pathway should be that from the T–site to the neighboring T–site *via* the S–site. However, notice that this simple idea cannot be applied when quantized zero-point vibrational energy is taken into account. Since the O–site corresponds to the second-order saddle point as mentioned above, it has two

imaginary vibrational frequencies, while the S-site has only one imaginary vibrational frequency. This implies that the energy difference between the S-site and O-site may become significantly smaller when quantized vibrational frequencies are taken into account. Interestingly, Kimizuka *et al.* found that the two diffusion pathways for H through the S-site and O-site have a comparable free-energy barriers at  $T = 100\text{--}200$  K, while the diffusion pathway through the S-site becomes more important as temperature increases [19]. Therefore, one should take into account the nuclear quantum effects in order to discuss the H/T diffusion processes in Fe more quantitatively. The lattice constant  $l_c$  and dissolution energy  $E_s$  at the most stable structure of  $\text{Fe}_{128}\text{H}$  obtained from this potential are  $2.8553 \text{ \AA}$  and  $0.20 \text{ eV}$  (not include zero-point correction), respectively. Table 4-2 shows the comparison of the EAM results with DFT calculations. The dissolution energy including zero-point vibrational energy is  $0.30 \text{ eV}$  [46]. Notice that the corresponding experiment values are  $2.86 \text{ \AA}$  and  $0.30 \text{ eV}$  respectively [47]. Therefore, our EAM potential energy interaction reasonably reproduces experimental physical quantities.

	DFT	EAM
$E_m$ (eV)	0.088	0.088
$\delta_s$ (Å)	0.407	0.407
$E_{\text{T-O}}$ (eV)	0.13	0.144
$E_s$ (eV)	0.2	0.201
$\Delta V$ (%)	0.06	0.108

TABLE 4-2. Calculated values of the migration energy ( $E_m$ ), distance between the O-site and S-site ( $\delta_s$ ), the difference between the energies of the H atom ( $E_{\text{T-O}} = E_{\text{O}} - E_{\text{T}}$ ) at the O-site and T-site, dissolution energy ( $E_s$ ) of H at the T-site, and percentage change in volume ( $\Delta V$ ). The target DFT energies in the literature [46] are not ZPE-corrected values [18,19]

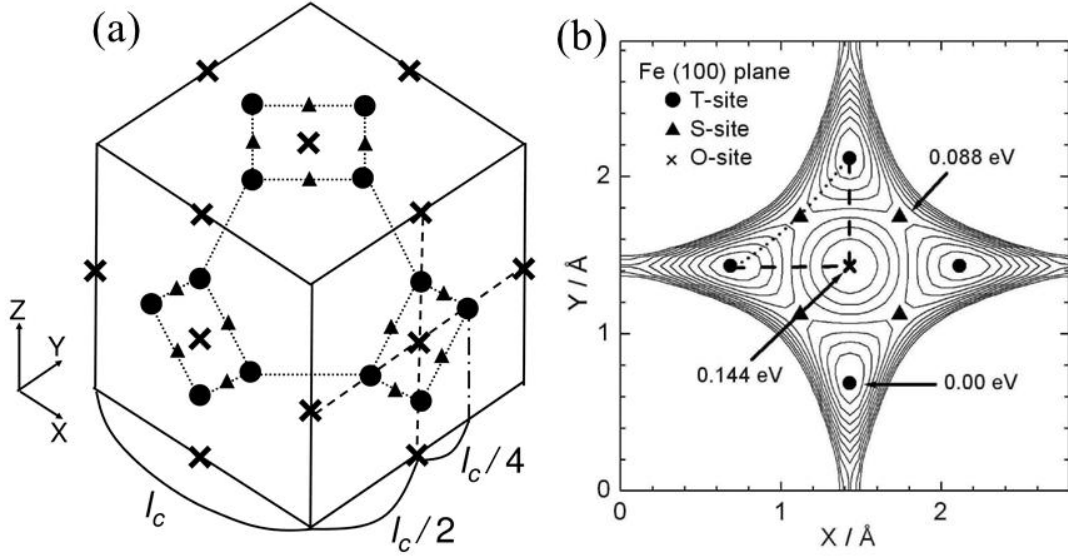


Fig. 4-1. (a) Three-dimensional perspective plots of the stationary points and (b) two-dimensional potential energy surface as a function of Cartesian (X, Y) coordinates (in Å) obtained from the EAM interaction potential on the Fe (100) plane. Contour increments are set to 0.02 eV. Closed circles, closed triangle and cross indicate T-site, S-site and O-site, respectively. Dotted line represents the minimum energy path *via* the S-site and broken line represents the diffusion pathway through the O-site.

### 4.3.3 Estimation of diffusion constant

The diffusion constant of CMD and RPMD is given by the mean square displacement

$$D = \lim_{t \rightarrow \infty} \frac{1}{6t} \langle |\mathbf{q}_x(t) - \mathbf{q}_x(0)|^2 \rangle \quad (4-7)$$

where the angular bracket denotes the statistical average obtained from the CMD and RPMD trajectory, and X is the diffusive atom, H or T. In practice, the time interval  $t$  is chosen to be large such that the mean square displacement increases linearly in time.

### 4.3.4 Simulation conditions

For each temperature condition (100–1000 K), the PIMD simulation were carried out for 2,000,000 steps with a time increment  $\Delta t = 0.1$  fs which was enough to equilibrate the system. For the PIMD (CMD) runs, the massive Nose-Hoover chain thermostats

were attached to all the degrees of freedom (the non-centroid degrees of freedom only) to control the temperature strongly. In all the calculations, we have employed the Fe<sub>128</sub>H supercell under periodic boundary conditions (lattice constant  $l_c = 2.8553 \text{ \AA}$  and  $4 \times 4 \times 4$  unit cells). After some test calculations, we have chosen the number of beads to be  $P = 24$ – $128$  (24 for 1000 K and 128 for 100 K) which give converged results. Then, using those initial positions and velocities, the CMD and RPMD simulations were restarted with a time increment being  $\Delta t = 0.1$  fs. For the CMD runs, the adiabatic parameter  $\gamma$  was set to 0.1. The total step for each CMD or RPMD trajectory was taken to be  $N_s = 4,000,000$  ( $t = 0.4$  ns) at each temperature. The final results were averaged over 15 independent trajectories for both the CMD and RPMD simulations. Since the RPMD dynamics does not use thermostats, one can employ a larger time step for RPMD simulations than that for CMD simulations [52]. In order to confirm this, we have carried out the RPMD calculations with larger time steps of  $\Delta t = 0.5$  and  $1.0$  fs. As a result, we found that the obtained diffusion coefficients were comparable to that obtained with  $\Delta t = 0.1$  fs. This suggests that the RPMD simulations are more efficient for obtaining a large number of trajectories than the CMD simulations. However, we here report computational results with  $\Delta t = 0.1$  fs for both RPMD and CMD simulations since the final results were averaged over the same number of trajectories. The details of our computational code are also described in Refs. 53–55.

#### **4.4 Diffusion constants obtained from RPMD, CMD and classical MD simulations**

First, we present the results of diffusion coefficients obtained from our simulations. Table 4-3 summarized the diffusion coefficients of H and T ( $D_H$  and  $D_T$ ) in Fe calculated with the CMD and RPMD methods at several temperatures in the range of  $T = 100$ – $1000$  K. We have also calculated the diffusion coefficients from classical MD simulations (*i.e.* with  $P=1$ ) and the corresponding results are also included in Table 4-3. The statistical error estimated from the standard deviation of diffusion coefficients obtained from 15 independent trajectories. It can be seen that the both CMD and RPMD results are in very good agreement within statistical uncertainty [8-15]. It is also found

that the classical MD simulations give much smaller diffusion coefficients than the CMD and RPMD results at low temperatures, as expected, due to the lack of quantum mechanical tunneling. On the other hand, the classical MD results are close to the quantum ones of CMD/RPMD at high temperatures. In particular, the diffusion coefficients for T obtained from the classical MD agree well with both the CMD and RPMD values in the temperature range of  $T = 700\text{--}1000$  K.

In the previous CMD work of Kimizuka *et al.* [18,19], the H diffusion coefficients with the same EAM potential were in reasonable agreement with experimental measurements over the temperature range of  $T = 300\text{--}1000$  K [8-15]. This suggests that both the CMD and RPMD simulations using the present EAM potential energy surface can give reliable estimates of diffusion coefficients for hydrogen. Therefore, it is suggested that the present CMD and RPMD simulations give reasonable diffusion coefficients also for tritium. As far as we are aware, there has been only one report on the experimental diffusion coefficients for T; Hagi and Hayashi have estimated the diffusion coefficients for T and H in Fe at  $T = 286$  K to be  $D_T = 0.09 \times 10^{-8} \text{ m}^2 \text{ s}^{-1}$  and  $D_H = 0.4 \times 10^{-8} \text{ m}^2 \text{ s}^{-1}$  using an indirect electrochemical permeation method [56]. It seems that this value of H diffusion coefficient seems to be underestimated since it is almost one half of our CMD and RPMD values ( $0.83\text{--}0.84 \times 10^{-8} \text{ m}^2 \text{ s}^{-1}$  at  $T = 300$  K) as well as other experimental values reported in the literature ( $0.74\text{--}0.89 \times 10^{-8} \text{ m}^2 \text{ s}^{-1}$  at  $T = 300$  K, see Table 4-3) [8-15]. In general, measurements of diffusion coefficients in Fe-H system strongly depend on the purity of the specimen, *i.e.*, concentration of vacancies and impurities, while the specimen of Hagi and Hayashi contains somewhat more impurities ( $> 0.1$  mass %) than in other measurements [8-15,56]. Thus, it might be due to the trapping effects that the estimated tritium diffusion coefficient is underestimated in the study of Hagi and Hayashi [56]. Their experimental  $D_T$  value is also about one half of our CMD and RPMD calculations give  $D_T$  at  $T = 300$  K to be  $0.17 \times 10^{-8} \text{ m}^2 \text{ s}^{-1}$  and  $0.18 \times 10^{-8} \text{ m}^2 \text{ s}^{-1}$ , respectively, although the temperature is slightly different from the experimental temperature. However, the ratio for  $D_T$  and  $D_H$  is in agreement between the computational and experimental results.

<b>Hydrogen</b>					
<i>T</i> / K	CMD	CMD <sup>a</sup>	RPMD	classical MD	exp. ( $D_H/D_T$ )
100	$0.36 \pm 0.22$	0.43	$0.44 \pm 0.10$	NA	-
200	$0.55 \pm 0.01$	-	$0.48 \pm 0.01$	$(2.98 \pm 0.04) \times 10^{-2}$	-
300	$0.83 \pm 0.33$	0.83	$0.84 \pm 0.24$	$0.32 \pm 0.17$	$0.74\text{-}0.87^{\text{b,c}}/0.09^{\text{b,d}}$
500	$1.08 \pm 0.15$	1.15	$1.24 \pm 0.25$	$0.92 \pm 0.13$	$1.5\text{-}1.7^{\text{b}}$
700	$1.75 \pm 0.26$	-	$1.87 \pm 0.05$	$1.92 \pm 0.16$	$1.9\text{-}2.2^{\text{b}}$
800	$1.99 \pm 0.12$	-	$1.95 \pm 0.11$	$2.21 \pm 0.06$	$2.0\text{-}2.4^{\text{b}}$
900	$2.18 \pm 0.08$	-	$2.04 \pm 0.18$	$2.30 \pm 0.02$	-
1000	$2.50 \pm 0.16$	2.37	$2.32 \pm 0.04$	$2.37 \pm 0.11$	$2.45 - 2.63^{\text{b,e}}$

<b>Tritium</b>					
<i>T</i> / K	CMD	CMD <sup>a</sup>	RPMD	classical MD	exp. ( $D_H/D_T$ )
100	$0.03 \pm 0.02$	-	$0.03 \pm 0.01$	NA	-
200	$0.08 \pm 0.02$	-	$0.07 \pm 0.03$	$(1.78 \pm 0.12) \times 10^{-2}$	-
300	$0.17 \pm 0.07$	-	$0.18 \pm 0.06$	$(13.1 \pm 0.09) \times 10^{-2}$	-
500	$0.64 \pm 0.09$	-	$0.72 \pm 0.15$	$0.60 \pm 0.02$	-
700	$1.21 \pm 0.12$	-	$1.19 \pm 0.11$	$1.17 \pm 0.12$	-
800	$1.33 \pm 0.30$	-	$1.28 \pm 0.15$	$1.25 \pm 0.08$	-
900	$1.55 \pm 0.21$	-	$1.52 \pm 0.10$	$1.41 \pm 0.16$	-
1000	$1.56 \pm 0.04$	-	$1.53 \pm 0.15$	$1.58 \pm 0.12$	-

<sup>a</sup>Previous CMD results taken from refs 18 and 19.

<sup>b</sup>Experimental data taken from refs 8–15 and 54.

<sup>c</sup>Measured at 293 K.

<sup>d</sup>Measured for tritium in Fe at 286 K.

<sup>e</sup>Measured at 973 K.

Table 4-3. H/T diffusion coefficients (in  $10^{-8} \text{ m}^2 \text{ s}^{-1}$ ) in the temperature range of 100–1000 K in Fe. The statistical errors have been evaluated from the standard error with respect to 15 independent trajectories in each condition.

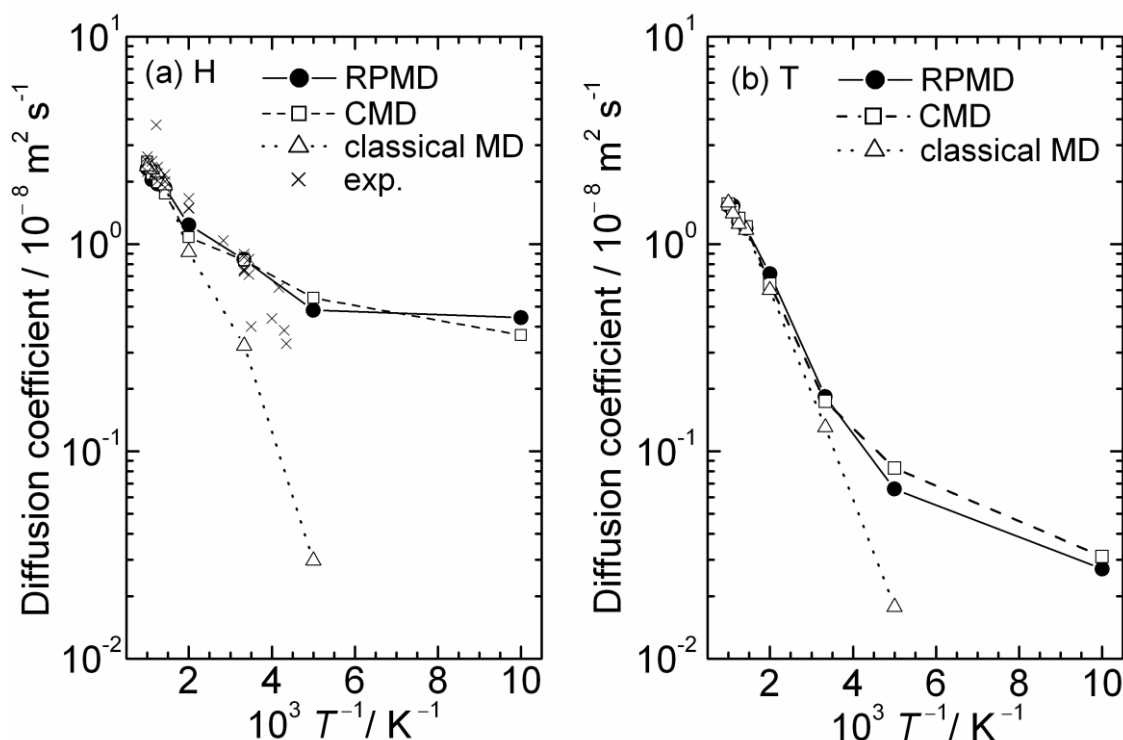


Fig. 4-2. Arrhenius plots of the diffusion coefficients for hydrogen and tritium in Fe. Experimental data are taken from refs 8–15. Solid, broken and dotted line represents results of RPMD, CMD, classical MD simulations, respectively.

#### 4.5 Arrhenius plots of diffusion constants

Figures 4-2a and 4-2b present Arrhenius plots of the diffusion coefficients of H and T in Fe, respectively. The results of the RPMD, CMD and classical MD are shown by closed circles, open squares and open triangles, respectively. The experimental data for H are presented with cross symbols in Figure 4-2a. The Arrhenius plots of the diffusion coefficients of both isotopes calculated with the classical MD method are almost on the straight lines within the temperature range considered here. On the other hand, the diffusion coefficients of both H and T obtained from the present quantum mechanical CMD and RPMD simulations show strong non-linear behaviors at low temperatures. More specifically, a deviation from linearity begins around  $T = 500$  K for H diffusion, while for T diffusion a deviation can be seen below  $T \sim 300$  K (see Table 4-3). The former behavior is in excellent agreement with the previous CMD calculations of

Kimizuka *et al.* Similar results can be also observed in other metals and solids [16-19,57-59]. These results indicate that a nuclear quantum effect, *i.e.* quantum tunneling, is playing an essential role in the diffusion of H and T in Fe at low temperatures.

In order to understand the isotope effect for H and T diffusion in detail, we plot the ratio of the diffusion coefficients  $D_H/D_T$  as a function of  $1000/T$  in Figure 4-3. It can be seen that both the CMD and RPMD methods give very similar curves within statistical uncertainty;  $D_H/D_T$  increases with the temperature decrease. The  $D_H/D_T$  value is seen to be nearly constant around 1.6–1.8 in the higher temperature range ( $> 500$  K). Notice that this value is close to the square root of tritium-hydrogen mass ratio 3.0, in agreement with the classical mechanics. In addition, this result is comparable with experiments in the range of error at room temperature [8-15,56].

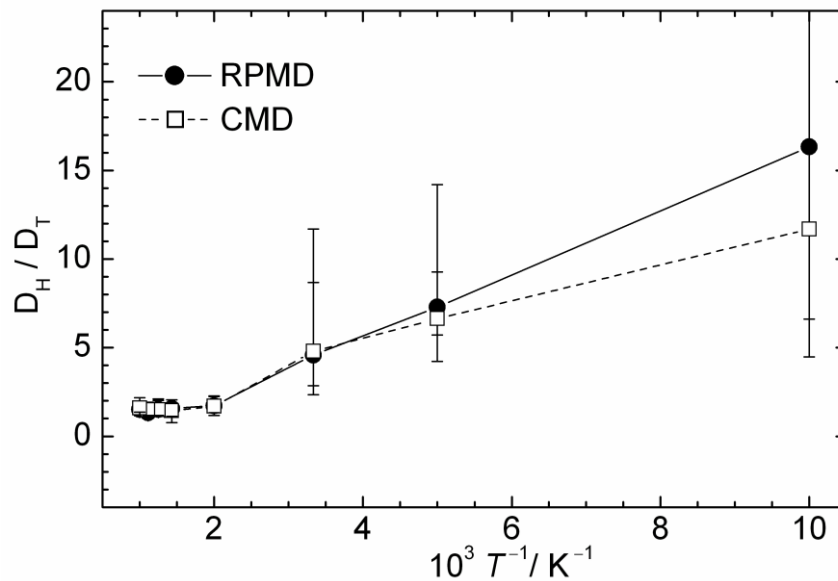


Fig. 4-3. The ratio of the diffusion coefficients for hydrogen and tritium as a

#### 4.6 Three dimensional perspective plots

Figure 4-4 displays representative three-dimensional perspective plots of the nuclear distribution function for the H/T (gray color) in Fe (purple color) obtained from the

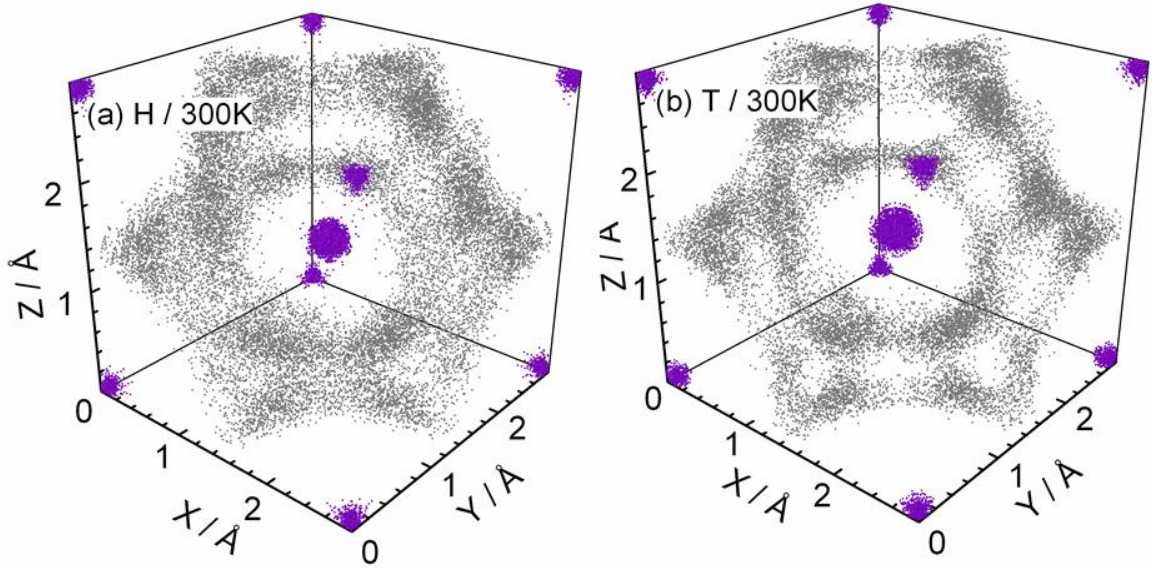


Fig. 4-4. Three-dimensional perspective plots of nuclear distribution of (a) Fe–H and (b) Fe–T obtained from the PIMD simulations at  $T = 300$  K. The purple color is represented the iron atoms and the gray color is represented the hydrogen or tritium. The T–sites are at  $(L \pm L/2, L)$  and  $(L, L \pm L/2)$  of the (100) plane where  $L = l_c/2$  and the O–site is at the center of (100) plane.

PIMD simulation at  $T = 300$  K. In Fig. 4-4a, large fluctuation can be seen for H atom. In particular, we can see that the hydrogen is distributed around not only the paths between T–sites *via* S–sites but also around the O–sites. In Figure 4-4b, however, motion of T is clearly different from H atoms and distributions of T around the O–site are much less than those of H. This clearly shows that there is a significant difference in the mechanisms of H- and T-diffusions on the ability to pass through the O–site. On the other hand, the spread of spatial distribution for the Fe atoms are relatively small compared to those for the H and T. This suggests that the Fe atom behaves as a classical mechanical particle.

#### 4.7 Free energy surfaces on Fe (100) plane

In order to understand the detailed diffusion mechanisms at a microscopic molecular level, it would be useful to present the free-energy surface  $F_T(q)$  along appropriate

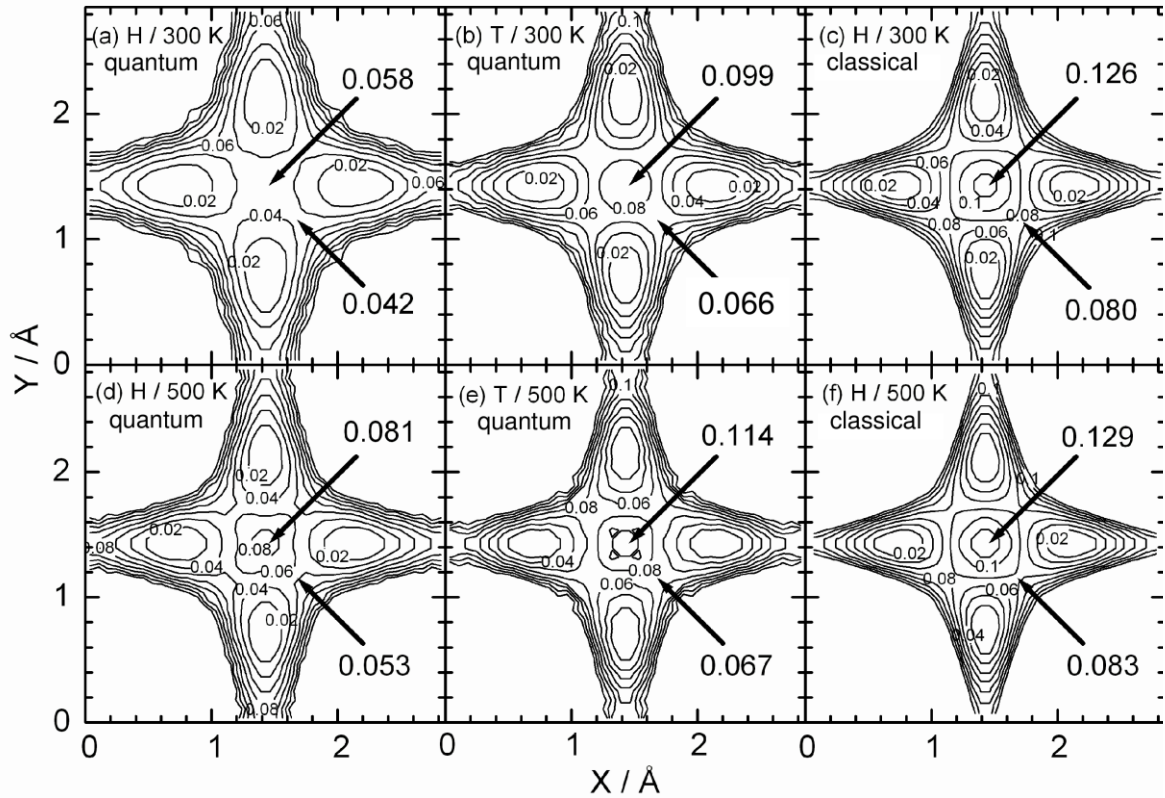


Fig. 4-5. Two-dimensional contour plots of free-energy surfaces (in eV) as a function of the Cartesian ( $X$ ,  $Y$ ) coordinates (in Å) on the Fe(100) plane obtained from the static path-integral molecular dynamics simulations at  $T = 300$  and  $500$  K.

reaction coordinates  $q$  at temperature  $T$  [60]. The free-energy  $F_T(q)$  is defined as  $F_T(q) = -k_B T \ln \rho_T(q)$ , where  $\rho_T(q)$  is the nuclear distribution probability to be observed at a given set of centroid coordinates  $q$  obtained from PIMD at  $T$ . Figure 4-5 displays the two-dimensional free-energy surfaces at  $T = 300$  and  $500$  K on the (100) plane of the bcc-Fe lattice obtained from the PIMD simulations. The values shown in figures are free-energy barriers (in eV) at the S-site and O-site (see also Figure 4-1). These plots are quite useful for understanding the microscopic mechanism of the H/T diffusion processes, because such an energy landscape provides the means to analyze the possible diffusion pathways at the temperature of our interest. For H diffusion at  $T = 300$  K, the quantum free-energy barrier *via* the S-site was estimated to be  $0.042$  eV (measured from the T-site), while the corresponding barrier *via* the O-site was obtained to be

0.058 eV (see Figure 4-5a). This result suggests that the H diffusion process mainly occurs *via* the S-site. However, it should be emphasized that the contribution of the diffusion pathway *via* the O-site at this temperature cannot be ignored since the energy difference between the S-site and O-site barriers is rather small. In the case of T diffusion at  $T = 300$  K (see Figure 4-5b), the quantum free-energy barrier *via* the S-site and O-site were estimated to be 0.066 eV (measured from the T-site) and 0.099 eV (measured from the T-site), respectively. Thus, comparing the height of the barriers, we can confirm that this system clearly shows isotope effects for the H/T migration at 300 K. Besides, the free-energy barriers obtained from the classical MD simulations are much higher than those barriers obtained from the quantum simulations. This also indicates importance of quantum effects even at room temperature. Our results are consistent with the previous CMD results of Kimizuka *et al.* although they have given one-dimensional free-energy profiles [18,19]. As can be expected, the free-energy difference between the S-site and O-site barriers becomes larger as temperature increases (see Figure 4-5d). One of the important origins for this temperature dependence in the barrier height may be large quantum fluctuation at low temperatures, which is characterized by the radius of gyration of the ring polymer at the transition state [17]. In the case of the T diffusion processes, the corresponding energy difference becomes larger than in the case of H-diffusion case. In addition, the free-energy barriers for H and T diffusion obtained from the quantum mechanical simulations are always much smaller than those for H-diffusion obtained from the classical MD simulations. This implies that one should employ appropriate methods that can account for nuclear quantum effects in order to discuss the diffusion dynamics of heavy tritium atoms at a quantitative level.

It may be interesting to compare the free-energy barrier of Figure 4-5 to the activation energy, the slope of Arrhenius plots in Figure 4-2. The activation energies for the H diffusion coefficients obtained from the present RPMD simulations can be roughly estimated to be 0.03 and 0.04 eV at  $T = 300$  and 500 K, respectively. Similarly, the activation energies for the T diffusion coefficients are estimated to be 0.07 and 0.09 eV at  $T = 300$  and 500 K, respectively. Thus, the agreement between the free-energy

barriers at the S-site and the above activation energies is seen to be fairly good although the statistical uncertainty of the RPMD simulations is somewhat large. Again, this rough agreement implies that the dominant bottleneck for the H- and T-diffusion processes in Fe is the S-site at least for  $T \geq 300$  K. We have also estimated imaginary vibrational frequencies along the reaction coordinate using the normal mode analysis on the present EAM potential. The obtained frequencies are  $1460i \text{ cm}^{-1}$  and  $810i \text{ cm}^{-1}$  at the S-site for the Fe-H and Fe-T systems, respectively. Thus, these values can qualitatively explain the difference in the cross-over temperature between H and T diffusion; the cross-over temperature for H diffusion is much lower than that for T due to a larger contribution of quantum tunneling of hydrogen. However, it should be mentioned that this is a very simplified picture because the diffusion pathways at lower temperatures show broader distributions, as Kimizuka *et al.* has already shown in their previous study [18,19].

#### 4.8 Quantum transition state theory

Finally, it will be interesting to compare the results with the centroid density QTST based on the traditional QTST [17,36-41,50,51]. This approach assumes the stochastic process of crossing over the effective free energy barrier in terms of the centroid coordinates

$$D_{\text{QTST}}(T) = \nu(T) \exp(-\Delta F/k_b T) \quad (4-8)$$

where

$$\Delta F = -k_b T \log \frac{Q(\mathbf{q}_{\text{TS}})}{Q(\mathbf{q}_{\text{EQ}})} \quad (4-9)$$

$\Delta F$  is the free energy difference between the transition state either at O- and S-sites ( $\mathbf{q}_{\text{TS}}$ ) and equilibrium at T-site ( $\mathbf{q}_{\text{EQ}}$ ) associated with the quantum partition function for fixed centroid coordinates as

$$Q(\mathbf{q}) = \prod_{i=1}^N \left[ \left( \frac{m_i P}{2\pi\beta\hbar^2} \right)^{\frac{3P}{2}} \int d\mathbf{x}_{i,1} \cdots \int d\mathbf{x}_{i,P} \right] \prod_{i=1}^N \left( \mathbf{q}_i - \frac{1}{P} \sum_{s=1}^P \mathbf{x}_{s,i} \right) \exp(-\beta V_{\text{eff}}). \quad (4-10)$$

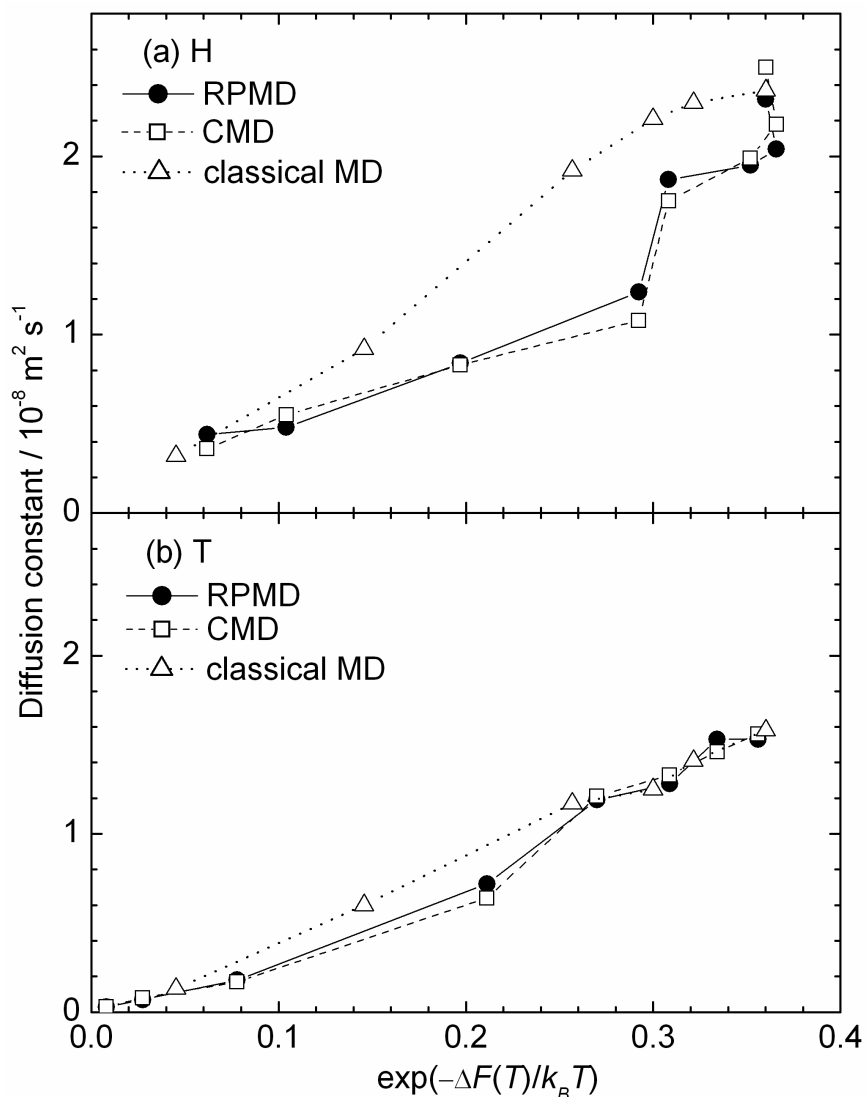


Fig. 4-6. Plots as a function of  $D(T)$  obtained from the quantum simulations and  $\exp(-\Delta F(T)/k_B T)$  obtained from the free-energy. The symbols and lines are the same as Fig. 4-2. Dotted line represents the line connecting classical points.

$\nu(T)$  is the pre-exponential factor which is weakly dependent on temperature in general. The PIMD simulation is able to provide  $\exp(-\Delta F/k_B T)$  since it is equal to the ratio of the centroid probability distributions at the S-site (O-site) and T-site although the direct evaluation of  $D_{\text{QTS}}(T)$  is difficult to obtain  $\nu(T)$  from the PIMD simulation result. In this work,  $\nu(T)$  is roughly estimated from the RPMD and CMD

results and is used to discuss a cross-over temperature below [17].

In Figure 4-6, the diffusion coefficients from CMD/RPMD are plotted as a function of  $\exp(-\Delta F(T)/k_B T)$ , where  $\Delta F$  was estimated with the ratio between the centroid probability densities at the S-site region and the T-site region from the PIMD results. The thermal-quantum crossover temperature can be roughly estimated from these plots [17]. For example, in the case of H diffusion, we can clearly see a significant slope change at  $\exp(-\Delta F(T)/k_B T) \sim 0.3$ , corresponding to  $T \sim 500$  K. This suggests a change in the diffusion mechanism between thermal and quantum processes around this temperature. On the other hand, in the case of T diffusion, the slope change is not so clear compared to the H case; however, we can also see a small slope change around  $\exp(-\Delta F(T)/k_B T) \sim 0.08$  corresponding to  $T \sim 300$  K. However, the slopes of both isotopes calculated with the classical MD method are almost constant. It should be emphasized that these crossover temperature values are consistent with Arrhenius plots of diffusion coefficients presented in Figure 4-2. We hope our computational result will be a stimulus to experiments, although no data has been reported so far for T diffusion.

## 4.9 References

- [1] T. Tanabe, “Tritium handling issues in fusion reactor materials” *J. Nucl. Mater.* **417** (2011) 545-550.
- [2] M. Nishi, T. Yamanishi, T. Hayashi, DEMO Plant Design Team., “Study on tritium accountancy in fusion DEMO plant at JAERI” *Fusion Eng. Des.* **81** (2006) 745-751.
- [3] J. Völkl, G. Alefeld, *Hydrogen in Metals I: Basic Properties*, G. Alefeld, J. Völkl, Eds., Topics in Applied Physics Vol. 28; Springer–Verlag: Berlin, 1978, pp 321-348.
- [4] G. Sandrock, “A panoramic overview of hydrogen storage alloys from a gas reaction point of view” *J. Alloys Comp.* **293–295** (1999) 877-888.
- [5] M. R. Louthan Jr., G. R. Caskey Jr., J. A. Donovan, D. E. Rawl Jr., “Hydrogen embrittlement of metals” *Mater. Sci. Eng.* **10** (1972) 357-368.
- [6] M. Shiga, M. Yamaguchi, H. Kaburaki, “Structure and energetics of clean and hydrogenated Ni surfaces and symmetrical tilt grain boundaries using the embedded–atom method” *Phys. Rev. B* **68** (2003) 245402.
- [7] H. Wipf, H., *Hydrogen in Metals III: Properties and Applications*, H. Wipf, Ed., Topics in Applied Physics Vol. 73, Springer–Verlag: Berlin, 1997, pp 51-91.
- [8] W. L. Bryan, B. F. Dodge, “Diffusivity of hydrogen in pure iron” *AIChE J.* **9** (1963) 223-228.
- [9] J. L. Dillard, “True diffusion coefficient of hydrogen in pure iron” *Seances, C. R. Acad. Sci. Ser. C* , **270** (1970) 669-672.
- [10] Th. Heumann, E. Domke, “Hydrogen diffusion in zone melted  $\alpha$ -iron” *Ber. Bunsen Phys. Chem.* **76** (1972) 825-826.
- [11] K. Kiuchi, R. B. McLellan, “The solubility and diffusivity of hydrogen in well-annealed and deformed iron” *Acta Metall.* **31** (1982) 961-984.
- [12] M. Nagano, Y. Hayashi, N. Ohtani, M. Isshiki, K. Igaki, “Hydrogen diffusivity in high-purity alpha iron” *Scripta Metall.* **16** (1982) 973-976.
- [13] Y. Hayashi, H. Hagi, A. Tahara, “Diffusion Coefficients of Hydrogen and Deuterium in Iron Determined by Permeation with Gas, Ion and Electrical Charging” *Z. Phys. Chem.* **164** (1989) 815-820.
- [14] M. Nagano, Y. Hayashi, N. Ohtani, M. Isshiki, K. Igaki, “Diffusion of Hydrogen

and Deuterium in High Purity Iron between 222 and 322 K” *Trans. JIM* **22** (1981) 423-429.

[15] H. Hagi, “Diffusion coefficient of hydrogen in iron without trapping by dislocations and impurities” *Mater. Trans., JIM* **35** (1994) 112-117.

[16] M. Dyer, C. Zheang, A. Alavi, “Quantum Diffusion of Hydrogen and Isotopes in Metals” *ChemPhysChem* **6** (2005) 1711-1715.

[17] M. J. Gillan, “Quantum simulation of hydrogen in metals” *Phys. Rev. Lett.* **58** (1987) 563-566.

[18] H. Kimizuka, H. Mori, H. Ushida, S. Ogata, “Evaluation of Hydrogen Diffusivity and Its Temperature Dependence in BCC Metals: A Path-Integral Centroid Molecular Dynamics Study” *J. Jpn. Inst. Met.* **73** (2009) 571-576.

[19] H. Kimizuka, H. Mori, S. Ogata, “Effect of temperature on fast hydrogen diffusion in iron: A path-integral quantum dynamics approach” *Phys. Rev. B* **83** (2011) 094110.

[20] H. Kimizuka, S. Ogata, “Slow diffusion of hydrogen at a screw dislocation core in  $\alpha$ -iron” *Phys. Rev. B* **84** (2011) 024116.

[21] R. P. Feynman, A. R. Hibbs, *Quantum Mechanics and Path Integrals*, McGraw-Hill: New York, 1965, Sections 12.8 and 12.9

[22] R. P. Feynman, *Statistical Mechanics*, Benjamin, New York, (1972). Another classic text by Feynman which covers the basic concepts.

[23] D. Chandler, P. G. Wolynes, “Exploiting the isomorphism between quantum theory and classical statistical mechanics of polyatomic fluids” *J. Chem. Phys.* **74** (1981) 4078-4095.

[24] J. Cao, G. A. Voth, “A new perspective on quantum time correlation functions” *J. Chem. Phys.* **99** (1993) 10070-10073.

[25] J. Cao, G. A. Voth, “The formulation of quantum statistical mechanics based on the Feynman path centroid density. II. Dynamical properties” *J. Chem. Phys.* **100** (1994) 5106-5117.

[26] J. Cao, G. A. Voth, “The formulation of quantum statistical mechanics based on the Feynman path centroid density. III. Phase space formalism and analysis of centroid molecular dynamics” *J. Chem. Phys.* **101** (1994) 6157-6167.

- [27] J. Cao, G. A. Voth, “The formulation of quantum statistical mechanics based on the Feynman path centroid density. IV. Algorithms for centroid molecular dynamics” *J. Chem. Phys.* **101** (1994) 6168-6183.
- [28] J. Cao, G. A. Voth, “The formulation of quantum statistical mechanics based on the Feynman path centroid density. V. Quantum instantaneous normal mode theory for liquids” *J. Chem. Phys.* **101** (1994) 6184-6192.
- [29] S. Jang, G. A. Voth, “Path integral centroid variables and the formulation of their exact real time dynamics” *J. Chem. Phys.* **111** (1999) 2357-2370.
- [30] S. Jang, G. A. Voth, “A derivation of centroid molecular dynamics and other approximate time evolution methods for path integral centroid variables” *J. Chem. Phys.* **111** (1999) 2371-2384.
- [31] I. R. Craig, D. E. Manolopoulos, “Quantum statistics and classical mechanics: Real time correlation functions from ring polymer molecular dynamics” *J. Chem. Phys.* **121** (2004) 3368-3373.
- [32] I. R. Craig, D. E. Manolopoulos, “Chemical reaction rates from ring polymer molecular dynamics” *J. Chem. Phys.* **122** (2005) 084106.
- [33] I. R. Craig, D. E. Manolopoulos, “A refined ring polymer molecular dynamics theory of chemical reaction rates” *J. Chem. Phys.* **123** (2005) 034102.
- [34] B. J. Braams, D. E. Manolopoulos, “On the short-time limit of ring polymer molecular dynamics” *J. Chem. Phys.* **125** (2006) 124105.
- [35] Y. V. Suleimanov, “Surface Diffusion of Hydrogen on Ni(100) from Ring Polymer Molecular Dynamics” *J. Phys. Chem. C* **116** (2012) 11141-11153.
- [36] M. J. Gillan, “Quantum-classical crossover of the transition rate in the damped double well” *J. Phys. C* **20** (1987) 3621-3641.
- [37] G. A. Voth, D. Chandler, W. H. Miller, “Rigorous formulation of quantum transition state theory and its dynamical corrections” *J. Chem. Phys.* **91** (1989) 7749-7760.
- [38] G. Mills, H. Jónsson, “Quantum and thermal effects in H<sub>2</sub> dissociative adsorption: Evaluation of free energy barriers in multidimensional quantum systems” *Phys. Rev. Lett.* **72** (1994) 1124-1127.

- [39] G. Mills, H. Jónsson, G. K. Schenter, “Reversible work transition state theory: application to dissociative adsorption of hydrogen” *Surf. Sci.* **324** (1995) 305-337.
- [40] D. G. Truhlar, B. C. Garrett, S. J. Klippenstein, “Current Status of Transition–State Theory” *J. Phys. Chem.* **100** (1996) 12771-12800.
- [41] M. Shiga, H. Fujisaki, “A quantum generalization of intrinsic reaction coordinate using path integral centroid coordinates” *J. Chem. Phys.* **136** (2012) 184103.
- [42] M. S. Daw, M. I. Baskes, “Semiempirical, Quantum Mechanical Calculation of Hydrogen Embrittlement in Metals” *Phys. Rev. Lett.* **50** (1983) 1285-1288.
- [43] M. S. Daw, M. I. Baskes, “Embedded–atom method: Derivation and application to impurities, surfaces, and other defects in metals” *Phys. Rev. B* **29** (1984) 6443-6453.
- [44] M. I. Mendeleev, S. Han, D. J. Srolovitz, G. J. Ackland, D. Y. Sun, M. Asta, “Development of new interatomic potentials appropriate for crystalline and liquid iron” *Philos. Mag.* **83** (2003) 3977-3994.
- [45] J. E. Angelo, N. R. Moody, M. I. Baskes, “Trapping of hydrogen to lattice defects in nickel” *Modell. Simul. Mater. Sci. Eng.* **3** (1995) 289-307.; M. I. Baskes, X. Sha, J. E. Angelo, N. R. Moody, “Trapping of hydrogen to lattice defects in nickel” *Modell. Simul. Mater. Sci. Eng.* **5** (1997) 651-652.
- [46] D. E. Jiang, E. A. Carter, “Diffusion of interstitial hydrogen into and through bcc Fe from first principles” *Phys. Rev. B* **70** (2004) 064102.
- [47] J. P. Hirth, Effects of Hydrogen on the Properties of Iron and Steel; In *Metallurgical Transaction A*, J. P. Hirth, Ed., Springer–Verlag: Berlin, 1980, Vol. 11, pp 861-890.
- [48] A. Pérez, M. E. Tuckerman, M. H. Müser, “A comparative study of the centroid and ring–polymer molecular dynamics methods for approximating quantum time correlation functions from path integrals” *J. Chem. Phys.* **130** (2009) 184105.
- [49] A. Witt, S. D. Ivanov, M. Shiga, H. Forbert, D. Marx, “On the applicability of centroid and ring polymer path integral molecular dynamics for vibrational spectroscopy” *J. Chem. Phys.* **130** (2009) 194510.
- [50] G. A. Voth, “Feynman path integral formulation of quantum mechanical transition–state theory” *J. Phys. Chem.* **97** (1993) 8365-8377.

- [51] G. Mills, G. K. Schenter, D. E. Makarov, H. Jónsson, “Generalized path integral based quantum transition state theory” *Chem. Phys. Lett.* **278** (1997) 91-96.
- [52] M. Ceriotti, M. Perrinello, T. E. Markland, D. E. Manolopoulos, “Efficient stochastic thermostating of path integral molecular dynamics” *J. Chem. Phys.* **133** (2010) 124104.
- [53] M. Shiga, M. Tachikawa, S. Miura, “*Ab initio* molecular orbital calculation considering the quantum mechanical effect of nuclei by path integral molecular dynamics” *Chem. Phys. Lett.* **332** (2000) 396-402.
- [54] M. Shiga, M. Tachikawa, S. Miura, “A unified scheme for *ab initio* molecular orbital theory and path integral molecular dynamics” *J. Chem. Phys.* **115** (2001) 9149-9159.
- [55] M. Shiga, A. Nakayama, “*Ab initio* path integral ring polymer molecular dynamics: Vibrational spectra of molecules” *Chem. Phys. Lett.* **451** (2008) 175-181.
- [56] H. Hagi, Y. Hayasi, “Electrochemical Measurement of Tritium and Hydrogen Permeation through Iron Membranes” *Trans. JIM* **29** (1988) 373-382.
- [57] F. Calvo, D. Costa, “Diffusion of Hydrogen in Palladium Nanoclusters. A Ring-Polymer Molecular Dynamics Study of Quantum Finite Size Effects” *J. Chem. Theory Comput.* **6** (2010) 508-516.
- [58] T. Miyake, T. Ogitsu, S. Tsuneyuki, “Quantum Distributions of Muonium and Hydrogen in Crystalline Silicon” *Phys. Rev. Lett.* **81** (1998) 1873-1876.
- [59] C. P. Herrero, R. Ramírez, “Diffusion of Muonium and Hydrogen in Diamond” *Phys. Rev. Lett.* **99** (2007) 205504.
- [60] U. W. Schmitt, G. A. Voth, “The computer simulation of proton transport in water” *J. Chem. Phys.* **111** (1999) 9361-9380.

## Chapter 5

# Non-Adiabatic Relaxation Dynamics of Hydrated Electron Cluster

In this chapter, the ring-polymer molecular dynamics (RPMD) method was applied to the real-time excess electron dynamics in water clusters within a one-electron pseudo-potential model, where the excess electron motion is described with the grid-based wave function while nuclear motions of water are described with RPMD. We have simulated electronically non-adiabatic relaxation dynamics associated with  $s \rightarrow p$  excitation of an excess electron in the  $(\text{H}_2\text{O})_{50}^-$  and  $(\text{D}_2\text{O})_{50}^-$  water anion cluster. The average relaxation times for  $(\text{H}_2\text{O})_{50}^-$  and  $(\text{D}_2\text{O})_{50}^-$  were calculated to be 120 and 207 fs, respectively, and are comparable to experimental results. Therefore, we conclude that nuclear quantum effects are playing an essential role in the structural rearrangement dynamics of water anion clusters. The detailed nonadiabatic relaxation mechanisms are also discussed.

### 5.1 Hydrated electron

The hydrated electron that excess electron attaches to several water molecules is one of the simplest chemical species, and is very important in various fields including condensed phase chemistry, radiation physics, chemistry and biology [1-4]. Since Hart and Boag detected the hydrated electron experimentally at 1962 [5], extensive studies have been performed from both experimental and theoretical viewpoints. In particular, the relaxation dynamics of the excess electron are well-studied. However, theoretical studies cannot interpret experimental results such as excited-state lifetime and vertical detachment energy (VDE). In addition, the hydrated electron dynamics are still not fully understood.

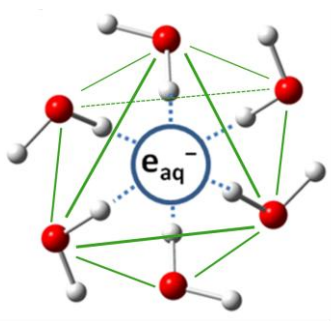


Fig. 5-1. The cavity model of hydrated electron.

## 5.2 Non-adiabatic relaxation dynamics of excited-state hydrated electron and its isotope effects

Early experiments had mainly focused on the microscopic structure of hydrated electron as shown in Fig. 5-1. However, recent experiments have been performed in order to understand the dynamical properties such as the solvation dynamics of an excess electron and the relaxation dynamics of electronically excited state of hydrated electron. For example, Neumark and his co-workers have extensively studied the non-adiabatic relaxation dynamics associated for hydrated electrons in the size-selected water anion clusters  $(\text{H}_2\text{O})_n^-$  using sophisticated ultrafast time-resolved laser techniques [1,6-13]. They have measured  $p \rightarrow s$  non-adiabatic internal conversion time in the  $n = 25\text{--}200$  cluster-size range (as shown in Fig. 5-2). They also estimated internal conversion lifetime to be 60 fs from extrapolation of the measured values to  $n \rightarrow \infty$ . Interestingly, they showed a very strong isotope effects for internal conversion lifetime ( $\tau(\text{D}_2\text{O})/\tau(\text{H}_2\text{O}) \sim 2.8\text{--}3.6$ ).

On the other hand, recent theoretical studies are addressing time-resolved experimental measurements as well as experimental studies [14-20]. Turi and his co-workers have extensively studied the non-adiabatic relaxation dynamics. They have previously found that nuclear quantum effects are very important on the electronically nonadiabatic relaxation within a golden rule approximation. They have obtained lifetimes of bulk to be  $t \sim 100$  fs from the quantum time correlation function and the mixed quantum/classical MD simulation which water nuclei are treated with classical particles. Neria and Nitzan have also carried out the mixed quantum/classical MD

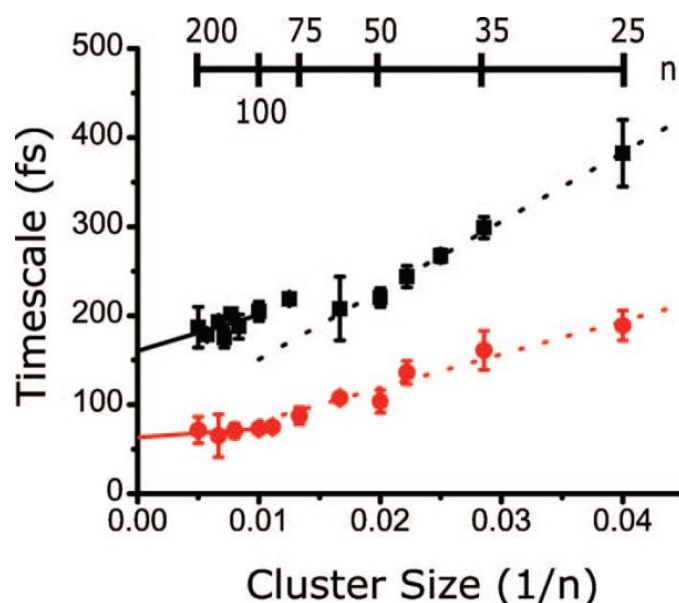


Fig. 5-2. The internal conversion lifetime for size-selected water anion cluster obtained from experiments [1,10]. @ Copyright 2009 American Institute of Physics.

simulation for  $(\text{H}_2\text{O})_{128}^-$  and  $(\text{D}_2\text{O})_{128}^-$  anion cluster [4,19]. Lifetimes obtained from the simulation for these clusters were  $t \sim 220$  fs and  $\sim 800$  fs, respectively; however experiments results are  $\sim 70$  fs and  $\sim 180$  fs, respectively (see also Figure 5-2). This indicates that previous theoretical studies cannot explain the isotope effects of lifetime. In order to understand nuclear quantum effects for the non-adiabatic relaxation dynamics of hydrated electron, we have developed RPMD method and applied to  $(\text{H}_2\text{O})_{50}^-$  and  $(\text{D}_2\text{O})_{50}^-$  water anion cluster.

Fig. 5-3 shows the simplified scheme of the non-adiabatic relaxation dynamics in  $(\text{H}_2\text{O})_{50}^-$  anion cluster. The electronic ground state of the excess electron is approximately *s*-like located outside of the water cluster and there are three *p*-like electronically excited states. When the nearly spherical *s*-like excess electron state is excited into the lowest *p*-like state, the ground state is destabilized as hydrogen atoms of water molecules move into the node of the excited *p*-like wave function. Then, the energy difference between the ground *s*-like and excited *p*-like states becomes close, where an electronically non-adiabatic transition (internal conversion) can eventually occur.

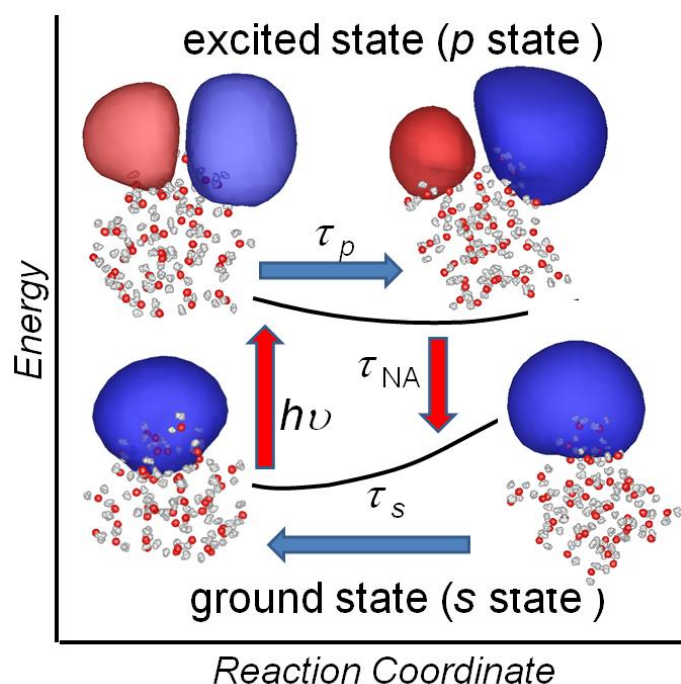


Fig. 5-3. The simplified scheme of the non-adiabatic relaxation dynamics.

### 5.3 Development of RPMD method for describing the non-adiabatic relaxation dynamics

In previous theoretical study, the relaxation dynamics of hydrated electron had been frequently solved using mixed quantum-classical Ehrenfest (mean field) dynamics method [4,21]. However, this method cannot include nuclear quantum effects because motion of nuclear degree of freedom is governed by classical Newton's law. RPMD method can consider nuclear quantum effects for nuclear motion while non-adiabatic effects cannot be described. In order to include both non-adiabatic and nuclear quantum effects in simulation, we have combined RPMD method with the wave packet propagation method within the Ehrenfest mean-field formalism.

#### 5.3.1 One electron wave packet propagation method

In our hybrid simulation method, the motion of an excess electron is described as a one-electron wave function  $\psi$ . The propagation of the wave function is performed with the solution of the time-dependent Schrödinger equation as

$$i\hbar \frac{\partial}{\partial t} |\psi(\mathbf{r}_e)\rangle = \hat{H}(\mathbf{r}_e, \mathbf{x}(t)) |\psi(\mathbf{r}_e)\rangle \quad (5-1)$$

where  $\mathbf{r}_e$  and  $\mathbf{x}$  are denoted as spatial coordinates of an excess electron and nuclear coordinates of in water, respectively. Here, the Hamiltonian in Eq. (5-1) is approximately written as

$$\hat{H}(\mathbf{r}_e, \mathbf{x}(t)) = \hat{H}_{w-w}(\mathbf{x}(t)) + \hat{H}_{e-w}(\mathbf{r}_e; \mathbf{x}(t)) \quad (5-2)$$

where  $\hat{H}_{w-w}$  is the Hamiltonian of water molecules and  $\hat{H}_{e-w}$  is the Hamiltonian of the excess electron-water interaction. All of the Hamiltonians in Eq. (5-2) are described as  $\hat{H} = \hat{T} + \hat{V}$ , where  $T$  and  $V$  are the kinetic energy term and potential energy term, respectively. If the wave function is normalized, atomic forces can be written with Hermann-Feynman force as

$$\begin{aligned} \mathbf{F}(\mathbf{x}(t)) = & -\nabla_{\mathbf{x}} \hat{V}_{w-w}(\mathbf{x}(t)) \\ & - \nabla_{\mathbf{x}} \langle \psi(\mathbf{r}_e) | \hat{V}_{e-w}(\mathbf{r}_e; \mathbf{x}(t)) | \psi(\mathbf{r}_e) \rangle \end{aligned} \quad (5-3)$$

where  $\nabla_{\mathbf{x}}$  is gradient of water nuclear coordinates, and  $\hat{V}_{w-w}$  and  $\hat{V}_{e-w}$  are the interaction potentials for the water-water and the electron-water, respectively. These equations are frequently solved using fewest-switching surface hopping method [21] or mixed quantum-classical Ehrenfest (mean field) dynamics method, where motions of nuclear degrees of freedom are governed by classical Newton's law. Instead of using classical mechanics, we apply the RPMD method for nuclear motions.

### 5.3.2 Hybrid of RPMD with wave packet propagation method

In chapter 2, the quantum canonical partition function  $Z_p$  for  $N$ -particles system in the RPMD method is defined as

$$\begin{aligned} Z_p(\beta) = & \int d\mathbf{p}_{1,1}, \dots, d\mathbf{p}_{N,P} \int d\mathbf{x}_{1,1}, \dots, d\mathbf{x}_{N,P} \\ & \times \exp\left\{-\frac{\beta}{P} H_P(\mathbf{x}_{1,1} \dots \mathbf{x}_{N,P}, \mathbf{p}_{1,1} \dots \mathbf{p}_{N,P})\right\} \end{aligned} \quad (2-13)$$

where  $\mathbf{x}_{i,s}$  and  $\mathbf{p}_{i,s}$  are the Cartesian coordinate and its momentum of the  $i$ -th atom in the  $s$ -th imaginary time slice (*i.e.*, bead). In the RPMD method, the Hamiltonian in  $Z_p$  is defined by

$$H_P(\mathbf{x}_{1,1} \cdots \mathbf{x}_{N,P}, \mathbf{p}_{1,1} \cdots \mathbf{p}_{N,P}) = \sum_{s=1}^P h_s(\mathbf{x}_{1,s} \cdots \mathbf{x}_{N,s}, \mathbf{p}_{1,s} \cdots \mathbf{p}_{N,s}) + \sum_{s=1}^P \sum_{i=1}^N \frac{m_i P^2}{2\beta^2 \hbar^2} (\mathbf{x}_{i,s} - \mathbf{x}_{i,s-1})^2 \quad (5-4)$$

with

$$h_s(\mathbf{x}_{1,s} \cdots \mathbf{x}_{N,s}, \mathbf{p}_{1,s} \cdots \mathbf{p}_{N,s}) = \sum_{i=1}^N \frac{\mathbf{p}_{i,s}^2}{2m_i} + V(\mathbf{x}_{1,s} \cdots \mathbf{x}_{N,s}) \quad (5-5)$$

where  $m_i$  is the  $i$ -th atomic mass and  $P$  is the number of beads. Notice that  $\mathbf{x}_{i,0} = \mathbf{x}_{i,s}$ . From Eqs. (5-2) and (5-5), the Hamiltonian can be expressed as

$$H_P(\mathbf{x}_{1,1} \cdots \mathbf{x}_{N,P}, \mathbf{p}_{1,1} \cdots \mathbf{p}_{N,P}) = \sum_{s=1}^P h_s(\mathbf{x}_{1,s} \cdots \mathbf{x}_{N,s}, \mathbf{p}_{1,s} \cdots \mathbf{p}_{N,s}) + h_{ew}(\mathbf{r}_e; \mathbf{x}_{1,s} \cdots \mathbf{x}_{N,s}) + \sum_{s=1}^P \sum_{i=1}^N \frac{m_i P^2}{2\beta^2 \hbar^2} (\mathbf{x}_{i,s} - \mathbf{x}_{i,s-1})^2 \quad (5-6)$$

with

$$h_s(\mathbf{x}_{1,s} \cdots \mathbf{x}_{N,s}, \mathbf{p}_{1,s} \cdots \mathbf{p}_{N,s}) = \sum_i^N \frac{\mathbf{p}_{i,s}^2}{2m_i} + \hat{V}_{w-w}(\mathbf{x}_{1,s} \cdots \mathbf{x}_{N,s}) \quad (5-7)$$

and

$$h_{ew}(\mathbf{r}_e; \mathbf{x}_{1,s} \cdots \mathbf{x}_{N,s}, \mathbf{p}_e) = \hat{T}_e(\mathbf{p}_e) + \hat{V}_{e-w}(\mathbf{r}_e; \mathbf{x}_{1,s} \cdots \mathbf{x}_{N,s}) \quad (5-8)$$

where  $\hat{T}_e$  and  $\mathbf{p}_e$  are the kinetic energy operator and momentum of an atom, respectively. Since the excess electron motion is affected by all water beads, the potential energy term in Eq. (5-8) is approximated by the mean-field of the excess electron-water interaction.  $\hat{H}_{e-w}$  is thus described as

$$\hat{H}_{e-w} \approx \frac{1}{P} \sum_s h_{ew}(\mathbf{r}_e; \mathbf{x}_{1,s} \cdots \mathbf{x}_{N,s}, \mathbf{p}_{e,s}) = \hat{T}_e(\mathbf{p}_e) + \frac{1}{P} \sum_s \hat{V}_{e-w}(\mathbf{r}_e; \mathbf{x}_{1,s} \cdots \mathbf{x}_{N,s}) \quad (5-9)$$

In this hybrid RPMD, the excess electron motion is described by Eqs. (5-1)-(5-3) and (5-9), and the water nuclear motion is described by Eqs. (5-6), (5-7) and (5-9). Notice that the RPMD method includes both quantum mechanical tunneling and quantized vibrational energy.

## 5.4 Methods

We have employed RWK2-M and Turi-Borgis (TB) one electron pseudo-potential model functions for interaction of water-water and electron-water, respectively [14,22-24]. The *ab initio* molecular orbital method is often utilized and very useful to describe properties of water anion cluster such as structure, hydrogen bonding energy, VDE; however, it is computationally too expensive for large-scale water anion cluster yet. On the other hand, both of RWK2-M and TB model function have been based on very simple formula. All simulation has been performed using these potential energy functions.

### 5.4.1 TB pseudo-potential function for the interaction between an excess electron and water molecules

In previous theoretical studies, TB model function has often been used to understand the non-adiabatic relaxation dynamics of hydrated electron [14]. This is an one-electron pseudo-potential model function and based on simple formula.

$$V_{e-H}(\mathbf{r}_e, \mathbf{x}_H) = -\frac{q_H}{|\mathbf{r}_e - \mathbf{x}_H|} \operatorname{erf}(C_{H,1} |\mathbf{r}_e - \mathbf{x}_H|) + \left[ \frac{C_{H,2}}{|\mathbf{r}_e - \mathbf{x}_H|} \operatorname{erf}(C_{H,3} |\mathbf{r}_e - \mathbf{x}_H|) - \frac{C_{H,4}}{|\mathbf{r}_e - \mathbf{x}_H|} \operatorname{erf}(C_{H,5} |\mathbf{r}_e - \mathbf{x}_H|) \right] \quad (5-10)$$

$$V_{e-O}(\mathbf{r}_e, \mathbf{x}_O) = -\frac{q_O}{|\mathbf{r}_e - \mathbf{x}_O|} \operatorname{erf}(C_{O,1} |\mathbf{r}_e - \mathbf{x}_O|) + \left[ \frac{C_{O,2}}{|\mathbf{r}_e - \mathbf{x}_O|} \operatorname{erf}(C_{O,3} |\mathbf{r}_e - \mathbf{x}_O|) - \frac{C_{O,4}}{|\mathbf{r}_e - \mathbf{x}_O|} \operatorname{erf}(C_{O,5} |\mathbf{r}_e - \mathbf{x}_O|) \right] \quad (5-11)$$

$$V_{pol} = -\frac{\alpha}{2\left(|\mathbf{r}_e - \mathbf{x}_O|^2 + C_{O,4}^2\right)^2} \quad (5-12)$$

where  $V_{e-H}$  and  $V_{e-O}$  are interactions with electron, respectively, and  $V_{pol}$  is polarization potential function. In addition, *erf* is represented as error function. The parameters in Eqs. (5-10)-(5-12) are shown in Table 5-1. This model function gives a roughly spherical cavity hydrated electron structure which is formed by six water OH bonds oriented towards the common center (see Figure 5-1). Accurate VDE values for

small water anion cluster can be also given using this model [25-36]. Most of previously-developed pseudo-potential models yield a cavity structure [14,25-27,32,36]. Jordan and co-workers have recently developed the electron-water interaction potential function [25-27,32]. Results of this potential function can be more comparable with vertical electron binding energies obtained from high level *ab initio* MO calculation in small water anion cluster; however, this calculation spends highly computational cost for RPMD calculation. On the other hand, the recently-developed pseudo-potential predicts a non-cavity structure for the hydrated electron [37,38]. However, the structure obtained from this model is not consistent with the *ab initio* calculation result, and the fitted non-cavity potential cannot show any properties such as exact model's Eigen energy and VDE [25-27,31,32,36]. In addition, the excess electron for this non-cavity model is delocalized over several water molecules in a region where the water density is increased relative to that of neat water. Thus, we have carried out simulation using TB model given cavity hydrated electron model [39].

Parameters	O atom	H atom
$q$	-0.820	0.410
$C_1$	0.575	0.750
$C_2$	0.620	0.150
$C_3$	1.000	0.500
$C_4$	0.400	0.350
$C_5$	4.400	-
$a$	9.7446	-

TABLE 5-1. Parameter set for the electron-water TB pseudo-potential function in Eq. (5-10) [14]. All quantities are in atomic units.

## 5.4.2 RWK2-M model potential for the interaction between water molecules

We have also employed the modified flexible RWK2-M model potential energy functions for water-water interaction [22-24]. RWK potential function described by Watts *et al.* is commonly used for computations of the tunneling splitting pattern before the potentials described above were developed [22]. Recently, Weare and co-workers have developed RWK2-M based on very simple functions as

$$V_{\text{intra}} = \sum_{i=1}^3 D_i \left(1 - e^{-\alpha s_i}\right)^2 + f_{12} s_1 s_2 \quad (5-13)$$

$$s_i = r_{\text{OH}_i} \cos\left(\frac{\theta - \theta_0}{2}\right) - R_0, i = 1, 2 \quad (5-14)$$

$$s_3 = \frac{r_{\text{OH}_1} + r_{\text{OH}_2}}{R_0} \sin\left(\frac{\theta - \theta_0}{2}\right) \quad (5-15)$$

$$V_{\text{inter}} = \sum_{i,j}^3 \frac{q_i q_j}{r_{ij}} + \sum_{\text{O,O}} A_{\text{OO}} e^{-\alpha_{\text{OO}} r_{\text{OO}}} + \sum_{\text{H,H}} A_{\text{HH}} e^{-\alpha_{\text{HH}} r_{\text{HH}}} + \sum_{\text{O,O}} \left\{ -f \left[ C_6 \left(\frac{g_6}{r_{\text{OO}}}\right)^6 + C_8 \left(\frac{g_8}{r_{\text{OO}}}\right)^8 + C_{10} \left(\frac{g_{10}}{r_{\text{OO}}}\right)^{10} \right] \right\} \quad (5-16)$$

$$f = 1 - (c r_{\text{OO}})^\beta e^{-c r_{\text{OO}}} \quad (5-17)$$

$$g_n = 1 - e^{-(a r_{\text{OO}}/n + b r_{\text{OO}}^2)/(n)_2} \quad (5-18)$$

where all parameters are shown in Table 5-2. The radial distribution functions of  $r_{\text{OO}}$ ,  $r_{\text{OH}}$  and  $r_{\text{HH}}$  obtained from the RWK2-M are very comparable with experimental results and *ab initio* MD results [23,24]. In addition, the RWK2-M potential gives a better potential energy curve for the small  $(\text{H}_2\text{O})_n^-$  anion cluster so that explicit vibrational anharmonicity is considered by using Morse functions [23,24]. Thus, we have carried out simulation using RWK2-M model for interaction of water-water.

Parameters	Value (in atomic unit)	Parameters	Value (in atomic unit)
$R_0$	1.8088	$C_6^*$	62.45134
$\theta_0$	104.52	$C_5$	1344.45317
$D_{1,2}$	0.20916	$C_{10}$	50014.91123
$D_3$	0.15660	$A_{00}$	5107.32897
$\alpha_{1,2}$	1.13315	$\alpha_{00}$	2.63108
$\alpha_3$	0.70600	$a$	1.99152
$f_{12}$	-0.00676	$b$	0.098016
$A_{HH}$	1.00703	$\beta$	2.326
$\alpha_{HH}$	1.73603	$c$	0.94834
$q$	0.6000	$\delta$	0.22188758
$A_{OH}$	0.0033045	$c^\beta$	0.88397
$\alpha_{OH}$	3.89559	$R_m$	3.09500

\* $C_n=Cn/0.948347^n$  then converted.

\*\* $fd=2\times R_0\times\cos(\theta_0/2)$

TABLE 5-2. Parameter set for RWK2-M potential function in Eqs. (5-13)-(5-18) [23,24]. All quantities are in atomic units.

### 5.4.3 Simulation conditions

Before the hybrid RPMD simulations were carried out, we firstly performed PIMD simulation (100 ps) with a constant temperature of 200 K to obtain thermally equilibrium  $(H_2O)_{50}^-$  and  $(D_2O)_{50}^-$  anion cluster structures [39]. In PIMD calculations, the massive Nose-Hoover chain technique in velocity Verlet algorithm was used to control the system temperature [40-43]. In the hybrid RPMD simulation, we have randomly sampled 60 initial configurations from 50 ps to 100 ps obtained from PIMD simulations. We have also randomly sampled 120 initial configurations from 100 ps to 150 ps obtained from classical molecular dynamics (classical MD) simulations for comparison with quantum results. In this chapter, classical MD simulation means that nothing of nuclear quantum effects is considered. The time space of nuclear motion in

the hybrid RPMD trajectory is  $\delta t = 0.5$  fs. On the other hand, initial electron wave function is set to the Eigen vector of first excited state in initial structure of the hybrid RPMD simulation and the Eigen vector is obtained by solving Hamiltonian in Eq. (5-9) using discrete variables representation (DVR) method (see Appendix 3) [44]. Here, we have solved the Schrödinger equation expressed with an evenly spaced Cartesian grid in three dimensions.  $32^3$  grid points were employed in the ranges of  $-18.2 \text{ \AA} < X, Y, Z < 18.2 \text{ \AA}$ , where the origin is the center of mass of the water cluster. Because simulation box is adequately larger than water cluster size and electron distribution, we have set cut-off distance  $r_c = 17.3 \text{ \AA}$ . When distance between the mass center of water cluster configuration and the electron position is larger than  $r_c$ , cut-off energy  $V_{cut} = -V_{e-w}(1 - \exp(-|r - r_c|))$  is add to the potential energy function in Eq. (5-9). The Electron wave function is propagated by using split operator method with Fast Fourier Transformation algorism. The time space of wave packet propagation is  $\delta t = 0.05$  fs. All the PIMD and the hybrid RPMD calculations presented in this chapter were carried out with 64 beads, which was determined from convergence tests.

## 5.5 Snapshots of the relaxation dynamics along the representative trajectory

Fig. 5-4 displays snapshots of the  $(\text{H}_2\text{O})_{50}^-$  anion cluster configurations on a representative trajectory obtained from the RPMD simulation. The ground state excess electron gives an *s*-like feature localized on water cluster surface and then the excess electron wave function shows a *p*-like shape when  $s \rightarrow p_1$  excitation occurs ( $t = 0$  fs). Here,  $p_i$  is denoted as the *i*-th electronic excited state. We notice that the initial  $p_1$  wave function is localized near a double-acceptor (AA) hydrogen-bonding water molecule as similar to previous theoretical studies [4,25-36]. As  $t$  increases, the energy gap between the *s* and  $p_1$  states become close up to  $t \sim 50$  fs. When this difference is satisfactorily small, non-adiabatic  $p_1 \rightarrow s$  transition (internal conversion) occurs ( $t = 50$  fs in this trajectory), and then the *s*-like wave function is finally formed. At  $t = 1000$  fs, the wave function becomes more compact since the excess electron is surrounded by several water molecules.

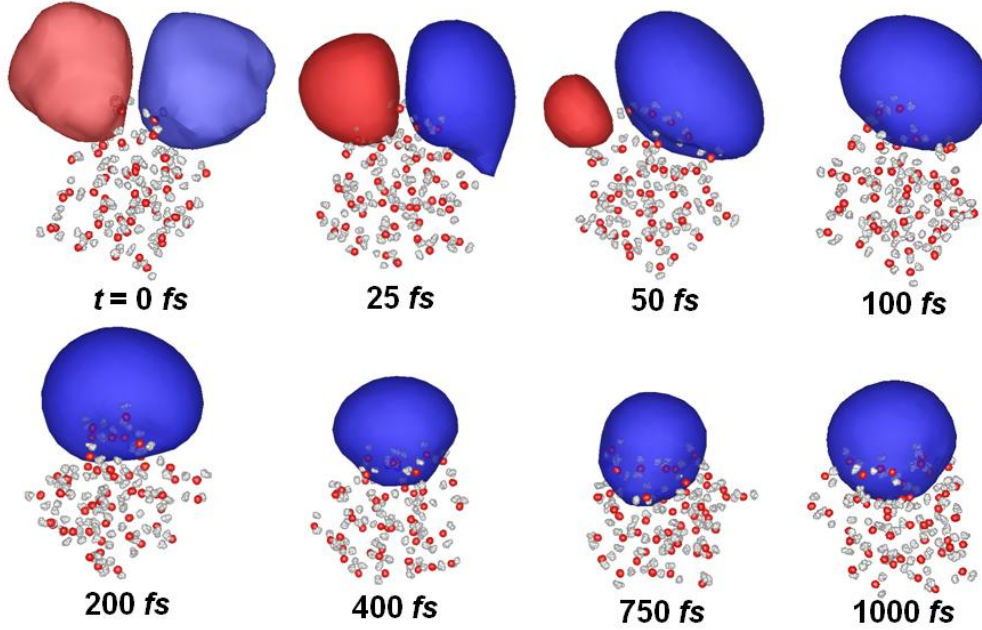


Fig. 5-4. Snapshots of selected cluster configurations along the representative RPMD trajectory. The excess electron wave functions are also shown. Notice that all the bead positions of water nuclei are plotted in this figure for understanding of quantum nature of nuclei.

## 5.6 Temporal changes of physical quantities along the representative RPMD trajectory

Fig. 5-5a shows the adiabatic energies of the lowest four bound states for the excess electron. The electronic-state probabilities (contribution of each electronic state) are plotted as a function of simulation time in Fig. 5-5b. Here, the probability  $P_i$  is defined as follows

$$P_i(t) = \left| \langle \psi(t, \mathbf{r}_e; \mathbf{x}(t)) | \Phi_i(\mathbf{r}_e, \mathbf{x}(t)) \rangle \right|^2 \quad (5-19)$$

where  $\Phi_i(\mathbf{r}_e, \mathbf{x}(t))$  is denoted as the  $i$ -th adiabatic eigenfunction of the excess electron for a given water cluster configuration. We can see the  $s$ -state probability becomes larger than that of the  $p_1$ -state after  $t \sim 50$  fs. We found that the probabilities of the  $p_2$ - and  $p_3$ -states are almost zero on this trajectory. Therefore, the relaxation dynamics may not be significantly affected by these higher electronic states.

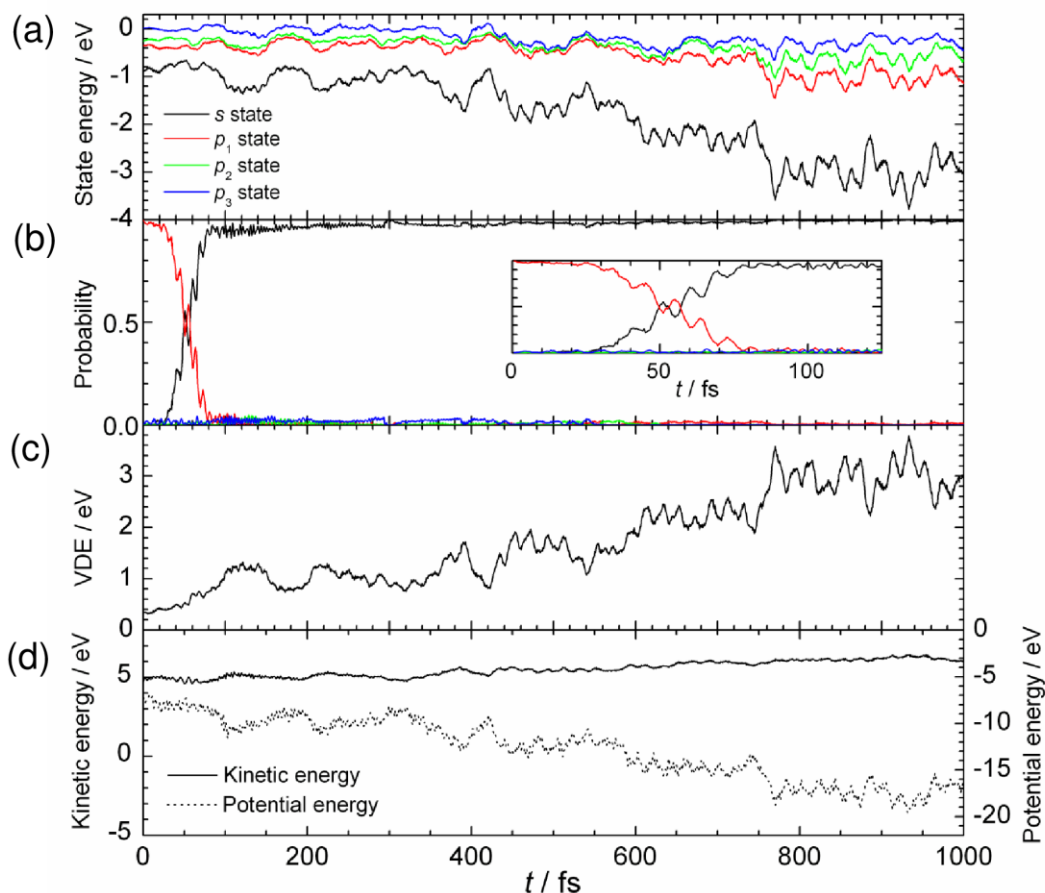


Fig. 5-5. Representative dynamical history of the trajectory presented in Fig. 5-4 as a function of simulation time: (a) the adiabatic energy levels of the lowest four electronic states of the excess electron in eV, (b) probabilities for the lowest two bound states, (c) VDE in eV and (d) the kinetic energy in the water cluster and the water-water potential energy (in eV). For the cluster configurations in figure (a), all the bead positions of water nuclei are plotted.

The plots of the vertical detachment energy (VDE) have been shown in Fig. 5-5c. Previous studies have already shown that the magnitude of the VDE value is largely affected by the number of AA-water molecule directly interacting with the excess electron [4,25-36]. Fig. 5-5d shows the potential and kinetic energies for the water cluster. It is seen that the potential energy gradually decreases while the kinetic energy slightly increases with time.

## 5.7 Statistical aspects of the survival probability and VDE for all trajectories of both $(\text{H}_2\text{O})_{50}^-$ and $(\text{D}_2\text{O})_{50}^-$

In order to understand the statistical aspect of the present RPMD simulations of both  $(\text{H}_2\text{O})_{50}^-$  and  $(\text{D}_2\text{O})_{50}^-$ , we calculate the survival probability of the electronic excited states. The survival probability  $P_s$  can be defined as

$$P_s(t) = 1 - \sum_{i>0, i \neq 1} P_i(t) \quad (5-20)$$

Fig. 5-6a shows the survival probabilities averaged over all 60 RPMD and 120 classical MD trajectories. The survival probability for each RPMD is given in Fig. 5-7. Figs. 5-6b and 5-6c display the VDE change and  $r_{e-w}$ , which is the distance between the center of the excess electron density and center-of-mass of the water cluster, also averaged over all RPMD and classical MD trajectories. The VDE change for each RPMD trajectory is shown in Fig. 5-8. We notice that the magnitude of VDE is well correlated with the value of  $r_{e-w}$ .

The averaged survival probability has been fitted to the following simple exponential function as

$$P_s(t) \sim \exp(-t/\tau) \quad (5-21)$$

It is found that the RPMD survival probability decreases faster than the classical MD one for both the  $(\text{H}_2\text{O})_{50}^-$  and  $(\text{D}_2\text{O})_{50}^-$  clusters. The lifetime values of  $\tau$  for the RPMD results are estimated to be 120 and 207 fs for  $(\text{H}_2\text{O})_{50}^-$  and  $(\text{D}_2\text{O})_{50}^-$ , respectively. These values are comparable to experimental results, which are  $\tau(\text{H}_2\text{O}) \sim 100$  fs and  $\tau(\text{D}_2\text{O}) \sim 200$  fs, respectively [1,6-13]. On the other hand, the lifetime values for the classical MD results are obtained to be  $\tau(\text{H}_2\text{O}) = 205$  fs and  $\tau(\text{D}_2\text{O}) = 304$  fs, respectively. Thus, it is found that nuclear quantum effects are playing an important role for non-adiabatic relaxation dynamics of the excited state in water anion clusters.

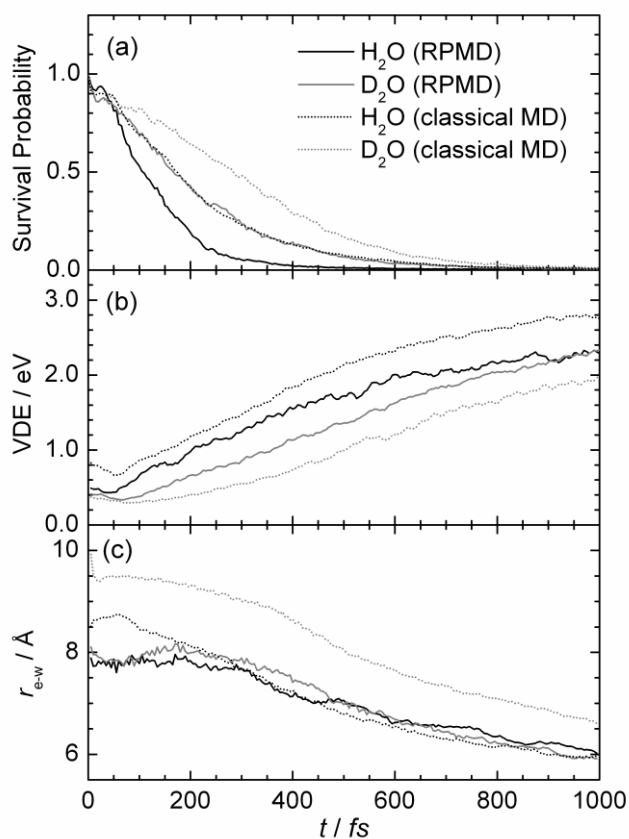


Fig. 5-6. (a) Survival probability (b) VDE and (c) distance  $r_{e-w}$  between electron density center and mass center of water cluster averaged over all 60 RPMD trajectories. Also shown in these figures are the classical MD results averaged over all the 120 trajectories. Solid and dotted lines are denoted as a result of RPMD and classical MD, respectively. In addition, black and gray colors are denoted as a result of  $(\text{H}_2\text{O})_{50}^-$  and  $(\text{D}_2\text{O})_{50}^-$ , respectively.

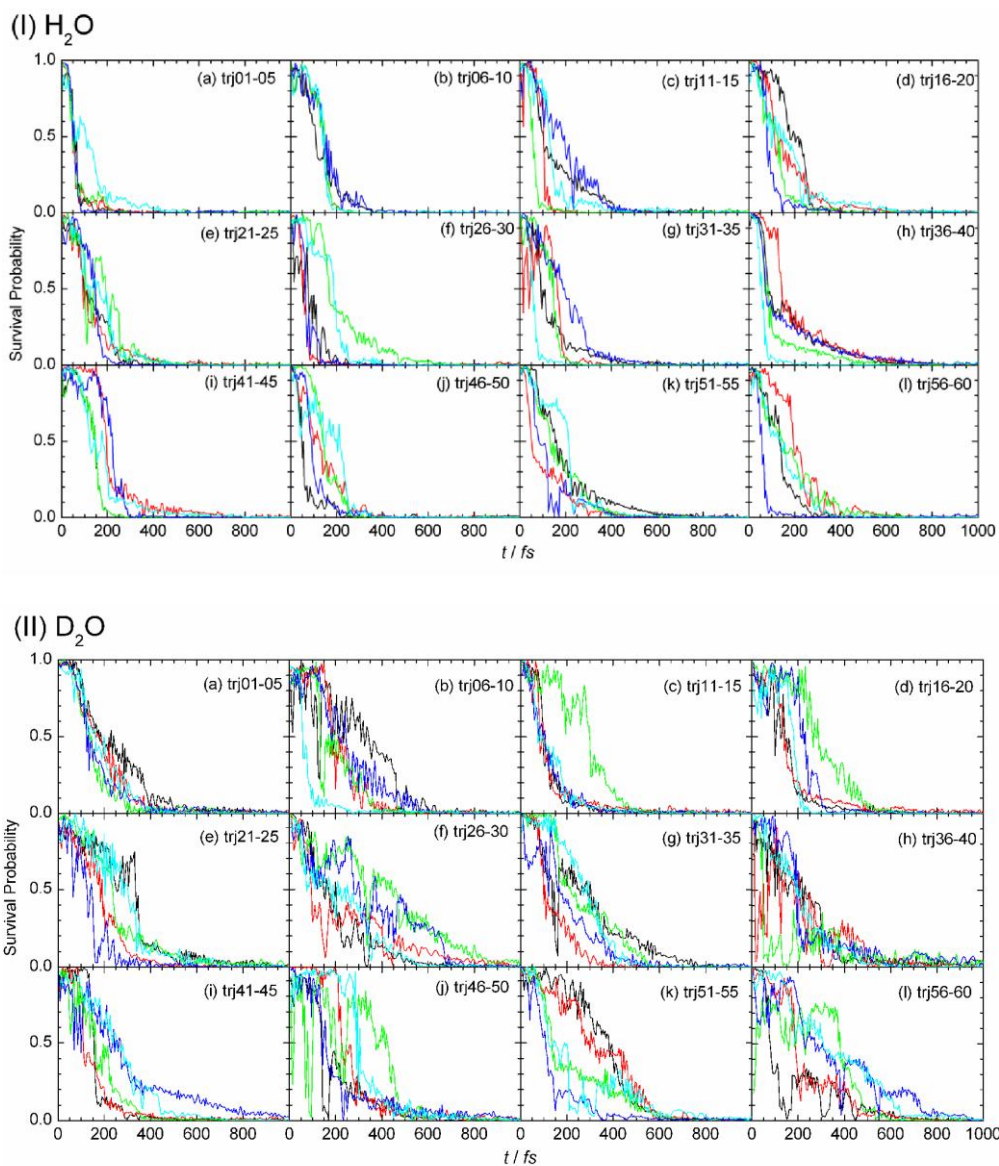


Fig. 5-7. The excited-state survival probabilities of the  $(\text{H}_2\text{O})_{50}^-$  and  $(\text{D}_2\text{O})_{50}^-$  anion clusters as a function of the simulation time for all the 60 RPMD trajectories. 5 RPMD results are shown in the same panel.

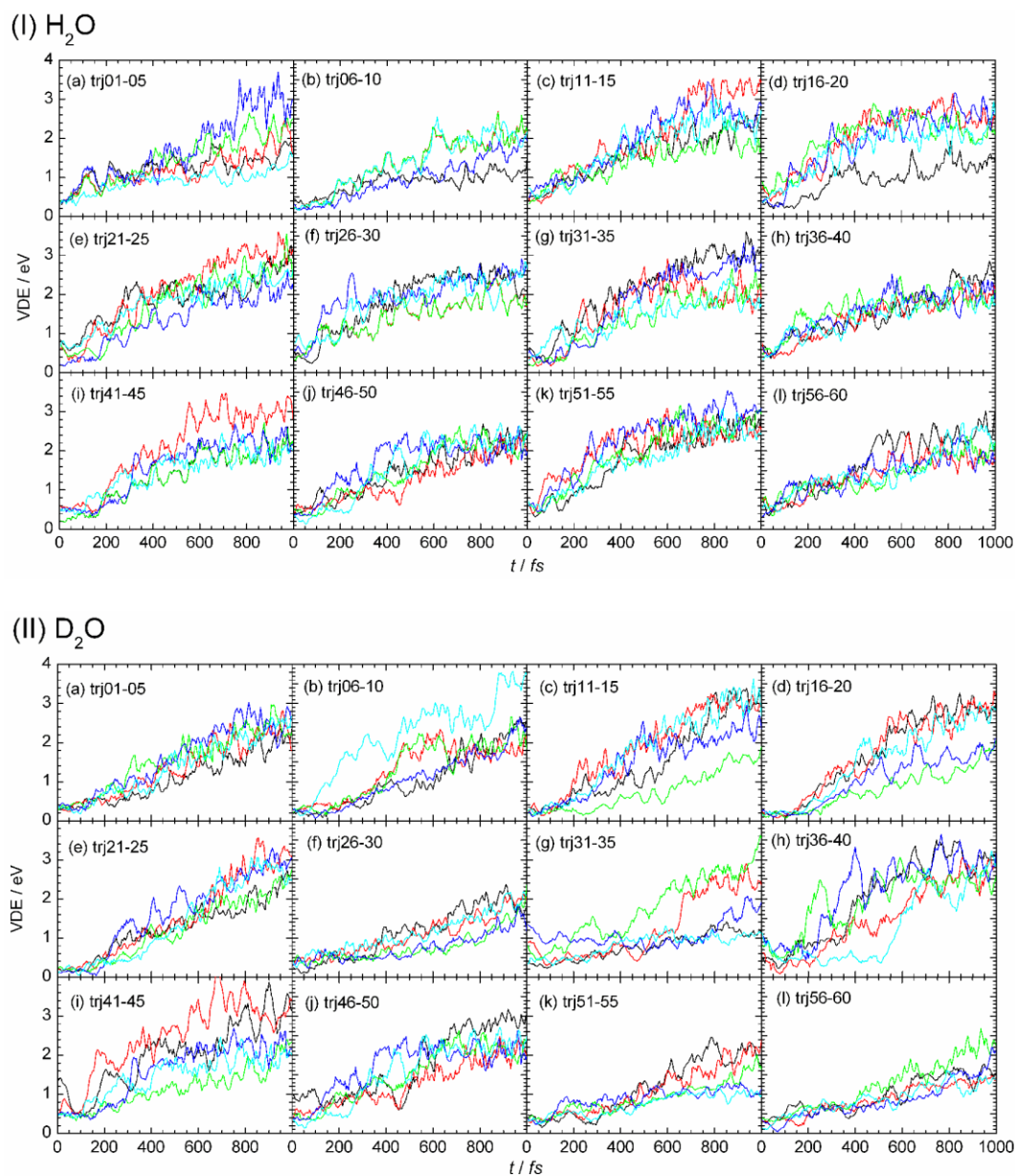


Fig. 5-8. The VDE change of the  $(\text{H}_2\text{O})_{50}^-$  and  $(\text{D}_2\text{O})_{50}^-$  clusters as a function of the simulation time for all the 60 RPMD trajectories. 5 RPMD results are shown in the same panel.

## 5.8 RPMD lifetimes obtained from a different scheme

We have also calculated the averaged relaxation lifetime using a different scheme. Fig. 5-9 shows the lifetime distribution histograms obtained from each RPMD and classical MD trajectories. The mean values from these distributions are  $\tau(\text{H}_2\text{O}) = 114$  fs and  $\tau(\text{D}_2\text{O}) = 206$  fs, respectively, for the RPMD results. These values are quite close to the values obtained from the results in Fig. 5-6.

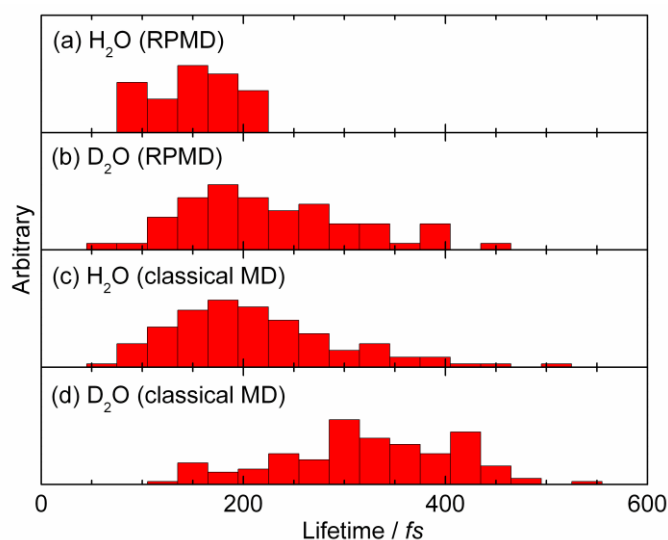


Fig. 5-9. Lifetime distribution functions obtained from each RPMD and classical MD trajectory. The results of  $(\text{H}_2\text{O})_{50}^-$  and  $(\text{D}_2\text{O})_{50}^-$  obtained from 60 RPMD simulations are shown in Figs. 5-9a and 5-9b. The results for 120 classical MD trajectories are shown in Figs. 5-9c and 5-9d. Notice that the box size is 30 fs.

## 5.9 Detailed nonadiabatic relaxation mechanisms

It should be quite important to discuss the detailed mechanism of the electronically nonadiabatic dynamics. Fig. 5-10a shows the schematic nonadiabatic relaxation mechanism. The excess electron wave function is initially localized on the deep potential minimum formed by the excess electron-water dipolar interaction, since the  $s$ -like ground-state wave function is formed on the water cluster. After  $s \rightarrow p_1$  excitation occurs, the water molecules move so as to accommodate the  $p_1$ -like excess electron distribution, forming a temporal multiple well-like potential. Thus, there is a

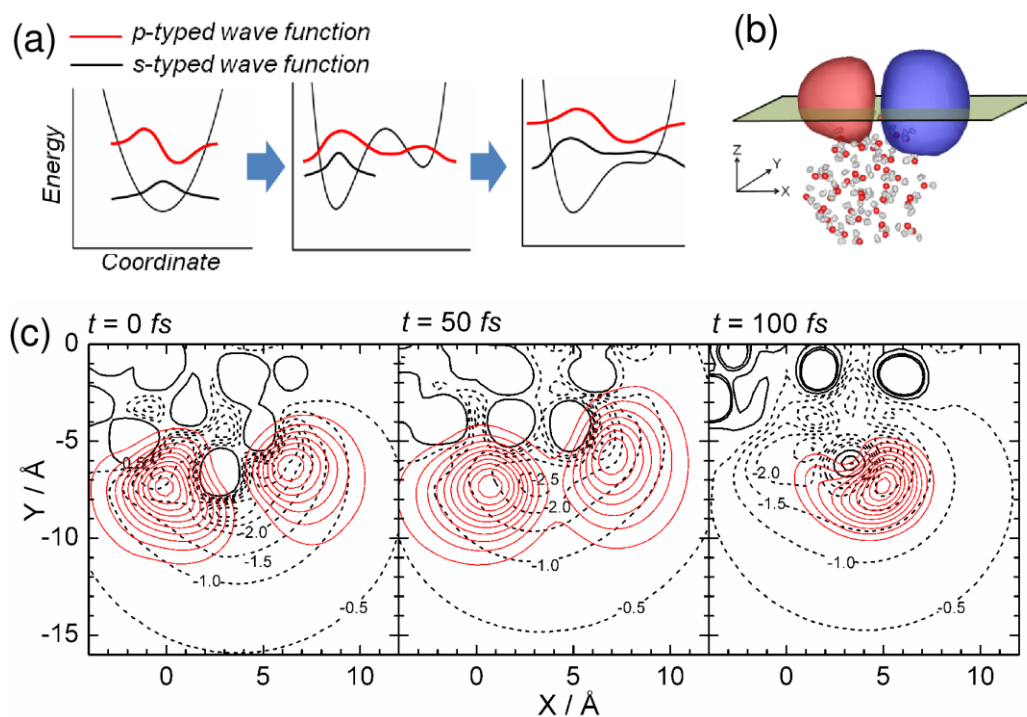


Fig. 5-10. The relaxation mechanism of  $p_1 \rightarrow s$  transition obtained from representative trajectory. (a) Simplified figures of relaxation dynamics, (b) definition of surface plane, (c) potential energy surface of the cut out plane and electron wave function. The potential energy and wave function are described as black and red lines, respectively. Notice that the potential energy surface is denoted as a function of Cartesian coordinates ( $X, Y$ ) in  $\text{\AA}$ . Solid and dotted lines are denoted as positive energy value with contour increments of 0.5 eV and negative with contour increments of 0.2 eV, respectively.

large probability that the energy gap between the lowest and excited states becomes small. In order to understand this scenario at a more quantitative level, the contour plots of the excess electron-water potential energy surfaces at three selected points are presented in Fig. 5-10c. The RPMD trajectory chosen here is the same as that used in Fig. 5-5. The potential energy surfaces cut along with the plane (defined in Fig. 5-10b) are plotted. This plane is intersecting with the nodal plane of the  $p$ -like wave function. In Fig. 5-10c, the wave function densities are also shown with contour plots. The potential energy surface at  $t = 0$  fs shows one deep minimum around the node position,

as expected. At  $t = 50$  fs, a multiple potential well behavior is clearly seen and thus the excess electron density show a somewhat delocalized trend. At  $t = 100$  fs, the  $s$ -like electron density is again formed in a deep potential well after shrinking of the multiple well.

## 5.10 References

- [1] R. M. Young, D. M. Neumark, "Dynamics of Solvated Electrons in Clusters" *Chem. Rev.* **2012**, 112, 5553-5577.
- [2] E. Alizadeh, L. Sanche, "Precursors of Solvated Electrons in Radiobiological Physics and Chemistry" *Chem. Rev.* 112 (**2012**) 5578-5602.
- [3] J. Gu, J. Leszczynski, H.F. Schaefer III, "Interactions of Electrons with Bare and Hydrated Biomolecules: From Nucleic Acid Bases to DNA Segments" *Chem. Rev.* 112 (**2012**) 5603-5640.
- [4] L. Turi, P. J. Rossky, "Theoretical Studies of Spectroscopy and Dynamics of Hydrated Electrons" *Chem. Rev.* 112 (**2012**) 5641-5674.
- [5] E. J. Hart. J. W. Boag, "Absorption Spectrum of the Hydrated Electron in Water and in Aqueous Solutions" *J. Am. Chem. Soc.* **84** (1962) 4090-4095.
- [6] J. R. R. Verlet, A. E. Bragg, A. Kammrath, O. Cheshnovsky, D.M. Neumark, "Observation of Large Water-Cluster Anions with Surface-Bound Excess Electrons" *Science*, 307 (**2005**) 93-96.
- [7] A. E. Bragg, J. R. R. Verlet, A. Kammrath, O. Cheshnovsky, D. M. Neumark, "Electronic Relaxation Dynamics of Water Cluster Anions" *J. Am. Chem. Soc.* 127 (**2005**) 15283 –15295.
- [8] A. Kammrath, J. R. R. Verlet, G. B. Griffin, D. M. Neumark, "Photoelectron spectroscopy of large ( water ) n ( n = 50 – 200 ) clusters at 4.7 eV" *J. Chem. Phys.* 125 (**2006**) 076101.
- [9] D. M. Neumark, Mol. "Spectroscopy and dynamics of excess electrons in clusters" *Phys.* 106 (**2008**) 2183 -2197.
- [10] G. B. Griffin, R. M. Young, O. E. Ehrler, D. M. Neumark, "Electronic relaxation dynamics in large anionic water clusters: (H<sub>2</sub>O)<sub>n</sub> and (D<sub>2</sub>O)<sub>n</sub> (n = 25–200)" *J. Chem. Phys.* 131 (**2009**) 194302.
- [11] R. M. Young, M. A. Yandell, S. B. King, D. M. Neumark, "Thermal effects on energetics and dynamics in water cluster anions (H<sub>2</sub>O) n" *J. Chem. Phys.* 136 (**2012**) 094304.

- [12] J. R. R. Verlet, A. Kammrath, G. B. Griffin, D. M. Neumark, "Electron solvation in water clusters following charge transfer from iodide" *J. Chem. Phys.* **123** (2005) 231102.
- [13] O. T. Ehrler, D. M. Neumark, "Dynamics of Electron Solvation in Molecular Clusters" *Acc. Chem. Res.* **42** (2009) 769-777.
- [14] L. Turi, D. Borgis, "Analytical investigations of an electron–water molecule pseudopotential. II. Development of a new pair potential and molecular dynamics simulations" *J. Chem. Phys.* **117** (2002) 6186-6195.
- [15] D. Borgis, P. J. Rossky, L. Turi, "Quantized time correlation function approach to nonadiabatic decay rates in condensed phase: Application to solvated electrons in water and methanol" *J. Chem. Phys.* **125** (2006) 064501.
- [16] L. Turi, Á. Madarász, P. J. Rossky, "Excess electron localization sites in neutral water clusters" *J. Chem. Phys.* **125** (2006) 014308.
- [17] L. Turi, P. J. Rossky, "Theoretical Studies of Spectroscopy and Dynamics of Hydrated Electrons" *Chem. Rev.* **112** (2012) 5641-5674.
- [18] Á. Madarász, P. J. Rossky, L. Turi, "Response of Observables for Cold Anionic Water Clusters to Cluster Thermal History" *J. Phys. Chem. A* **114** (2010) 2331-2337.
- [19] E. Neria, A. Nitzan, "Semiclassical evaluation of nonadiabatic rates in condensed phases" *J. Chem. Phys.* **99** (1993) 1109-1123.
- [20] A. Staib, D. Borgis, "Molecular dynamics simulation of an excess charge in water using mobile Gaussian orbitals" *J. Chem. Phys.* **103** (1995) 2642-2655.
- [21] R. E. Larsen, M. J. Bedard-Hearn, B. J. Schwartz, "Exploring the Role of Decoherence in Condensed-Phase Nonadiabatic Dynamics: A Comparison of Different Mixed Quantum/Classical Simulation Algorithms for the Excited Hydrated Electron" *J. Phys. Chem. B* **110** (2006) 20055–20066.
- [22] J. R. Reimer, R. O. Watts, M. L. Klein, "Intermolecular potential functions and the properties of water" *Chem. Phys.* **64** (1982) 95-114.
- [23] Z. Duan, N. Moller, J. H. Weare, "Molecular dynamics simulation of water properties using RWK2 potential: From clusters to bulk water" *Geochim. Cosmochim. Acta* **59** (1995) 3273-3283.

- [24] Z. Duan, N. Moller, J. H. Wheare, "Gibbs Ensemble Simulations of Vapor/Liquid Equilibrium Using the Flexible RWK2 Water Potential" *J. Phys. Chem. B* 108 (2004) 20303-20309
- [25] F. Wang, K. D. Jordan, "Application of a Drude model to the binding of excess electrons to water clusters" *J. Chem. Phys.* **116** (2002) 6973-6981.
- [26] K. D. Jordan, "A Fresh Look at Electron Hydration" *Science* 306 (2004) 618-619.
- [27] T. Sommerfeld, K. D. Jordan, "Quantum Drude Oscillator Model for Describing the Interaction of Excess Electrons with Water Clusters: An Application to  $(\text{H}_2\text{O})_{13}^-$ " *J. Phys. Chem. A* **109** (2005) 11531-11538.
- [28] L. Turi, W. -S. Sheu, P. J. Rossky, "Characterization of Excess Electrons in Water-Cluster Anions by Quantum Simulations" *Science* 309 (2005) 914-917.
- [29] L. Turi, Á. Madarász, P. J. Rossky, "Excess electron localization sites in neutral water clusters" *J. Chem. Phys.* 125 (2006) 014308.
- [30] D. Borgis, P. J. Rossky, L. Turi, "Quantized time correlation function approach to nonadiabatic decay rates in condensed phase: Application to solvated electrons in water and methanol" *J. Chem. Phys.* 125 (2006) 064501.
- [31] K. Yagi, Y. Okano, Y. Kawashima, T. Tsuneda, K. Hirao, "Water Cluster Anions Studied by the Long-Range Corrected Density Functional Theory" *J. Phys. Chem. A* 112 (2008) 9845-9853.
- [32] T. Sommerfeld, A. DeFusco, K. D. Jordan, "Model Potential Approaches for Describing the Interaction of Excess Electrons with Water Clusters: Incorporation of Long-Range Correlation Effects" *J. Phys. Chem. A* 112 (2008) 11021-11035.
- [33] Á. Madarász, P. J. Rossky, L. Turi, "Interior-and surface-bound excess electron states in large water cluster anions" *J. Chem. Phys.* 130 (2009) 124319.
- [34] T. Takayanagi, T. Yoshikawa, H. Motegi, M. Shiga, Chem. "Path-integral molecular dynamics simulations for water anion clusters  $(\text{H}_2\text{O})_5^-$  and  $(\text{D}_2\text{O})_5^-$ " *Phys. Lett.* 482 (2009)195.
- [35] Á. Madarász, P. J. Rossky, L. Turi, Response of Observables for Cold Anionic Water Clusters to Cluster Thermal History *J. Phys. Chem. A* 114 (2010) 2331-2337.

- [36] J. M. Herbert, L. D. Jacobson, "Structure of the Aqueous Electron: Assessment of One-Electron Pseudopotential Models in Comparison to Experimental Data and Time-Dependent Density Functional Theory" *J. Phys. Chem. A* **114** (2011) 14470-14483
- [37] R. E. Larsen, W. J. Glover, B. J. Schwartz, "Does the Hydrated Electron Occupy a Cavity?" *Science* **329** (2010) 65-69.
- [38] J. R. Casey, A. Kahros, B. J. Schwartz, "To Be or Not to Be in a Cavity: The Hydrated Electron Dilemma" *J. Phys. Chem. B* **117** (2013) 14173-14182.
- [39] T. Yoshikawa, T. Takayanagi, "Application of ring-polymer molecular dynamics to electronically nonadiabatic excess electron dynamics in water clusters: Importance of nuclear quantum effects" *Chem. Phys. Lett.* **564** (2013) 1-5.
- [40] M. Shiga, M. Tachikawa, S. Miura, "Ab initio molecular orbital calculation considering the quantum mechanical effect of nuclei by path integral molecular dynamics" *Chem. Phys. Lett.* **332** (2000) 396-402.
- [41] M. Shiga, M. Tachikawa, S. Miura, "A unified scheme for ab initio molecular orbital theory and path integral molecular dynamics" *J. Chem. Phys.* **115** (2001) 9149-9159.
- [42] M. Shiga, M. Tachikawa, "Ab initio path integral study of isotope effect of hydronium ion" *Chem. Phys. Lett.* **374** (2003) 229-234.
- [43] U. W. Schmitt, G. A. Voth, "The computer simulation of proton transport in water" *J. Chem. Phys.* **111** (1999) 9361-9381.
- [44] J. C. Light, I. P. Hamilton, J. V. Lill, "Generalized discrete variable approximation in quantum mechanics" *J. Chem. Phys.* **82** (1985) 1400-1409.

# Chapter 6

## General Conclusions

In this work, nuclear quantum effects for dynamical behavior of light particles, such as hydrogen and proton, have been discussed from quantum mechanical viewpoints. In order to understand the quantum behavior, PIMD, RPMD and CMD methods based on the path-integral formalisms have been used. PIMD can obtain the thermal-equilibrium configuration while RPMD and CMD can describe dynamical properties, such as rate and diffusion constants. These methods have been applied to three hydrogen-bonded systems; porphycene (Chapter 3), hydrogen and tritium in Fe (bcc) lattice (Chapter 4) and  $(\text{H}_2\text{O})_{50}^-$  and  $(\text{D}_2\text{O})_{50}^-$  anion clusters (Chapter 5). From these results, we conclude that the quantum behavior of the hydrogen and proton have a significant impact on the reaction mechanism associated with these particles.

### 6.1 Conclusion for chapter 3

We have carried out quantum PIMD simulations in order to theoretically understand the inner double proton/deuteron transfer mechanisms of porphycene and its isotopic variants. We have used the on-the-fly direct dynamics technique at the semiempirical PM6 molecular orbital level but with its semiempirical parameters being adjusted so as that the stationary point energetics reproduces previous *ab initio* and DFT results reasonably. The PIMD simulation for the unsubstituted HH-porphycene at  $T = 300$  K shows that the double proton transfer mechanism dominantly occurs through the concerted pathway *via* configurations around the  $\text{D}_{2\text{h}}$  second-order saddle point. This result is in high contrast with the previous classical simulation results. At  $T = 500$  K, the contribution of the stepwise mechanism significantly increases. It was found that the isotopic substitution of the inner protons into deuterons affects the transfer mechanism. We have also carried out the PIMD simulation for HH-porphycene at  $T = 500$  K with

the porphycene molecular configurations restricting planar structures. Interestingly, this simulation shows that the contribution of the stepwise mechanism decreases compared to the full-dimensional simulation result at the same temperature. From this result, we can qualitatively conclude that out-of-plane vibrational motions suppress the concerted mechanism presumably due to entropic effects.

## 6.2 Conclusion for chapter 4

We have carried out approximate quantum dynamical techniques simulations based on the CMD and RPMD methods using the EAM potential to study the H/T diffusion processes in  $\alpha$ -Fe in the temperature range of  $T = 100$ – $1000$  K. It has been found that the H and T diffusion has the crossover at about  $T = 500$  K and  $300$  K, respectively, which implies that nuclear quantum effects are not negligible at these temperatures or lower. The result is quite similar between the CMD and RPMD methods as well as centroid density QTST based on the PIMD method, which seems to be convincing. The importance of quantum diffusion, even at the room temperature, could be a noticeable outcome that might be of help to tritium confinement problems mentioned in the introduction.

## 6.3 Conclusion for chapter 5

We have combined the RPMD method with the wave packet propagation method within the Ehrenfest mean-field formalism and then applied to the electronically nonadiabatic relaxation dynamics of the excess electron in the  $(\text{H}_2\text{O})_{50}^-$  and  $(\text{D}_2\text{O})_{50}^-$ . The nonadiabatic relaxation lifetimes averaged over all RPMD trajectories were obtained to be  $\tau(\text{H}_2\text{O}) = 120$  fs and  $\tau(\text{D}_2\text{O}) = 207$  fs, respectively. Our simulation results are comparable to the previous experimental results,  $\tau(\text{H}_2\text{O}) \sim 100$  fs and  $\tau(\text{D}_2\text{O}) \sim 200$  fs, respectively. It was found that the classical MD results give longer lifetimes and thus we conclude that nuclear quantum effects are playing an essential role in the present relaxation dynamics. Detailed nonadiabatic relaxation mechanisms are also discussed using the potential energy surfaces formed by the excess electron-water dipolar interaction.



# Appendix A

## Velocity Verlet algorithm

In this work, PIMD, RPMD and CMD simulations. We employed the Velocity-Verlet algorithm, which calculates positions and velocities of particles via Taylor expansion, *i.e.* the Newton's equation-of-motion is second order in relative position ( $\mathbf{x}$ )

$$\mathbf{x}(t + dt) = \mathbf{x}(t) + \mathbf{v}(t)dt + \frac{\mathbf{F}(t)}{m} dt^2 \quad (\text{B-1})$$

$$\mathbf{v}(t + dt) = \mathbf{v}(t) + \frac{\mathbf{F}(t)}{m} dt \quad (\text{B-2})$$

$$\frac{\mathbf{F}(t)}{m} = \mathbf{a}(t) \quad (\text{B-3})$$

where  $\mathbf{v}$  is velocity, and  $m$  and  $F$  are mass and force, respectively. This algorithm also needs the both  $\mathbf{x}(t)$  and  $\mathbf{v}(t)$  at  $t = 0$ . The standard implementation scheme of the Velocity-Verlet algorithm is shown as follows

1.  $\mathbf{v}\left(t + \frac{1}{2} dt\right) = \mathbf{v}(t) + \frac{1}{2} \mathbf{a}(t) dt$  (B-4)

2.  $\mathbf{x}(t + dt) = \mathbf{x}(t) + \mathbf{v}\left(t + \frac{1}{2} dt\right) dt$  (B-5)

$$= \mathbf{x}(t) + \mathbf{v}(t) dt + \frac{1}{2} \mathbf{a}(t) dt^2 \quad (\text{B-6})$$

3. Displace to new positions.

4. Calculate the new forces.

5.  $\mathbf{a}(t + dt) = \frac{\mathbf{F}(t + dt)}{m}$  (B-7)

6.  $\mathbf{v}(t + dt) = \mathbf{v}\left(t + \frac{1}{2} dt\right) + \frac{1}{2} \mathbf{a}(t + dt) dt$  (B-8)

## Appendix B

### Discrete Variable Representation (DVR)

The DVR method can solve accurately the energies and wave functions of bound states for any arbitrary one-dimensional potential function.

First, one-dimensional Hamiltonian is defined as

$$H(x) = T(\hat{p}) + V(\hat{x}) = -\frac{1}{2m} \frac{d^2}{dx^2} + V(\hat{x}) \quad (\text{C-1})$$

Here,  $\Psi_i(x)$  is defined as a wave function obtained by solving this Hamiltonian. Using  $\Psi_i(x)$ , Schrödinger equation is described as

$$\langle \Psi_i | H | \Psi_j \rangle = \delta_{ij} E_j \quad (\text{C-2})$$

The initial and final values of  $x$  are denoted as  $x_0$  and  $x_N$ , respectively. Here, the wave function  $\Psi_i$  can be approximated by an expansion in a set of orthogonally and linearly-independent basis functions  $\phi_i$ ,

$$\Psi_i \approx \sum_{i=1}^N c_{ij} \phi_i \quad (\text{C-3})$$

with  $c_{ij}$  is denoted as an expansion coefficient. From Eqs. (C-2) and (C-3), we can derive Eq. (C-4) as:

$$H_{ij} = \langle \phi_i | H | \phi_j \rangle = \langle \phi_i | T | \phi_j \rangle + \langle \phi_i | V | \phi_j \rangle = T_j \delta_{ij} + \langle \phi_i | V | \phi_j \rangle \quad (\text{C-4})$$

with Kronecker delta function  $\delta_{ij}$ .  $\langle \phi_i | V | \phi_j \rangle$  in Eq. (C-4) can be obtained by using Gaussian quadrature method. This method is one of the numerical integral methods, and evaluates an integral as the sum of a finite number of terms:

$$\int_a^b f(x) dx \approx \sum_{i=1}^n \omega_i f(x_i) \quad (\text{C-5})$$

where  $f(x)$  is an orthogonally and linearly-independent basis function, and  $x_i$  is  $i$ -th node point. In addition,  $\omega$  is represented as weight function. From Eq. (C-5),  $\langle \phi_i | V | \phi_j \rangle$  is described as

$$\langle \phi_i | V | \phi_j \rangle = \sum_{\alpha} \omega_{\alpha} \phi_i(x_{\alpha}) V(x_{\alpha}) \phi_j(x_{\alpha}) = \sum_{\alpha\beta} \sqrt{\omega_{\alpha}} \phi_i(x_{\alpha}) V(x_{\alpha}) \delta_{\alpha\beta} \sqrt{\omega_{\beta}} \phi_j(x_{\beta}) \quad (\text{C-6})$$

$$= \sum_{\alpha\beta} X_{i\alpha} (V(x_{\alpha}) \delta_{\alpha\beta}) X_{\beta j}^{\dagger} \quad (\text{C-7})$$

with  $X_{i\alpha} = \sqrt{\omega_{\alpha}} \phi_i(x_{\alpha})$ .  $x_{\alpha}$  and  $\omega_{\alpha}$  is represented as the  $\alpha$ -th node point and weight, respectively. Thus, Hamiltonian in Eq. (4) is rewritten as

$$(X^{\dagger} H T)(X^{\dagger} c) = \varepsilon (X^{\dagger} c) \quad (\text{C-8})$$

$$\Psi_{ak}^{DVR} = X_{ai}^{\dagger} c_{ik} \quad (\text{C-9})$$

$$H_{\alpha\beta}^{DVR} = X_{\alpha i}^{\dagger} (T_j \delta_{ij}) X_{i\beta} + V(x_{\alpha}) \delta_{\alpha\beta} \quad (\text{C-10})$$

if  $V(x) = 0$  in Eq. (1), Hamiltonian is  $H(x) = -\frac{1}{2m} \frac{d^2}{dx^2}$ . This Eigenfunctions are written

as

$$\phi_n(x) = \sqrt{\frac{2}{b-a}} \sin\left(\frac{n\pi(x-a)}{b-a}\right), \quad n=0,1,\dots,N \quad (\text{C-11})$$

From Eq. (C-11), Kinetic energy matrix in DVR is described as

$$T_{ij} = \langle \phi_n(x_i) | T | \phi_n(x_j) \rangle = -\frac{\hbar^2}{2m} \Delta x \sum_{n=0}^N \phi_n(x_i) \nabla^2 \phi_n(x_j) \quad (\text{C-12})$$

with

$$x_i = a + i\Delta x, \quad n=0,1,\dots,N \quad (\text{C-13})$$

Kinetic energy matrix can be solved analytically, and rewritten as

$$T_{ij} = \begin{cases} \frac{\hbar^2}{2m} \frac{(-1)^{ij}}{(b-a)^2} \frac{\pi^2}{2} \left[ \frac{1}{\sin^2\left(\frac{(i-j)\pi}{2N}\right)} - \frac{1}{\sin^2\left(\frac{(i+j)\pi}{2N}\right)} \right] & (i \neq j) \\ \frac{\hbar^2}{2m} \frac{1}{(b-a)^2} \frac{\pi^2}{2} \left[ \frac{2N^2+1}{3} - \frac{1}{\sin^2\left(\frac{i\pi}{N}\right)} \right] & (i = j) \end{cases} \quad (\text{C-14})$$

In addition, Hamiltonian are represented as

$$H_{ij} = T_{ij} + V(x_i) \delta_{ij} \quad (\text{C-15})$$

Eigenvalues and Eigenvectors can be obtained by solving the DVR Schrödinger equation in Eqs. (C-8) - (C-15).